Appendix A – Referenced Studies and Data on Climate Change Science

Humboldt Bay: Sea Level Rise, Hydrodynamic Modeling, and Inundation Vulnerability Mapping

Prepared for

State Coastal Conservancy, and

Coastal Ecosystems Institute of Northern California

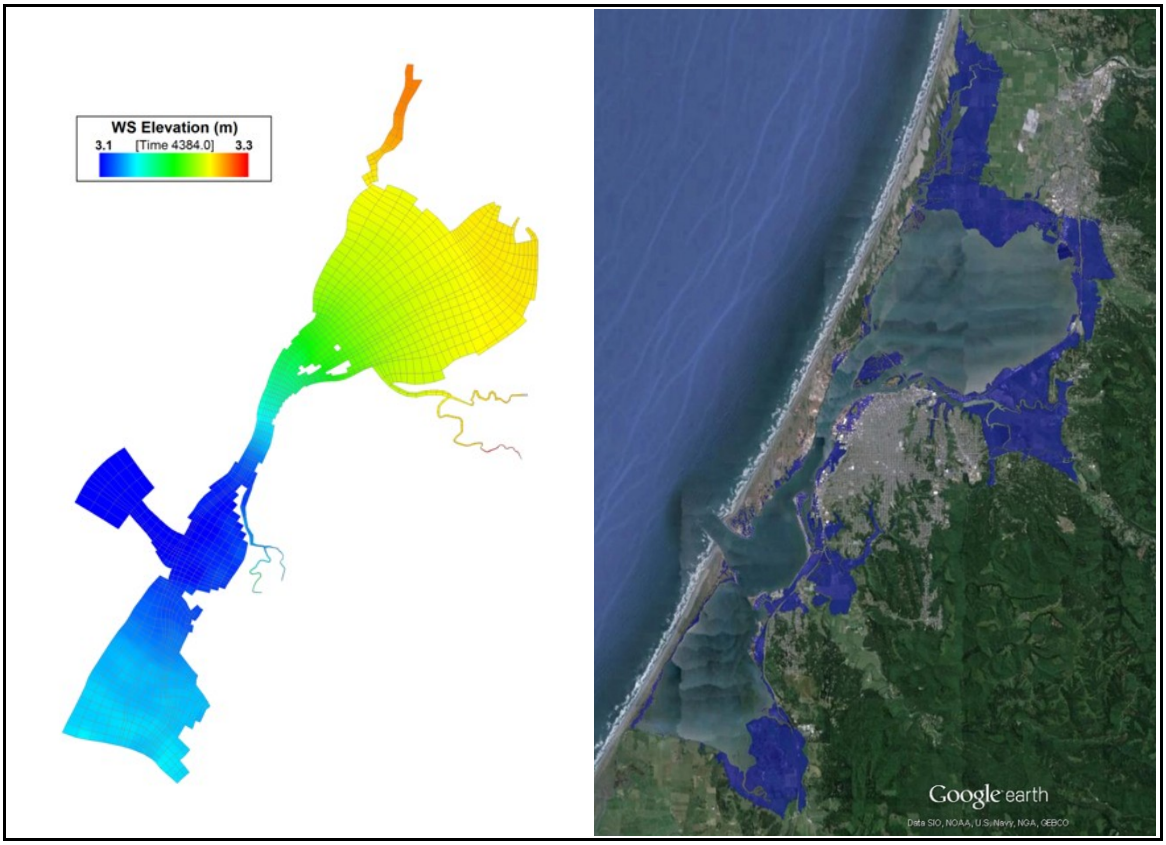

Final Report

April 2015

Prepared by

Northern Hydrology & Engineering

Northern Hydrology & Engineering

Humboldt Bay: Sea Level Rise, Hydrodynamic Modeling, and Inundation Vulnerability Mapping

Final Report

April 2015

Prepared for

State Coastal Conservancy
1330 Broadway, 13th Floor
Oakland, CA 94612-2530

and

Coastal Ecosystems Institute of Northern California
PO Box 806
Bayside, CA 95524

Prepared by and under the supervision of Jeffrey K. Anderson, PE (C50713)

Northern Hydrology & Engineering
P.O. Box 2515
McKinleyville, CA 95519

Northern Hydrology & Engineering

Cover figure: Humboldt Bay predicted water level for year 2012 (left figure), and resulting 100-yr vulnerability inundation map (right figure).

Table of Contents

1 Introduction

Background

Sea level rise is one of the most evident and problematic consequences of global climate change. As the earth's climate warms, sea levels increase primarily from thermal expansion of a warmer ocean and melting land ice (NRC, 2012). In California, sea level rise (SLR) will threaten and directly affect vulnerable coastal ecosystems, bays and estuaries, coastal communities and infrastructure due to increased flooding, gradual inundation, and erosion of the coastal shorelines, cliffs, bluffs and dunes (Russell and Griggs, 2012). If sea level continues to rise at present rates, impacts identified in this report could take decades or longer to occur. However, a troublesome aspect of climate change and the rapid warming of the earth's atmosphere and ocean is the potential for SLR to accelerate to high rates over a short period of time, in which case the identified impacts could happen within a much shorter period (years to decades).

In 2008, California Governor Schwarzenegger issued Executive Order S-13-08 directing state agencies to plan for SLR and corresponding impacts. Following the executive order, planning for the inevitable effects of SLR to California's communities and regions has become a priority for many local coastal governments and state agencies.

Humboldt Bay is located in northernmost California approximately 160 km south of the Oregon border and 420 km north of San Francisco (Figure 1-1). The bay contains numerous aquatic and terrestrial ecosystems that support a diversity of wildlife species, Native American cultures, a number of small towns and communities (e.g. Eureka and Arcata), and an economy dependent on natural resources (Schlosser et al., 2009). Beginning in 2006, with funding from the State Coastal Conservancy (SCC), a group of local scientists, resource managers, and stakeholders established a Science Advisory Team to explore how ecosystem-based management could be applied to Humboldt Bay. In 2008, with funding from the David and Lucile Packard Foundation, the Advisory Team undertook a formal strategic planning effort in Humboldt Bay. A culmination of these efforts was the Humboldt Bay Strategic Plan and the formation of the Humboldt Bay Initiative (Schlosser et al., 2009). The strategic plan identified climate change and associated SLR as a very high threat to Humboldt Bay, and further noted that these threats were not well understood nor had they been assessed.

Recently, the SCC began funding a coordinated planning effort to identify SLR vulnerabilities and develop adaptation strategies for Humboldt Bay, known as the Humboldt Bay Sea Level Rise Adaptation Planning (HBSLRAP) project. The first phase of this work was a Humboldt Bay shoreline inventory, mapping and vulnerability assessment conducted by Trinity Associates (Laird, 2013) that identified portions of the bay's shorelines vulnerable to failure and overtopping from current sea levels. The second phase, which was sponsored by the Coastal Ecosystems Institute of Northern California (CEINC), consisted of two components: identifying additional SLR vulnerabilities in Humboldt Bay through a detailed technical study, and SLR

adaptation planning and risk assessment, co-sponsored by the Humboldt County Public Works (County) and Humboldt Bay Harbor, Recreation and Conservation District (District).

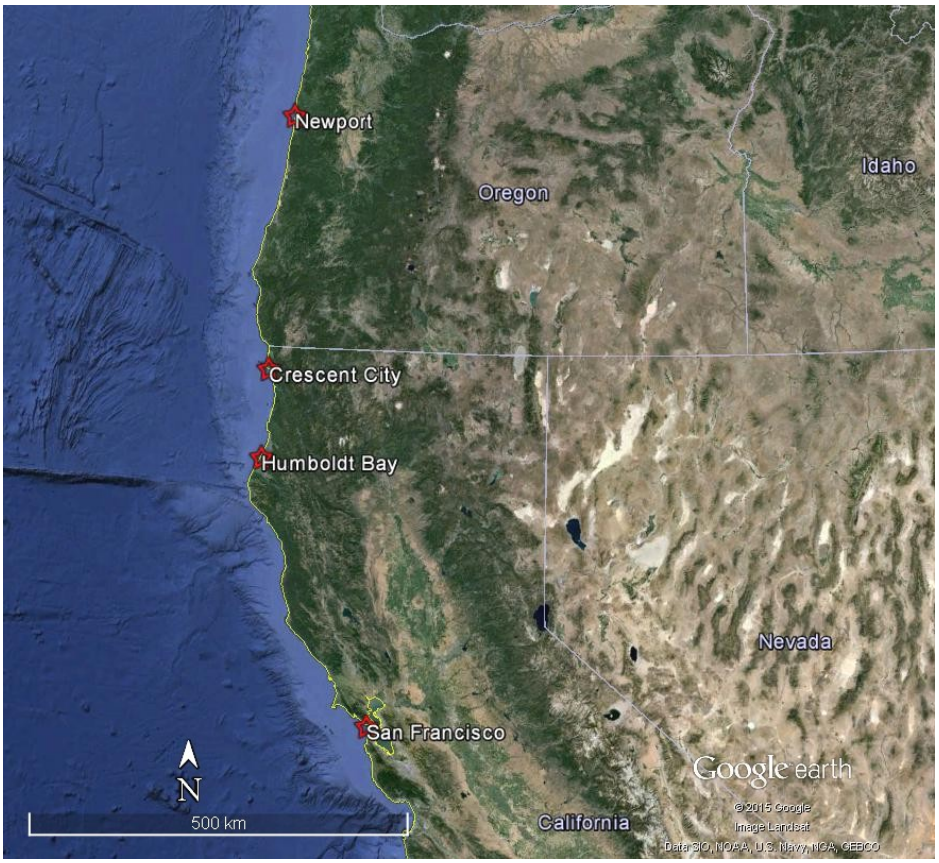

Figure 1-1 Humboldt Bay location map.

The County and District convened an Adaptation Planning Working Group (APWG) for the adaptation planning component of the project, with Trinity Associates serving as the adaptation planning consultant for the working group. The APWG consists of members from the District, County, Cities of Arcata and Eureka, California Coastal Commission, State Coastal Conservancy, Wiyot Tribe, Humboldt Bay National Wildlife Refuge, California Department of Fish and Wildlife, U.S. Fish and Wildlife Service, Bureau of Land Management, California Department of Transportation, California Sea Grant Extension, Humboldt County Farm Bureau, Humboldt County Resources Conservation District, National Resources Conservation Service, North Coast Regional Land Trust, CEINC, Trinity Associates, U.C. Agricultural Extension, and Northern Hydrology & Engineering. The goal of the APWG is to support informed decision-making and encourage a unified, consistent regional adaptation strategy to address impacts to critical assets associated with SLR in the Humboldt Bay region.

The project component to identify additional SLR vulnerabilities in Humboldt Bay was led by Northern Hydrology and Engineering (NHE) and consisted of the following work products:

1. SLR hydrodynamic modeling to develop inundation vulnerability maps of areas surrounding Humboldt Bay vulnerable to inundation from existing and future sea levels (described in this report).
2. A seamless topographic/bathymetric digital elevation model (DEM) of Humboldt Bay using the recent 2009-2011 California Coastal Conservancy LiDAR Project Hydro-flattened Bare Earth DEM (California Coastal DEM) and various subtidal bathymetric data sets to support the modeling efforts. Pacific Watershed Associates (PWA) conducted this work in 2014.
3. A conceptual groundwater model to analyze the effects of SLR on groundwater levels and saltwater intrusion in the Eureka-Arcata coastal plain. Dr. Robert Willis conducted this work in 2014.

Purpose and Scope

Sea level rise already threatens many areas surrounding Humboldt Bay that are currently protected by the natural shoreline, levees, and road or railroad grades from flooding by extreme high tides and storm events, and many more vulnerable areas will be threatened by SLR within the century. If SLR rates accelerate as projected, these vulnerable areas could see routine flooding within the next few decades, particularly if levees or other shoreline barriers fail. The purpose of this project is to (1) conduct detailed hydrodynamic modeling in Humboldt Bay to determine average high water levels and extreme high water level event probabilities for existing sea levels and SLR scenarios, and (2) develop inundation maps of areas surrounding the bay that are vulnerable to inundation from existing and future sea levels. The ultimate goal of this project is to provide the APWG and general public information on how SLR may affect high water levels in Humboldt Bay, including inundation vulnerability maps in a user-friendly format.

For the remainder of this study, the Humboldt Bay shoreline refers to the natural shoreline, and the portions of shoreline consisting of levees, road and railroad grades, and other man-made barriers or structures.

Humboldt Bay Physical Description

Humboldt Bay can best be described as a tidally driven, multi-basin, bar-built, coastal lagoon (Figure 1-2), and is the second largest enclosed bay in California (Costa, 1982; Costa and Glatzel, 2002; Schlosser and Eicher, 2012). The bay is separated from the Pacific Ocean by two long, narrow sand spits (North Spit and South Spit), and is connected to the ocean by the stabilized, twin-jettied Entrance Channel. The first attempts to stabilize the entrance began in 1889, and dredging of interior harbor channels began as early as 1881 (Costa and Glatzel, 2002).

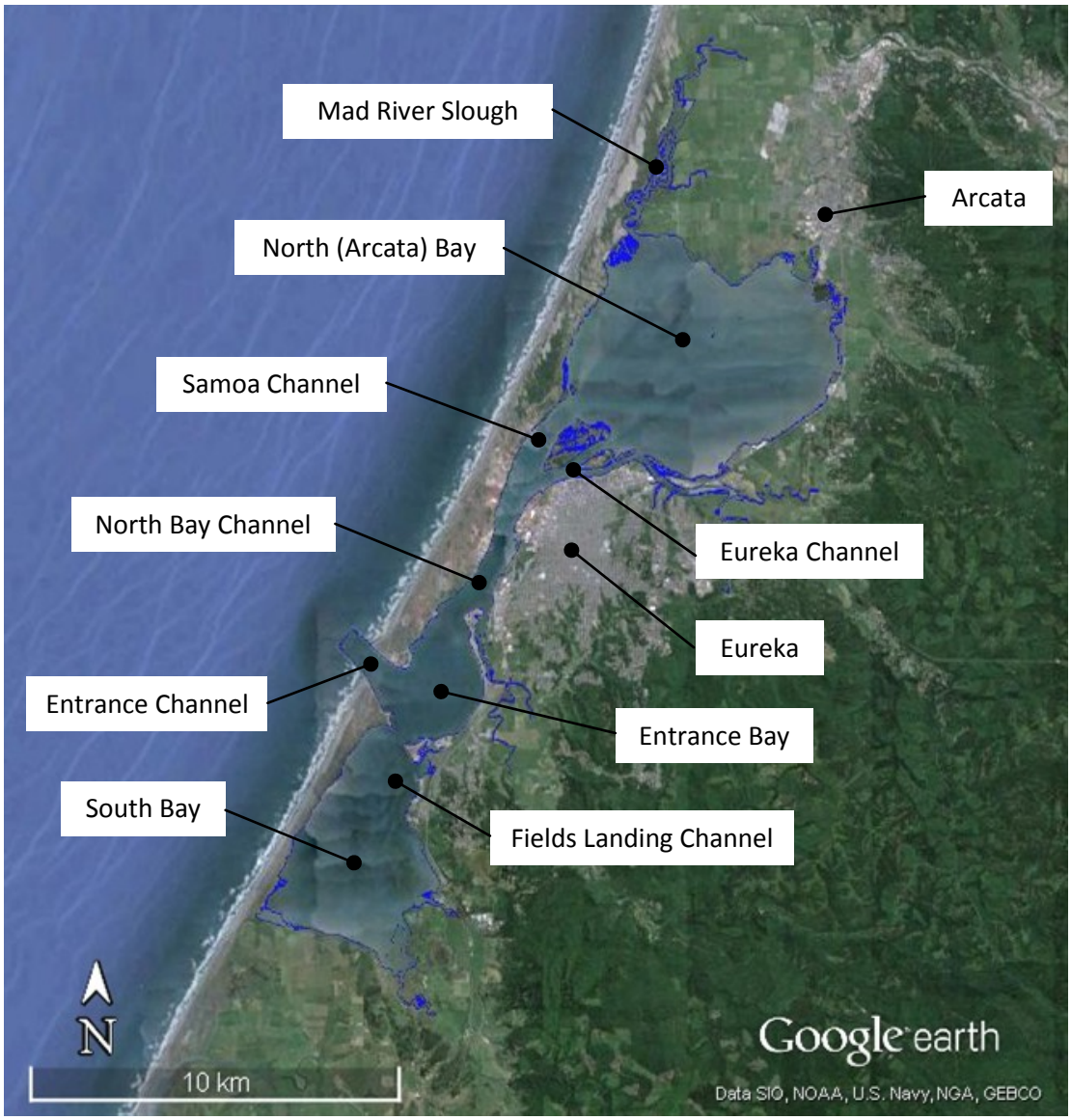

Figure 1-2 Humboldt Bay physical setting and mean high water edge (blue line).

Humboldt Bay contains three distinct bays (Figure 1-2), Entrance Bay, North (or Arcata) Bay, and South Bay (Costa 1982; Costa and Glatzel, 2002). Entrance Bay is connected to the ocean through the Entrance Channel, which is maintenance dredged by the U.S. Army Corps of Engineers. South Bay is directly connected to Entrance Bay through a natural constriction and the dredged Fields Landing Channel. North Bay is connected to Entrance Bay via the long, narrow dredged North Bay Channel. The North Bay Channel splits into the dredged Samoa and Eureka Channels, just before connecting with North Bay.

Humboldt Bay is relatively shallow, with 70% of the bay comprised of tidal mud flats that are exposed during low tide (Costa, 1982). The mud flats are predominately in North and South Bays, and only Entrance Bay and the lower portions of North Bay Channel maintain an

approximate constant surface area over a tide cycle. The water surface area of Humboldt Bay is approximately 64.8 km^2 at high tide and 20.7 km^2 during low tide (Costa, 1982).

The drainage basin of Humboldt Bay is approximately 578 km^2, a relatively small basin for a bay of its size. Although a number of small streams flow into the bay, the annual freshwater input to the bay is small, on the order of the tidal prism (Costa, 1982). The tidal prism is approximately 9.63 to 9.91 x 10^7 m^3 during a spring tide range and about 70% less over a mean tide range (Costa and Glatzel, 2002). North Bay contributes approximately 50% of the tidal prism, and about 30% for South Bay.

Humboldt Bay tides are mixed semidiurnal, and show tidal amplification and phase lag with distance from the entrance (Costa, 1982; Costa and Glatzel, 2002). Due to the small freshwater inflow, the general circulation of Humboldt Bay is dominated by tidally driven flows modified by the bathymetry (Costa, 1982), with estuarine conditions typically only found within the small stream mouths and slough channels (Costa and Glatzel, 2002). The general circulation patterns can be affected on daily and seasonal time scales by waves entering through Entrance Channel (primarily influencing Entrance Bay), internally generated wind waves, and density differences (Costa, 1982). Humboldt Bay is typically well mixed vertically, and normally consists of unstratified marine water (Costa and Glatzel, 2002).

Previous Humboldt Bay Sea Level Rise Mapping

A previous study conducted by the Pacific Institute (Herberger et al., 2009) mapped flood and coastal erosion hazard zones along the California coast for year 2000 existing conditions and year 2100 with 1.4 m (55 inches) of SLR based on the Cayan et al. (2009) SLR estimate for the Intergovernmental Panel on Climate Change (IPCC) A2 emission scenario. Phillip Williams and Associates Ltd. (2009), now ESA PWA, provided the coastal erosion hazards assessment, and compiled a statewide Base Flood Elevations (BFE) layer to support the flood hazard analysis conducted by Pacific Institute. As defined by FEMA, the BFE is the 1% (100-yr) annual chance flood elevation, and for coastal areas is the 1% total water level (TWL) which consists of the still water elevation (SWL) and wave effects. The BFE layer consisted of published FEMA BFEs for California, with data gaps filled using professional judgment and/or local knowledge and experience. The Pacific Institute flood hazard maps developed for Humboldt Bay used a single water elevation value (bathtub approach) to map flood zones in the bay. Review of the BFE layer (available at http://www2.pacinst.org) indicates that the mapped year 2000 BFE value was 2.90 m (9.5 ft) referenced to the North American Vertical Datum of 1988 (NAVD88), and the year 2100 BFE value would have been 4.3 m (2.9 m + 1.4 m SLR). Since the California Coastal DEM was not available until 2012, it was assumed that the flood hazard maps produced by Pacific Institute in 2009 for Humboldt Bay relied on the USGS National Elevation Dataset 10-m resolution topography, which has a stated vertical accuracy of ±7.5 m (Herberger et al., 2009).

General SLR Hydrodynamic Modeling and Inundation Mapping Approach

The Humboldt Bay SLR modeling and inundation mapping conducted in this study was built from the general approach used by Knowles (2010) for similar work done in San Francisco Bay. A hydrodynamic model was used to predict water levels within the existing shoreline of Humboldt Bay for five SLR scenarios: year 2012 existing sea levels and half-meter SLR increments of 0.5, 1.0, 1.5 and 2.0 m. The hydrodynamic model was forced by a 100-yr long stationary hourly sea level height series developed for Crescent City tide gauge. The 100-yr hourly series accounts for astronomical tides, and varying effects including wind, sea level pressure, and El Niño variability. The 100-yr series was incremental adjusted for each half-meter SLR scenario. Each hydrodynamic model simulation produced 100 years of predicted water levels throughout the bay. Estimates of average high water levels and annual exceedance probabilities of extreme high water levels were determined bay-wide for each of the five SLR scenarios.

Using the model results, inundation vulnerability maps of areas surrounding Humboldt Bay vulnerable to inundation from existing and future sea levels were produced for the estimated average water levels and extreme high water level events from the five SLR scenarios. The inundation maps identified areas surrounding Humboldt Bay currently protected from inundation by the shoreline, levees or other barriers, but are vulnerable and at risk to flooding from future sea levels. The inundation vulnerability mapping relied on the recent high resolution California Coastal DEM (PWA, 2014).

Disclaimer

The sea level rise modeling, analysis, and inundation vulnerability mapping conducted in this study are intended for use as planning-level tools to illustrate the areas surrounding Humboldt Bay vulnerable to existing and future sea levels. The inundation vulnerability maps identify potential future inundation conditions that could occur if nothing is done to adapt to, or prepare for sea level rise.

The 100-year extreme high water surface elevations presented in this report do not represent what FEMA defines as the 1% annual base flood elevation, which includes wave effects. The extreme high water level events presented in this report correspond approximately to what FEMA defines as still water elevations.

Acknowledgments

This study was funded by the State Coastal Conservancy, and sponsored by the Coastal Ecosystems Institute of Northern California. The principal author, Jeff Anderson, would like to acknowledge the following individuals. First, a special thanks to Susan Schlosser who's diligence and drive for all things Humboldt Bay paved the way for this study. Thanks to Corin Pilkington of NHE for development of the inundation vulnerability maps. Thanks to the

following individuals who reviewed and commented on this report in draft form: Jill Demers, CEINC; Joel Gerwein, SCC; Dr. Sharon Kramer, CEINC; Darren Mierau, CEINC; Rose Patenaude, NHE; Becky Price-Hall, CEINC; Hank Seemann, Humboldt County; Susan Schlosser, CEINC; and Dr. Frank Shaughnessy, CEINC. Thanks to Robert Willis for providing initial feedback on the modeling approach for this study, and Whelan Gilkerson of PWA for development of the Humboldt Bay digital elevation model (DEM). Finally, thanks to Aldaron Laird of Trinity Associates for always asking questions.

2 Sea Level Change in the Humboldt Bay Region

The Humboldt Bay region, which for this report includes the coasts of Humboldt and Del Norte Counties, is experiencing the combined effects of global sea level rise, regional sea level height variability from seasonal to multidecadal ocean-atmosphere circulation dynamics (e.g. El Niño Southern Oscillation), and relatively large tectonic vertical land motions associated with the Cascadia subduction zone (CSZ) (Figure 2-1). These large tectonic motions along the southern CSZ create the highly variable and opposing sea level trends observed between Humboldt Bay and Crescent City. Recent estimates of land subsidence by Patton et al. (2014) indicate that Humboldt Bay has the highest local sea level rise rate in California, approximately two to three times higher than the long-term global rate. In contrast, the land in Crescent City (109 km north) is uplifting faster than long-term global sea level rise, which causes a negative or decreasing local sea level rise rate.

The purpose of this chapter is to provide an overview of global and regional sea level change, with an emphasis on the physical processes locally effecting sea levels in the Humboldt Bay region. This overview relies on the climate and sea level change literature, specifically the 2013 Intergovernmental Panel on Climate Change (IPCC) Fifth Assessment Report, the 2012 National Resource Council (NRC) Sea Level Rise for the Coasts of California, Oregon, and Washington report, and the scientific and technical literature specific to the U.S. Pacific Northwest (PNW) coast (Northern California (north of Cape Mendocino), Oregon and Washington), and the Humboldt Bay region.

General Concepts and Definitions

Mean Sea Level

Mean sea level (MSL) is the average ocean level at a specific location over a known period of time. When MSL is estimated at a tide gauge from the hourly sea level height record over the 19-year National Tidal Datum Epoch (NTDE) period, it is known as the MSL tidal datum. The current tidal epoch is the 1983-2001 NTDE. MSL can change (rise or fall) over temporal and global, regional and local spatial scales.

Global Mean Sea Level

Global (or eustatic) mean sea level (GMSL) is the average height of the earth's oceans, and GMSL changes globally due to (1) changes in the shape of the ocean basins, (2) a change in ocean volume due to changes in the total mass of water in the ocean (barystatic), and (3) a change in ocean volume from changes in ocean water density (steric) (IPCC, 2013a). Thermosteric refers to density changes from ocean temperature changes, while halosteric defines density changes from changes in ocean salinity.

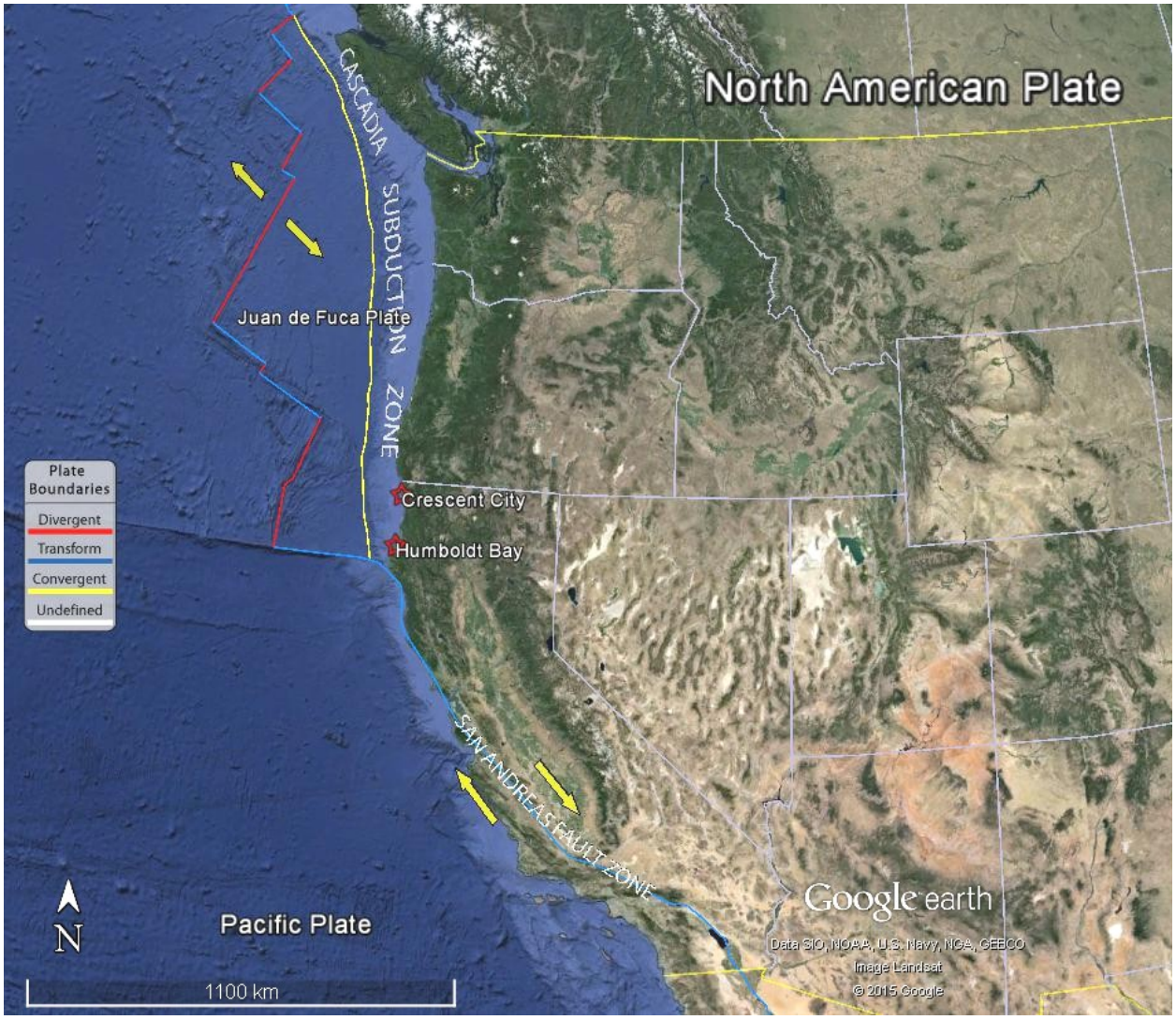

Figure 2-1 Tectonic plate boundaries along the U.S. west coast, and the location of Humboldt Bay and Crescent City relative to the Cascadia subduction zone. Tectonic boundary data downloaded from http://earthquake.usgs.gov/learn/kml.php.

Long-term reconstructions of GMSL change (e.g. Church and White, 2011) generally rely on the longest tide gauge records located on relatively stable land (Zervas, 2013), which are then adjusted for ocean basin changes, such as the land motion associated with the global glacial isostatic adjustment.

Regional Mean Sea Level

Regionally, sea level change may differ from GMSL due to meteorological effects (for example storms) and natural climate variability, such as the El Niño Southern Oscillation, which alters surface winds, ocean heating, and ocean currents (NRC, 2012; Church et al., 2013). Regional mean sea level (ReMSL) is the average sea level over a region of the earth's oceans, such as the

U.S. west coast. In this report, ReMSL does not include the effects of vertical land motion, such as plate tectonic motion.

Relative Sea Level

Relative sea level (RSL), or local sea level, is the sea level measured by a tide gauge relative to a specific point on land. Tide gauges measure the combined effects of ocean volume change (GMSL), ocean and climate variability (ReMSL), and vertical land motion. The change in RSL is what coastal areas experience, and is the quantity used for assessing and planning for the coastal impacts from sea level change (NRC, 2012; Church et al., 2013).

Vertical Land Motion

Global, regional and local vertical land motions (VLM) effect RSL change, and are responsible for most of the regional RSL trend differences observed between tide gauges (Zervas, 2009). Examples of VLM include glacial isostatic adjustment, plate tectonic land-level changes (seismic and interseismic), and land subsidence (e.g. soil compaction and groundwater extraction).

Glacial isostatic adjustment (GIA) is the deformation of the earth in response to melting of the large continental ice sheets that covered much of North America and Europe (Peltier, 1990), during the last glacial maximum that occurred about 20,000 years ago (Kominz, 2001). Estimates of GMSL rise trends are generally adjusted for vertical GIA using GIA models. For example, Peltier (2002, 2009) estimates the global average GIA at -0.3 mm/yr (a downward VLM).

Regional and local VLM, such as tectonic land-level changes, can be much larger than those associated with GIA models (Zervas, 2013). Researchers have documented interseismic tectonic uplift rates from plate locking along the CSZ that are an order-of-magnitude greater than the global GIA rate (Mitchell et al., 1994; Burgette et al., 2009). Along the PNW coast, the tectonic land-level changes associated with the CSZ strongly affect RSL changes, indicating both submergent and emergent stretches of coast (Komar et al., 2011).

Global Climate System Change

In 2013, the IPCC completed its Fifth Assessment Report (AR5). The AR5 builds upon the 2007 IPCC Fourth Assessment Report (AR4), and considers the climate science and research findings since AR4. Conclusions from the AR5 climate change science shows (95% confidence) that human activity is the dominant cause of the observed global climate system warming since the mid-20th century. Climate change will undoubtedly affect global climate such as temperature and precipitation patterns, ocean temperatures and chemistry, ocean-climate variability, and sea level rise. The following excerpts are key climate system change summary statements from the IPCC AR5 Summary for Policymakers report (IPCC, 2013b).

- "Each of the last three decades has been successively warmer at the Earth's surface than any preceding decade since 1850 (Figure 2-2). In the northern hemisphere, 1983-2012 was likely the warmest 30-year period of the last 1400 years (medium confidence)."

- "Ocean warming dominates the increase in energy stored in the climate system, accounting for more than 90% of the energy accumulated between 1971 and 2010 (high confidence). It is virtually certain that the upper ocean (0−700 m) warmed from 1971 to 2010, and it likely warmed between the 1870s and 1971."

- "Over the last two decades, the Greenland and Antarctic ice sheets have been losing mass, glaciers have continued to shrink almost worldwide, and Arctic sea ice and Northern Hemisphere spring snow cover have continued to decrease in extent (high confidence)."

- "The rate of sea level rise since the mid-19th century has been larger than the mean rate during the previous two millennia (high confidence). Over the period 1901 to 2010, global mean sea level rose by 0.19 [0.17 to 0.21] m."

- "The atmospheric concentrations of carbon dioxide, methane, and nitrous oxide have increased to levels unprecedented in at least the last 800,000 years. Carbon dioxide concentrations have increased by 40% since pre-industrial times, primarily from fossil fuel emissions and secondarily from net land use change emissions. The ocean has absorbed about 30% of the emitted anthropogenic carbon dioxide, causing ocean acidification (Figure 2-3)."

- "Total radiative forcing is positive, and has led to an uptake of energy by the climate system. The largest contribution to total radiative forcing is caused by the increase in the atmospheric concentration of CO_2 since 1750."

- "Continued emissions of greenhouse gases will cause further warming and changes in all components of the climate system. Limiting climate change will require substantial and sustained reductions of greenhouse gas emissions."

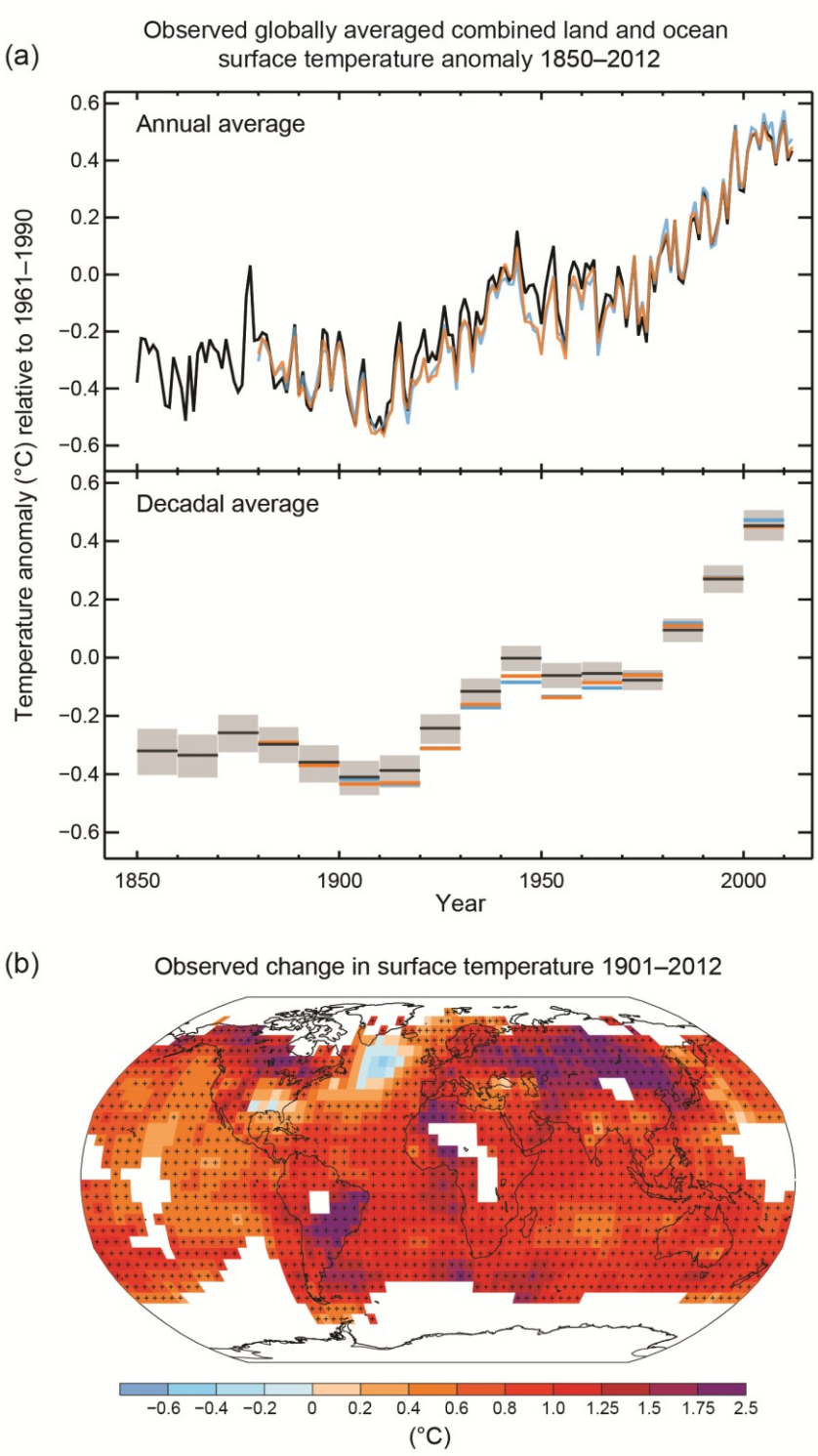

Figure 2-2 (a) Observed 1850 to 2012 global mean combined land and ocean surface temperature anomalies (relative to the mean of 1961-1990) from three datasets. Top panel is the annual mean values, and bottom panel are the decadal mean values with uncertainty for one dataset (black). (b) Map of observed surface temperature change (1901 to 2012) derived from temperature trends (orange line in panel a). (Figure from IPCC (2013b), Figure SPM.1)

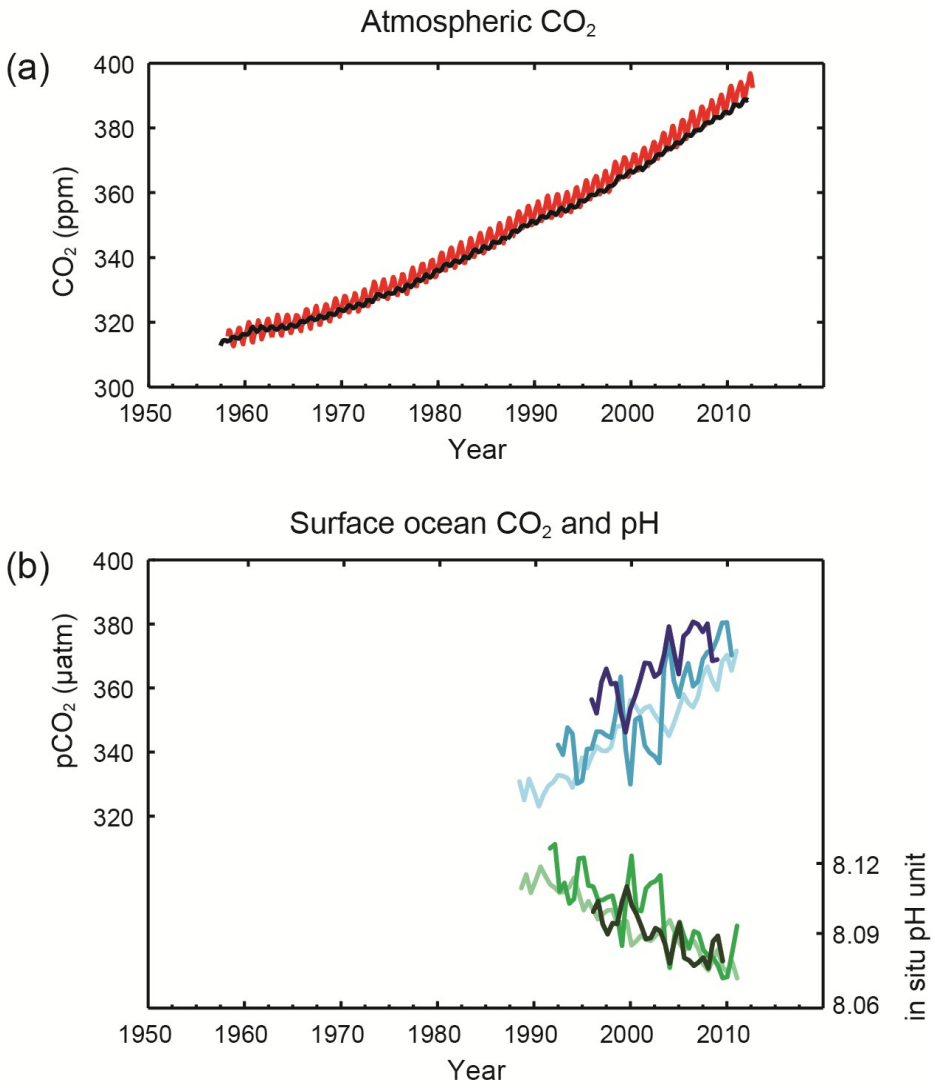

Figure 2-3 (a) Observed atmospheric carbon dioxide (CO_2) concentrations for Mauna Loa (red line) and South Pole (black line) since 1958. (b) Ocean surface observed partial pressure of dissolved CO_2 (blue lines), and in situ pH (green lines) which is an indicator of ocean acidification. Measurements from Atlantic Ocean (dark blue and dark green, and blue and green) and Pacific Ocean (light blue and light green). (Figure from IPCC (2013b), Figure SPM.4)

Past and Present Global Sea Level Rise

Global sea levels have been increasing for 20,000 years since the last ice age (Russell and Griggs, 2012; Kominz, 2001), although at relatively low rates (~ 0.1 mm/yr) over the last two millennia (NRC, 2012). There is high confidence, based on proxy records (e.g. salt marsh sediments) and instrumental sea level data, that GMSL rise increased in the late 19th to early 20th century from relatively low rates over the previous two millennia to higher rates today (Church et al., 2013). As noted earlier, sea levels are increasing globally due to thermal

expansion from ocean warming and increases in ocean mass from melting land ice caused by warming of the earth's climate.

Reconstructions of late 19th, 20th and early 21st century GMSL rise have been made by numerous investigators (e.g. Jevrejeva et al., 2008; Church and White, 2011; Ray and Douglas, 2011) using tide gauge records, starting in the late 1800s, and the more recent satellite-based radar altimeter measurements since the early 1990s. Only results of the reconstructed GMSL time series (1880 to 2010) and satellite altimeter data (1992 to 2010) of Church and White (2011) are presented in this study (Figure 2-4 and Table 2-1). As noted by Rhein et al. (2013), other long-term GMSL reconstructions (e.g. Jevrejeva et al., 2008; Ray and Douglas, 2011; and others) provide similar long-term rates of GMSL rise as compared to the Church and White (2011) estimate. To account for ocean volume variability, the Church and White (2011) GMSL estimates removed the GIA signal and adjusted sea levels for atmospheric pressure variations (inverse barometer effect).

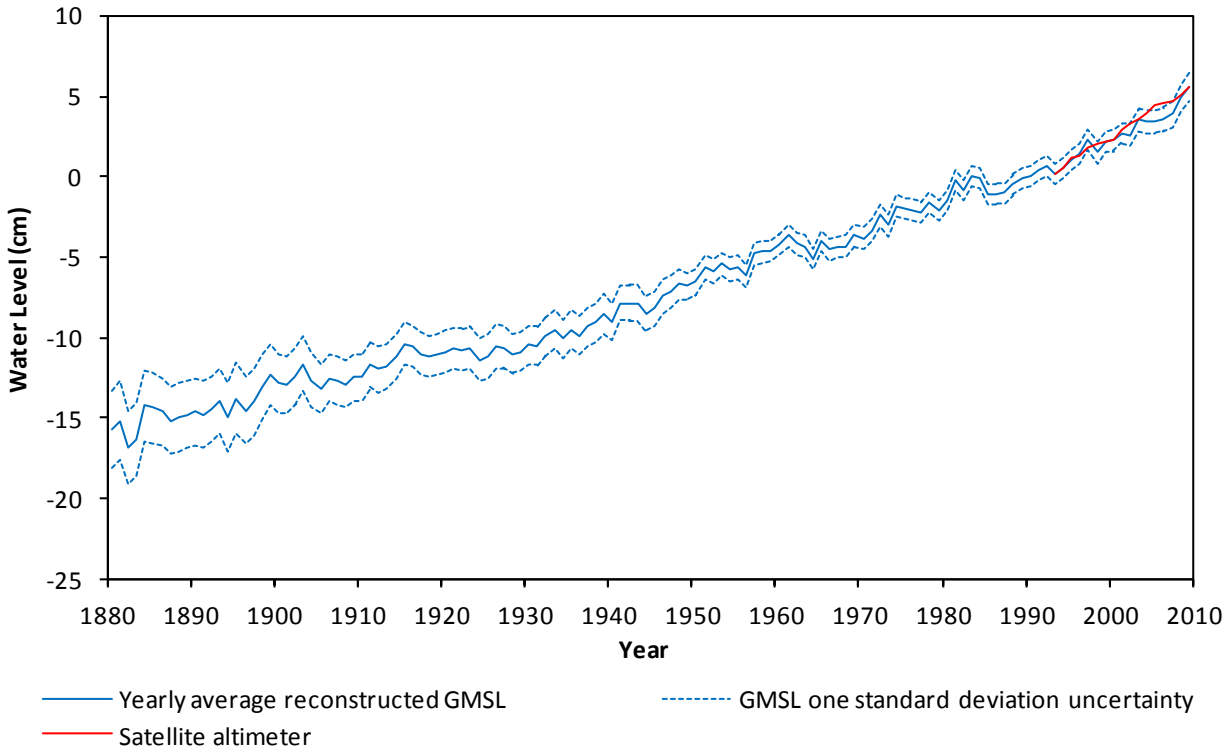

Figure 2-4 Yearly average reconstructed global mean sea level (GMSL) for 1880 to 2010 with one standard deviation uncertainty bounds, and satellite altimeter data for 1993 to 2010 (Church and White, 2011). The reconstruction is set to zero in 1990, and satellite altimeter data match the reconstructed time series over 1993. Data downloaded from http://www.cmar.csiro.au.

Table 2-1 Estimated global mean sea level (GMSL) rise trends and uncertainty range for different time periods. Data from Church and White (2011), and Table 3.1 of Rhein et al. (2013).

Time Period	GMSL Rise Trend (mm/yr)	Source
1901 to 1990	1.5 [1.3 to 1.6]	Tide gauge reconstruction
1901 to 2010	1.7 [1.5 to 1.9]	Tide gauge reconstruction
1936 to 2010	1.8 [1.5 to 2.1]	Tide gauge reconstruction
1961 to 2010	1.9 [1.5 to 2.3]	Tide gauge reconstruction
1971 to 2010	2.0 [1.5 to 1.9]	Tide gauge reconstruction
1993 to 2010	2.8 [2.3 to 3.3]	Tide gauge reconstruction
1993 to 2010	3.2 [2.8 to 3.6]	Satellite altimetry data

The 2013 IPCC AR5 states it is very likely (90 to 100% probability) that the rate of GMSL rise between 1901 and 2010 was 1.7 ± 0.2 mm/yr, and increased to 3.2 ± 0.4 mm/yr between 1993 and 2010 (Rhein et al., 2013). During the 20th century, there is high confidence that the dominant contributors to GMSL rise were ocean thermal expansion and glacier mass loss (Church et al., 2013).

The IPCC AR5 scientific work further documented the observed contributions to GMSL rise for the 1993 to 2010 period from ocean thermal expansion, melting land ice, and land water storage (Table 2-2), with thermal expansion and land ice melting being the dominant contributors (Rhein et al., 2013; Church et al., 2013).

To better understand GMSL change and contributions a number of global observation systems have been deployed over the last two decades, which include (1) satellite radar altimetry to measure sea level height, (2) the Argo Project global ocean array of free-drifting profiling floats that measure temperature and salinity in the upper 2,000 m of the ocean, and (3) the Gravity Recovery and Climate Experiment (GRACE) satellites that measure the Earth's gravity field and can detect mass changes in the oceans and ice sheets. Between 1993 and 2010, the total observed contributions to GMSL rise was estimated at 2.8 ± ~0.5 mm/yr, which is consistent with the tide gage reconstructions (2.8 ± 0.5 mm/yr) and the satellite altimetry data (3.2 ± 0.4 mm/yr) for the same period (Table 2-2).

Table 2-2 Observed global mean sea level (GMSL) rise trends, observed contributions to GMSL rise and model-based contributions to GMSL rise for the 1993 to 2010 period based on the 2013 IPCC AR5. Uncertainties are 5 to 95%. GMSL rise trends from Church and White (2011); observed contributions from Table 3.1 of Rhein et al. (2013); observed and model-based contributions from Table 13.1 of Church et al. (2013).

Source	Trend/Contribution for 1993 to 2010 (mm/yr)
Observed GMSL rise	
Tide gauge reconstruction	2.8 [2.3 to 3.3]
Satellite altimeter data	3.2 [2.8 to 3.6]
Observed GMSL Contributions	
Ocean thermal expansion	1.1 [0.8 to 1.4]
Glaciers (except in Greenland and Antarctica)	0.76 [0.39 to 1.13]
Greenland ice sheet and glaciers	0.33 [0.25 to 0.41]
Antarctic ice sheet	0.27 [0.16 to 0.38]
Land water storage	0.38 [0.26 to 0.49]
Total of contributions	**2.8 [2.3 to 3.4]**
Modeled GMSL Contributions	
Ocean thermal expansion	1.49 [0.97 to 2.02]
Glaciers (except in Greenland and Antarctica)	0.78 [0.43 to 1.13]
Glaciers in Greenland	0.14 [0.06 to 0.23]
Total of contributions including land water storage	**2.8 [2.1 to 3.5]**

As noted by Church et al. (2013), the ability to reproduce observed GMSL change since 1993 from the observed ocean budget (ocean mass and thermosteric changes) demonstrates a significant advancement since the 2007 IPCC AR4 (Meehl et al., 2007) in understanding the contributions to GMSL change (Figure 2-5).

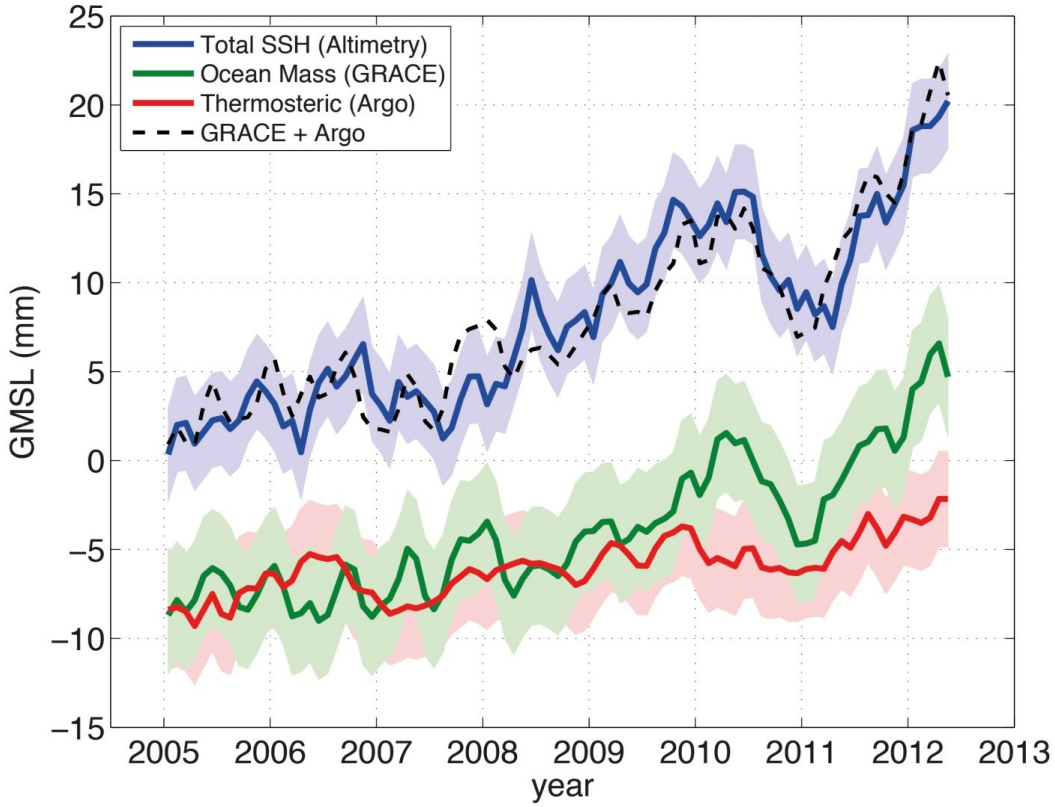

Figure 2-5 Observed global mean sea level (GMSL) from satellite altimetry (blue line), observed ocean mass changes from GRACE satellites (green line), and observed thermosteric sea level change from Argo floats (red line) for 2005 to 2012. The dashed black line is the summed contributions of GRACE and Argo observations. (Figure from Church et al. (2013), Figure 13.6)

Past and Present Regional Sea Level Rise

Spatial patterns in sea level change can differ from GMSL values due to regional ocean and climate processes, such as El Niño Southern Oscillation, which effects ocean circulation patterns on seasonal to multi-decadal timescales and redistributes ocean mass and temperature (Cayan et al., 2008; Bromirski et al., 2011; NRC, 2012; Church et al., 2013; Rhein et al., 2013). For example, Figure 2-6 shows the monthly MSL trends, as reported by National Oceanic Atmospheric Administration (NOAA) Center for Operational Oceanographic Products and Services (CO-OPS) for three long-term tide gauge sites (Seattle, San Francisco and San Diego) along the U.S. west coast that are located on relatively tectonically stable ground (Cayan et al., 2008; Burgette et al., 2009; Bromirski et al., 2011). Each tide gauge record is over 100-yrs long, beginning in 1898 for Seattle, 1897 for San Francisco, and 1906 for San Diego, which coincides

well with the 1901 to 2010 GMSL reconstruction period of Church et al. (2011). The RSL rise trends for these three U.S. west coast tide gauge locations are very consistent, ranging from 1.89 to 2.04 mm/yr (average ~2.0 mm/yr), which is greater (18% increase) than the 1901 to 2010 GMSL trend of 1.7 mm/yr (Table 2-1). This implies that over the instrument period, ReMSL rise along the U.S. west coast has been greater than GMSL rise for the same general period.

Processes Affecting Regional Sea Level Rise on the U.S. West Coast

The NRC (2012) report addressed sea level variability along the coasts of California, Oregon and Washington. Monthly mean sea levels vary along the MSL trend line (Figure 2-6) due to natural climate and ocean variability. The following subsections briefly summarize the dominant processes affecting ReMSL change in the Pacific Ocean along the U.S. west coast, taken from the NRC (2012) report and other scientific literature.

Seasonal to Interannual Variability

The El Niño Southern Oscillation (ENSO) is the most important coupled ocean-atmosphere phenomenon that causes seasonal to interannual timescale global climate variability (Wolter and Timlin, 2011). ENSO is the dominant cause of sea level variability along the U.S. west coast (Komar et al., 2011; Bromirski et al., 2011; NRC, 2012), with higher sea levels during the warmer El Niño phase, and lower levels during the cooler La Niña phase (Figure 2-7). Strong El Niño events effect wind and ocean circulation, reducing upwelling and producing warmer than normal ocean temperatures along the U.S. west coast, which can raise mean winter water levels by 0.2 to 0.3 m for several months (Komar et al, 2011). This winter seasonal increase is larger than the 20th century GMSL rise of 0.17 m (Table 2-1). El Niño events are generally associated with a more active winter storm period along the U.S. west coast (NRC, 2012).

Seasonal coastal current and wind patterns (e.g. upwelling) also produce seasonal variations in sea level heights (known as the average seasonal cycle) due to ocean temperature and density changes (Komar et al., 2011). Both ENSO and the average seasonal cycle will be discussed in more detail for the Humboldt Bay region in following sections of this chapter.

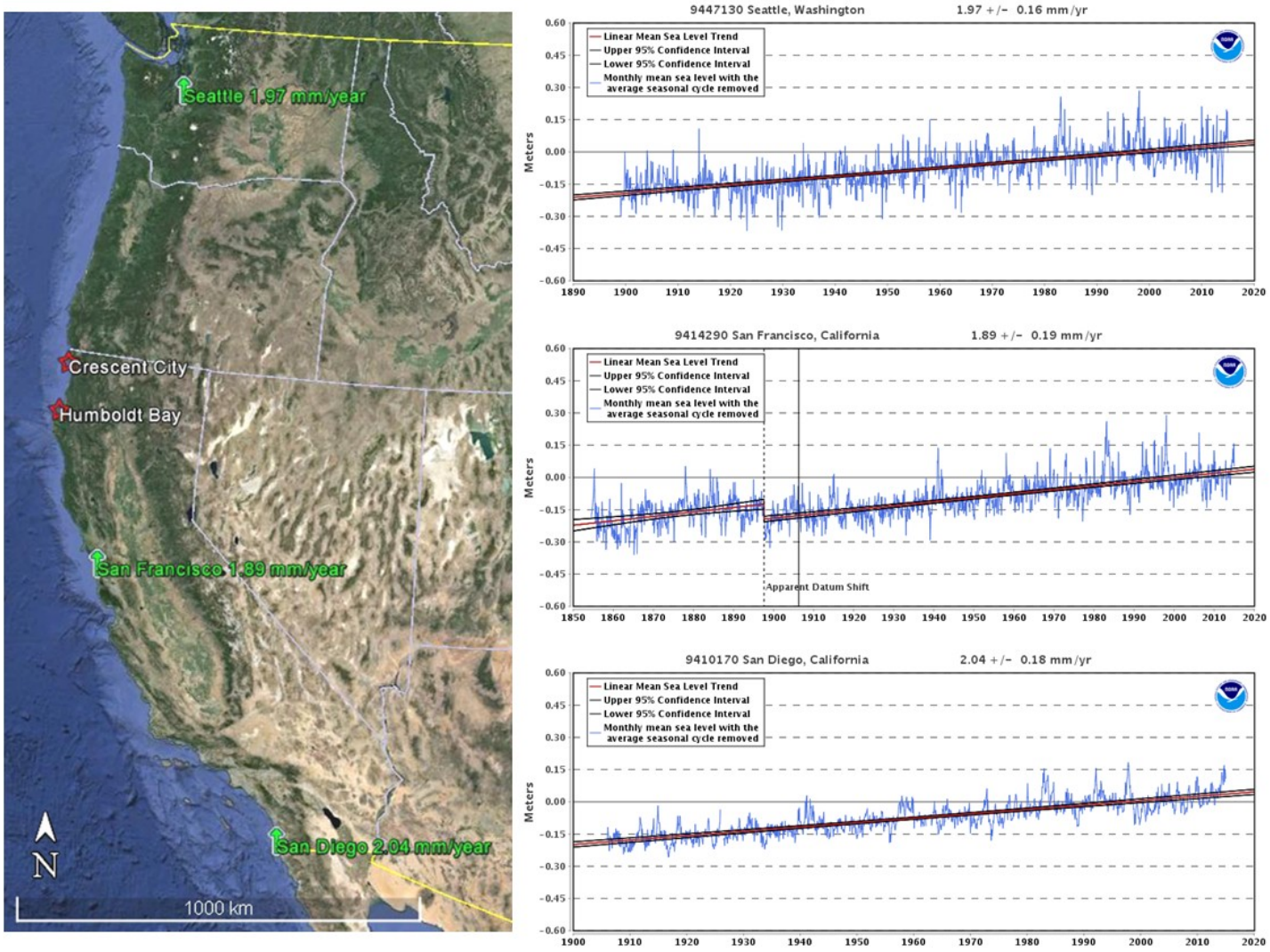

Figure 2-6 Observed monthly relative sea level (RSL) rise trends from NOAA tide gauge records for Seattle, San Francisco and San Diego. These tide gauge sites are located on relatively tectonically stable ground. Data and figures downloaded from NOAA CO-OPS at http://tidesandcurrents.noaa.gov.

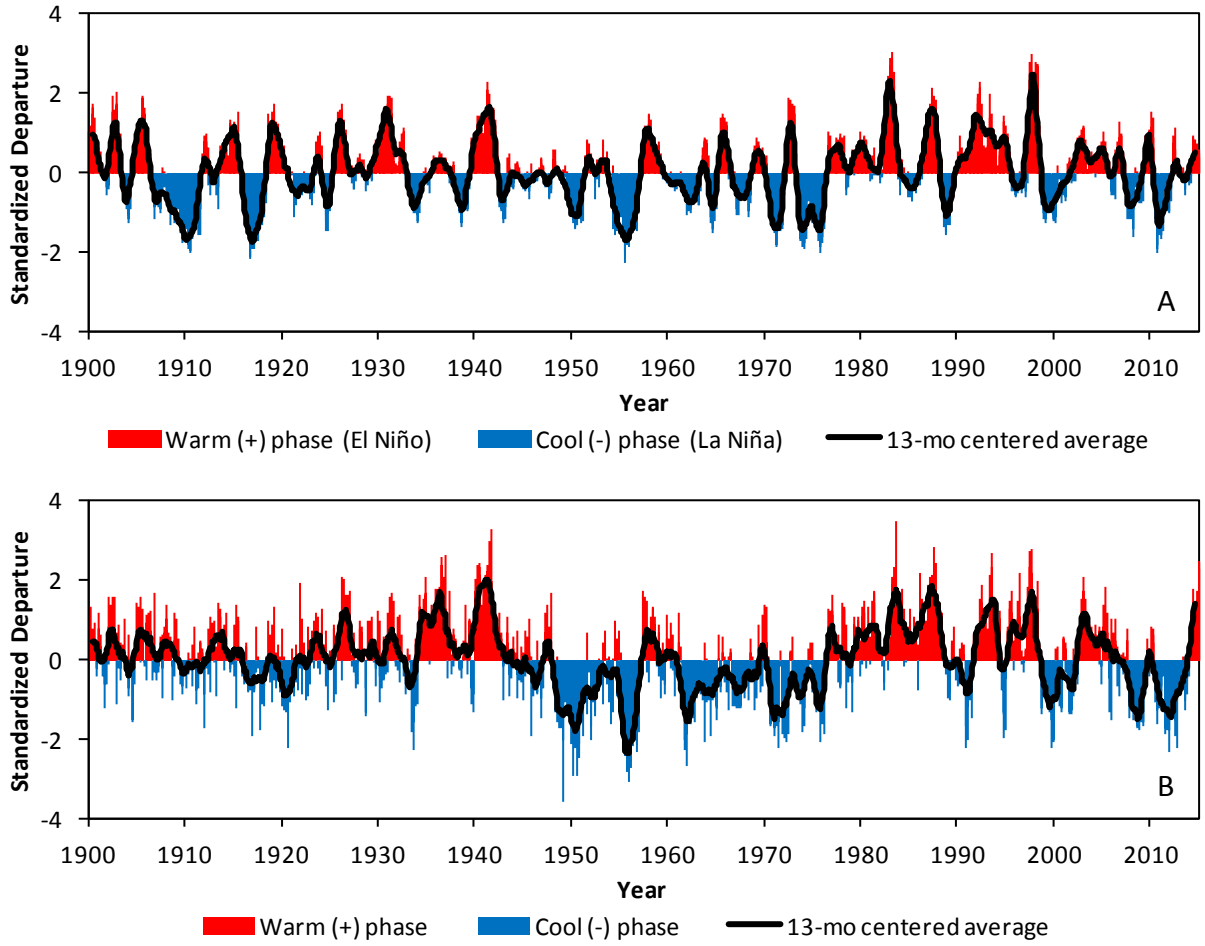

Figure 2-7 (A) Multivariate ENSO index (MEI), and (B) Pacific Decadal Oscillation (PDO) index from 1900 to March 2015. The black lines are 13-month centered average values. MEI index based on MEI.ext data from 1900 to 1949 (Wolter and Timlin, 2011), and MEI data from 1950 to March 2015 (Wolter and Timlin, 1993, 1998); MEI data downloaded from http://www.esrl.noaa.gov/psd/enso. PDO index data from 1900 to March 2015 (Mantua et al., 1997); PDO data downloaded from http://research.jisao.washington.edu/pdo. Refer to sources and links for details on how the MEI and PDO index's were computed.

Decadal and Longer Variability

The Pacific Decadal Oscillation (PDO) is described as an interdecadal ENSO like pattern of climate variability in the Pacific Ocean with warm and cool phases (Figure 2-7), which usually shifts phases on interdecadal timescales of about 20 to 30 years (Zhang et al., 1997; Mantua et al., 1997). The causes of the PDO are not well understood. During the warm (positive) phase the eastern Pacific Ocean warms and the western portion cools, and during the cool (negative) phase the opposite pattern develops. The NRC (2012) report noted that ENSO and PDO are not independent, with ENSO influencing the PDO (e.g. Newman et al., 2003), and the PDO

modulating ENSO (e.g. Vimont et al., 2009). For example, both the 1982-83 and 1997-98 large El Niño events correspond to the late 1970s to late 1990s warm (positive) phase of the PDO (Figure 2-7).

The PDO and the corresponding regional and basin-scale wind stress patterns have been associated with decadal to multidecadal sea level variability along the U.S. west coast (e.g. Bromirski et al., 2011; NRC, 2012). Bromirski et al. (2011) attributes suppression of the ReMSL trend along the U.S. west coast since the 1980s (Figure 2-6) to changes in the wind stress curl associated with the PDO regime shift in the mid-1970s (Figure 2-7). Furthermore, the regime shift from warm to cold phases in the late 1990s and late 2000s (Figure 2-7) may lead to a shift in the wind stress patterns and a resumption of ReMSL rise along the U.S. west coast (Bromirski et al., 2011).

Sea Level Fingerprints

Another process affecting ReMSL is the gravitational pull of the large glacier and ice sheet masses that draws ocean water closer and raises sea levels near the ice masses (NRC, 2012). As the land ice melts, water enters the ocean raising GMSL. However, the melting land ice decreases the gravitational pull on the ocean water due to the decrease in ice mass. The loss of modern land ice also causes land to uplift at the ice masses, but these land-level changes from modern ice melting are too far from the U.S. west coast to have an effect on sea level change (NRC, 2012). In contrast, the loss of the ancient ice sheets during the last glacial maximum caused the entire earth's land and ocean basins to deform (glacial isostatic deformation).

The gravitational and deformational responses to land ice melting and mass redistribution in the oceans produce regional patterns of sea level change known as sea level fingerprints (NRC, 2012; Church et al., 2013). The overall net effect of these fingerprints is that ReMSL or RSL will drop near the melting ice masses, and increase proportional to the distance from the ice masses.

The NRC (2012) report estimated the sea level fingerprint effects of the Alaska, Greenland, and Antarctica ice mass loss on the U.S. west coast for the 1992-2008 period. The estimated uniform sea level rise, without sea level fingerprints, along the U.S. west coast from the three ice masses was 0.79 mm/yr. Assuming fingerprint effects, the adjusted sea level rise rate at Neah Bay, OR was 0.46 mm/yr (42% reduction), at Eureka, CA was 0.60 mm/yr (24% reduction), and at Santa Barbara, CA was 0.68 mm/yr (14% reduction). The overall effect of the sea level fingerprints was to reduce sea level change from the uniform ice mass loss rate of 0.79 mm/yr along the U.S. west coast in a north to south direction.

Regional Sea Level Rise along the Cascadia Subduction Zone

To better understand the pattern of interseismic locking on the CSZ and quantify uplift rates, Burgette et al. (2009) assessed land elevation changes from benchmark survey records and sea level change at six NOAA tide gauges along the coasts of Oregon and northernmost California.

The tide gauges extended from Crescent City, CA to Astoria, OR. To infer tectonic uplift rates (i.e. VLM) from the RSL change determined at each tide gauge site, a ReMSL rise rate was added to each sites RSL rate. Burgette et al. (2009) determined an average sea level rise rate of 2.28 ± 0.20 mm/yr that represents an approximate 20th century ReMSL rise rate for the PNW coast along the CSZ. The ReMSL rate was based on the Seattle tide gauge record, which Burgette et al. (2009) assumed was tectonically stable, and a procedure between the six CSZ tide gauge sites and the Seattle record that generated the single regional value of 2.28 mm/yr over the observation period of the CSZ tide gauge records (~1925 to 2006).

As noted by Burgette et al. (2009), the 2.28 mm/yr ReMSL rise rate compared well to the 1950 to 2000 global sea level reconstruction of Church and White (2006), which had trend slopes for grid points offshore of the CSZ of 2.2 ± 0.30 mm/yr. Komar et al. (2011) further assessed the Burgette et al. (2009) ReMSL rate by comparing RSL rates for the six CSZ tide gauge records to the benchmark and Pacific Northwest Geodetic Array Global Positioning System (GPS) data, and concluded that the ReMSL rise rate of 2.28 mm/yr is reasonable for the PNW coast (Northern California, Oregon and Washington). Finally, the NRC (2012) study determined sea level rise rates for the Seattle tide gauge for the period of 1900 to 2008. The RSL rise rate for the Seattle tide gauge (2.01 mm/yr) was corrected for atmospheric pressure (0.09 mm/yr upward) and VLM determined from GPS data (0.20 mm/yr upward), providing an adjusted sea level rise rate of 2.30 mm/yr. This NRC (2012) adjusted sea level rise rate of 2.30 mm/yr for the Seattle tide gauge can be considered a regional value for the 1900 to 2008 period, which is consistent with the 2.28 mm/yr ReMSL rise rate determined by Burgette et al. (2009).

The 2.28 mm/yr ReMSL rise rate is 0.58 mm/yr greater (34% increase) than the 1901 to 2010 GMSL trend of 1.7 mm/yr (Table 2-1). This implies that the natural climate variability (ENSO and PDO), ocean dynamical processes, and gravitational mass redistribution has produced a greater ReMSL rise rate for the PNW coast within the CSZ that is approximately 34% greater than the GMSL rate for the same general period. The Burgette et al. (2009) rate of 2.28 mm/yr is used in this study to represent the historic ReMSL rise rate for the Humboldt Bay region.

Past and Present Relative Sea Level Rise

Tide gauges measure RSL change, the combined effects of sea level change and VLM. The measured sea level change includes (1) GMSL change, (2) ocean dynamic processes, natural climate variability, and sea level fingerprint effects that create ReMSL patterns, and other short-term local climate variability such as storm surge, wind stress effects, and changes in barometric pressure. As noted earlier, the VLM is responsible for most of the differences in RSL trends between regional tide gauge observations (Zervas, 2009).

Although the Crescent City and Humboldt Bay (North Spit) tide gauges are only separated by 109 km, the RSL trends for these gauges are in opposing directions (Figure 2-8), with Crescent City RSL having a downward trend while North Spit RSL has an upward trend. The relatively

large oscillations in RSL (monthly MSL values) around the RSL trend line are due to short-term weather variability (e.g. storms), natural climate variability (e.g. ENSO and PDO), and the average seasonal cycle as described previously. The downward RSL trend at Crescent City indicates this section of coast is emerging, with an uplift rate greater than the current GMSL and ReMSL rise rates. In contrast, the North Spit RSL trend is greater than the GMSL or ReMSL rise rates, indicating that Humboldt Bay is submergent, and in fact, has the highest RSL rise rate in California.

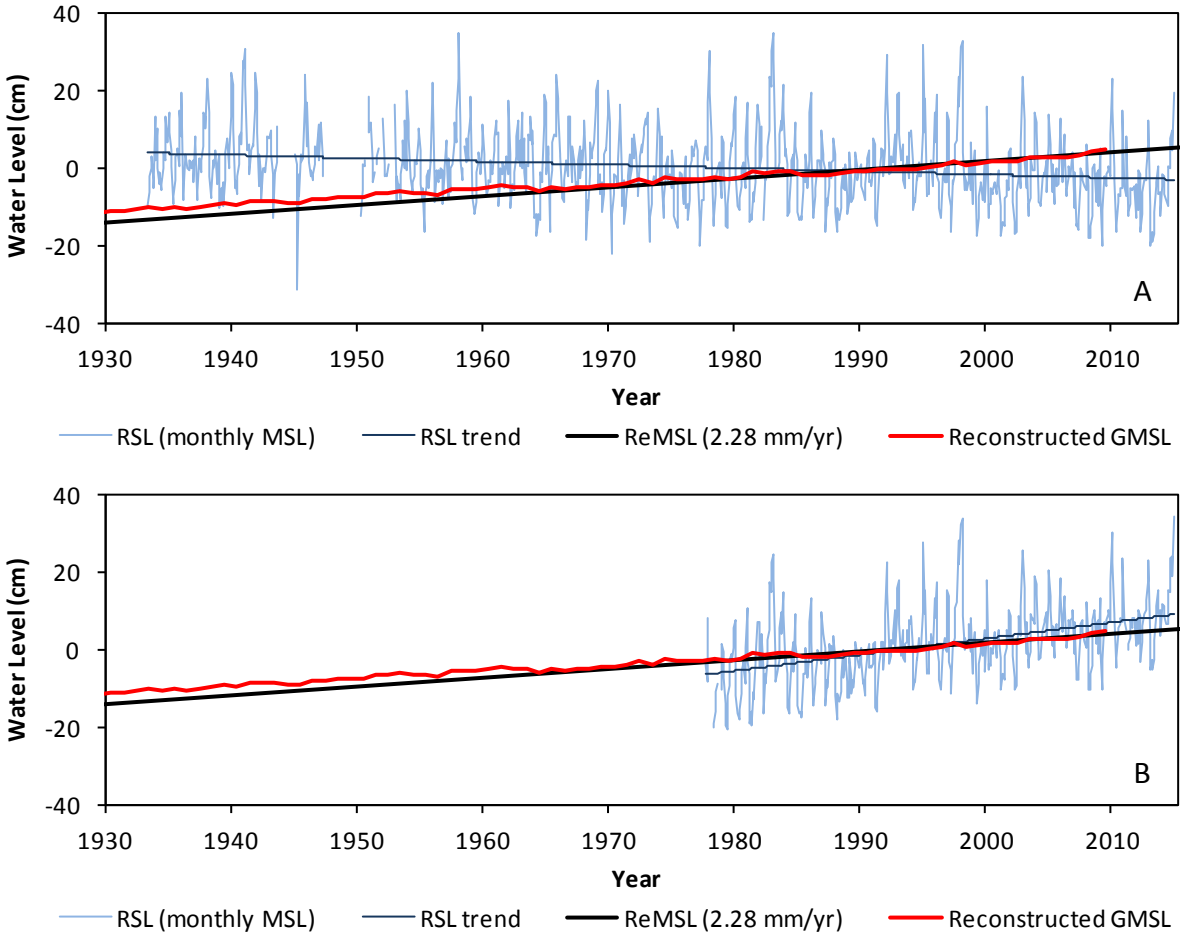

Figure 2-8 (A) Relative sea level (RSL) change for Crescent City tide gauge observations for 1933 to 2014 record. (B) RSL change for Humboldt Bay North Spit tide gauge observations for 1977 to 2014 record. RSL changes (light blue lines) are monthly MSL values relative to the MSL tidal datum (1983-2001 NTDE) for each tide gauge. RSL trends (dark blue lines) are the linear regression on the monthly MSL values. Regional mean sea level (ReMSL) trend (black line) is the Burgette et al. (2009) ReMSL rate of 2.28 mm/yr, set to zero on June 1992. Global mean sea level (GMSL) change (red line) is the Church and White (2011) yearly average reconstruction, set to zero in the middle of 1992.

Average Seasonal Cycle in the Humboldt Bay Region

The average seasonal cycle represents the long-term average repeatable variation in sea levels from the effects of seasonal cycles in climate patterns, ocean circulation, ocean volume density (steric) changes, and river discharge, with the steric density changes from temperature and salinity changes being the dominant factor (Zervas, 2009). In the Humboldt Bay region and PNW, winter ocean temperatures are warmer and thus less dense than summer temperatures and density, primarily due to upwelling that brings the deeper colder ocean water to the surface (Komar et al., 2011). The resulting average seasonal cycle (Figure 2-9) has higher MSL during the winter period and lower levels in the summer. In general, the seasonal cycle for Crescent City and North Spit tide gauges are similar, with a total average seasonal difference in water levels of approximately 17 cm. To demonstrate how El Niño events can affect average sea levels over extended periods, the mean monthly MSL for the 1983 El Niño are included on Figure 2-9, which shows that average monthly winter levels during this large El Niño were about 27 cm higher than normal.

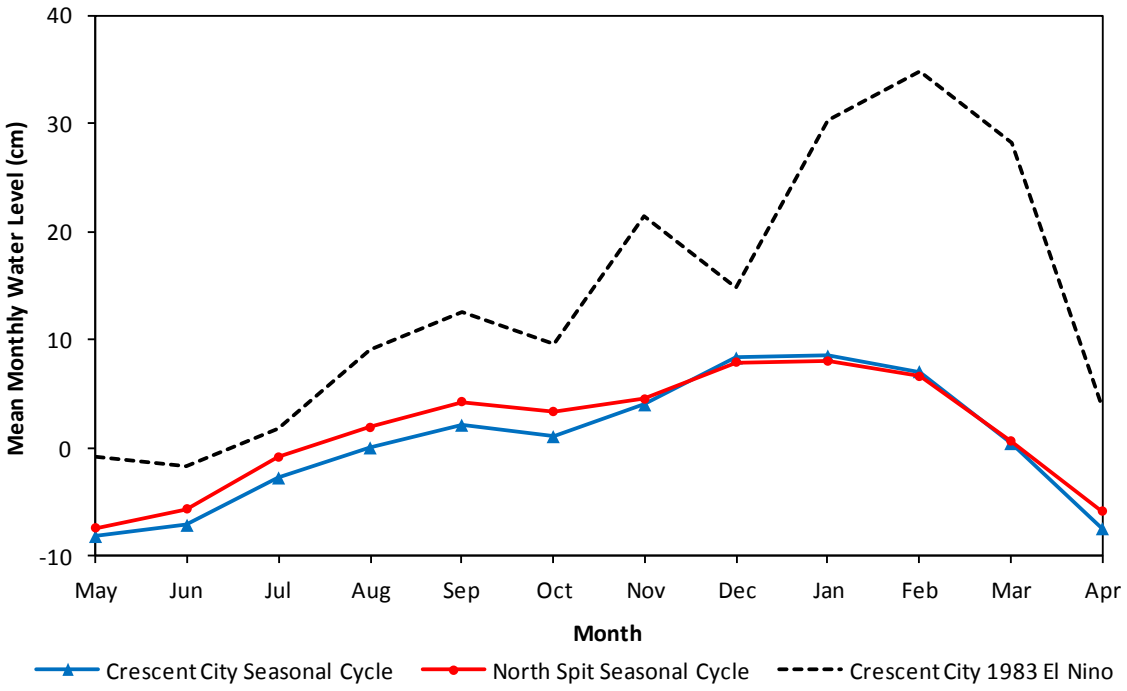

Figure 2-9 Long-term average seasonal cycles based on tide gauge observations for Crescent City 1933 to 2014 record (red line) and North Spit 1977 to 2014 record (blue line). The dashed black line is the mean monthly MSL for the 1983 El Niño.

Hydrodynamic modeling has shown that horizontal temperature gradients develop in the spring and summer periods in Humboldt Bay (Anderson, 2010). As solar radiation heats the bay water, horizontal gradients in temperature develop between the cold ocean water entering the bay

through the deeper Entrance Bay, and the warmer shallower waters of North Bay and South Bay. Model results show that North Bay and South Bay can be 4.1° C and 2.5° C warmer, respectively, than the colder water in Entrance Bay for the spring and summer months (Figure 2-10). This persistent temperature gradient in Humboldt Bay helps explain the elevated North Spit seasonal cycle values compared to Crescent City for the months of April to October (Figure 2-9). Even though the North Spit tide gauge is located in Entrance Bay and exposed daily to cold ocean water, the warmer less dense water in North and South Bays during the spring and summer still influences the North Spit seasonal cycle compared to Crescent City, whose orientation directly exposes the tide gauge to colder, denser ocean water during this period.

The seasonal temperature patterns simulated in North and South Bays appear to be opposite to the PNW Ocean, with warmer temperatures in the late spring, summer, and early fall periods than in the winter. Although not directly assessed in this study, the average seasonal cycle for North Bay and South Bay may be opposite of the North Spit and Crescent City tide gauges, due to the solar heating and warmer water temperatures in the shallow bays where thermal expansion could produce higher water levels during the warmer months.

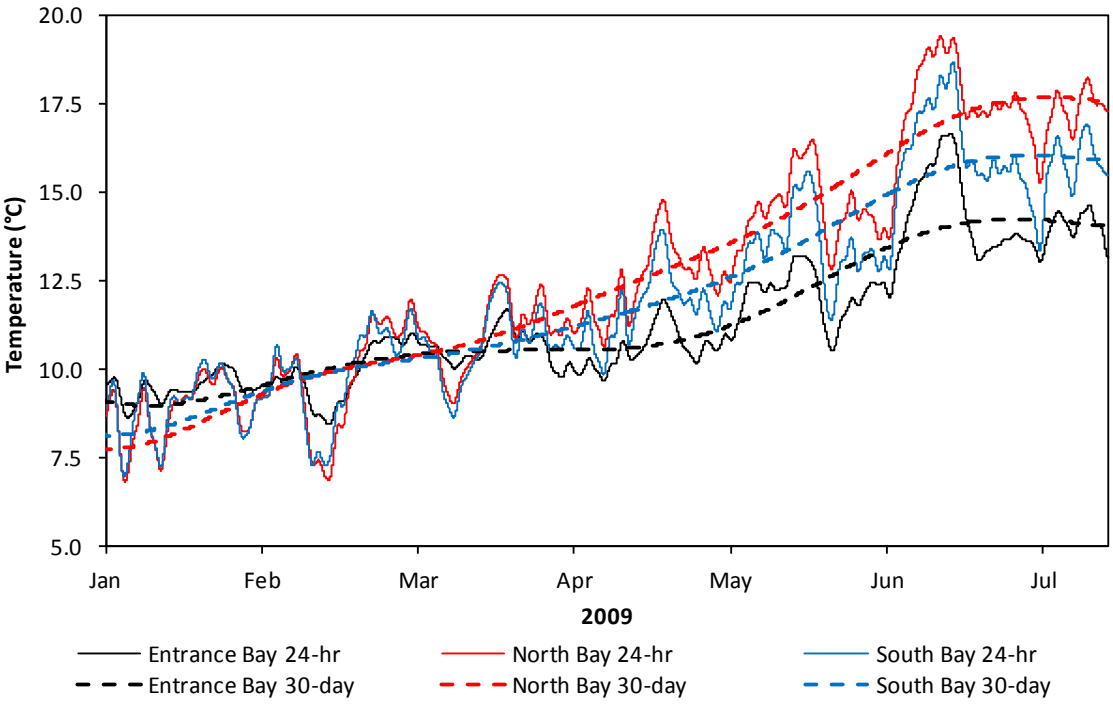

Figure 2-10 Simulated water temperature in Entrance Bay (black lines), North Bay (red lines), and South Bay (blue lines) from the Humboldt Bay hydrodynamic model for January to July 2009 (Anderson, 2010). Results are for 24-hr low-pass filtered (solid lines) and 30-day low-pass filtered (dashed lines) volume averaged temperatures for each distinct bay.

Relative Sea Level Rise and Vertical Land Motion Rates in the Humboldt Bay Region

As discussed earlier, the RSL rise rate at North Spit tide gauge is greater than both the GMSL and ReMSL rise rates due to land subsidence in and around Humboldt Bay. To better understand how tectonic land motions affect RSL rise in Humboldt Bay, Cascadia Geosciences was provided funding from the U.S. Fish & Wildlife Service Coastal Program (study plan at http://www.hbv.cascadiageo.org). Cascadia Geosciences (CG), along with Northern Hydrology and Engineering, Pacific Watershed Associates, and researchers from Humboldt State University, University of Oregon, and New Mexico State University are utilizing tide gauge observations, benchmark level surveys, and GPS data to evaluate tectonic VLM and RSL rates in Humboldt Bay. The tide gauge analysis consisted of evaluating water level observations at the NOAA Crescent City tide gauge (active), and five NOAA tide gauge sites in Humboldt Bay, which include North Spit (active), and four historic gauges located at Mad River Slough, Samoa, Fields Landing, and Hookton Slough. Figure 2-1 shows the Crescent City tide gauge in relation to Humboldt Bay, and Figure 2-11 shows the five Humboldt Bay tide gauge locations.

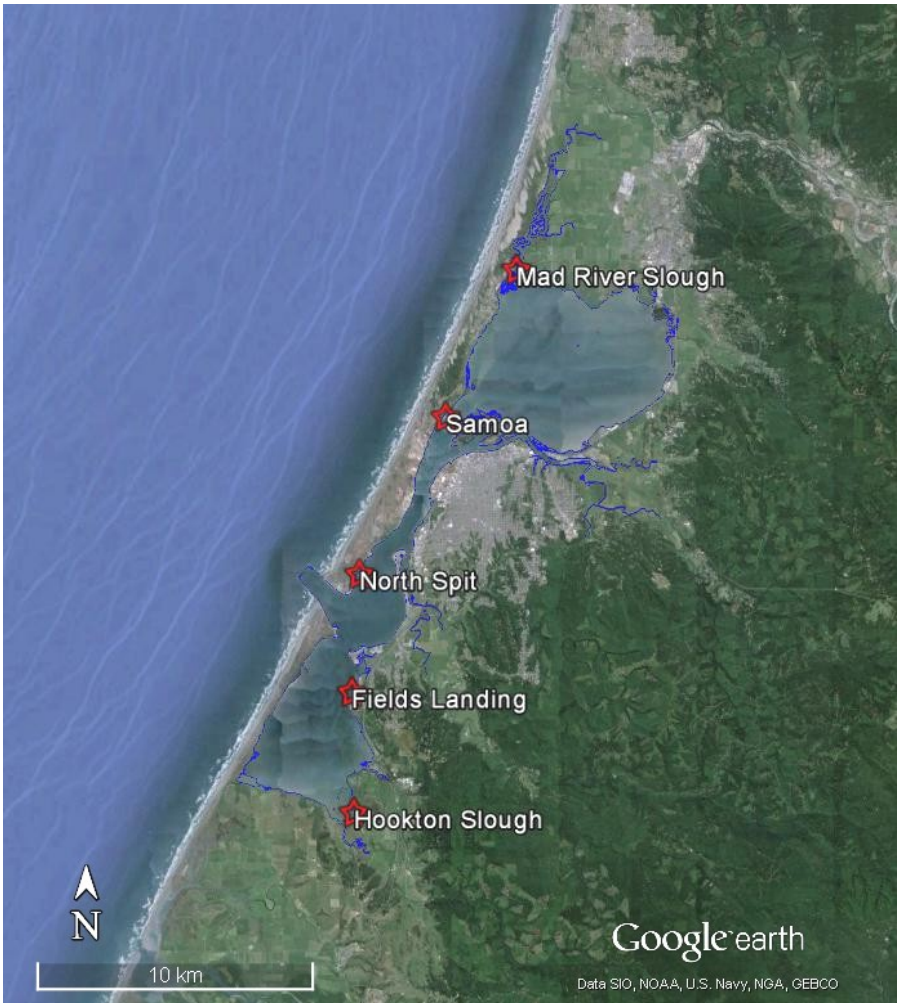

Figure 2-11 Five NOAA tide gauge locations in Humboldt Bay, and mean high water edge (blue line).

The analysis approach relied on the long-term Crescent City tide gauge (~81 years), and the general approach of Mitchell et al. (1994) and Burgette et al. (2009) to determine RSL and VLM rates at the Humboldt Bay tide gauges, which all have records less than 40 years in length and are considered too short to directly determine rates. The analysis approach also relied on the 20th century ReMSL rise rate of 2.28 mm/yr (Burgette et al., 2009) for the PNW. Updated estimates of VLM and RSL rates for the Crescent City and Humboldt Bay tide gauges (Patton et al., 2014) are provided in Table 2-3. For a detailed discussion of the tide gauge analysis methods and interpretation of results, reference can be made to the Patton et al. (2014) work.

Table 2-3 Summary of relative sea level (RSL) rise and vertical land motion (VLM) rates for Crescent City and the five Humboldt Bay tide gauges (Patton et al., 2014). Regional mean sea level (ReMSL) rise is the Burgette et al. (2009) rate of 2.28 mm/yr. Positive rates indicate upward motion, and negative rates indicate downward motion.

	Annual Rates (mm/yr)		
Tide Gauge	**ReMSL**	**VLM**	**RSL**
Crescent City	2.28	3.25	-0.97
North Spit (Humboldt Bay)	2.28	-2.33	4.61
Mad River Slough (Humboldt Bay)	2.28	-1.11	3.39
Samoa (Humboldt Bay)	2.28	-0.25	2.53
Fields Landing (Humboldt Bay)	2.28	-1.48	3.76
Hookton Slough (Humboldt Bay)	2.28	-3.56	5.84

Vertical land motion rates determined from the tide gauge analysis (Table 2-3) generally agreed within 1 mm/yr of the land-level VLM rates derived from the benchmark survey analysis (Patton et al., 2014). The north to south down trending VLM gradient controls the RSL rate variation in Humboldt Bay, with the highest rates of VLM in south Humboldt Bay at the Hookton Slough gauge. Adding the ReMSL of 2.28 mm/yr to the VLM rates in Table 2-3 provide estimates of RSL rise rates for Humboldt Bay. For example, RSL rise rates for Mad River Slough, North Spit, and Hookton Slough are approximately 3.4, 4.6 and 5.8 mm/yr, respectively. The tectonic deformation in Humboldt Bay increases the RSL rates above the ReMSL rate of 2.28 mm/yr, with both the North Spit and Hookton Slough RSL rates being more than twice the regional rate. These higher RSL rise rates indicate that increases in the GMSL and ReMSL will affect Humboldt Bay faster than other parts of U.S. west coast; and within the bay, the south end will be affected sooner than the north end.

Sea Level Rise Trends at the North Spit and Crescent City Tide Gauges

Due to the large monthly MSL oscillations inherent in PNW tide gauges caused by natural climate and ocean variability (e.g. Figure 2-8), researches typically attempt to smooth the monthly MSL data prior to assessing decadal trends. One approach is to remove the average seasonal cycle from the monthly MSL values (e.g. Zervas, 2009). However, Komar et al. (2011) demonstrated that using the average summer monthly MSL (average summer MSL) provided the statistically best RSL trends for PNW tide gauges. The average summer MSL value consists of the three-month average, centered on the unadjusted minimum monthly summer value. Figure 2-12 and Figure 2-13 show the RSL trends for the Crescent City and North Spit tide gauge observation record, respectively, for both smoothing approaches described above.

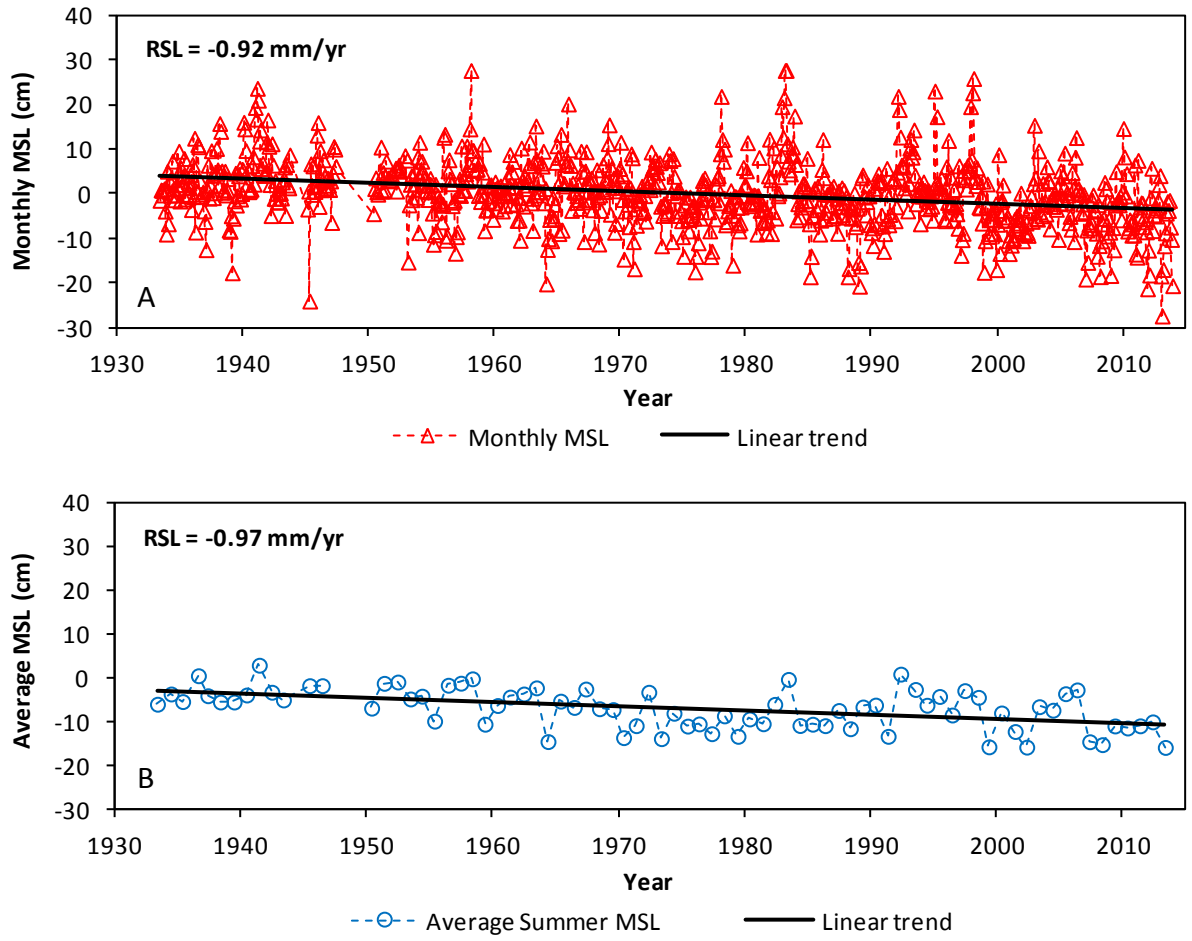

Figure 2-12 Relative sea level (RSL) trends for Crescent City tide gauge using (A) monthly mean sea level (MSL) with the average seasonal cycle removed, and (B) average summer MSL. Figures reproduced from Patton et al. (2014).

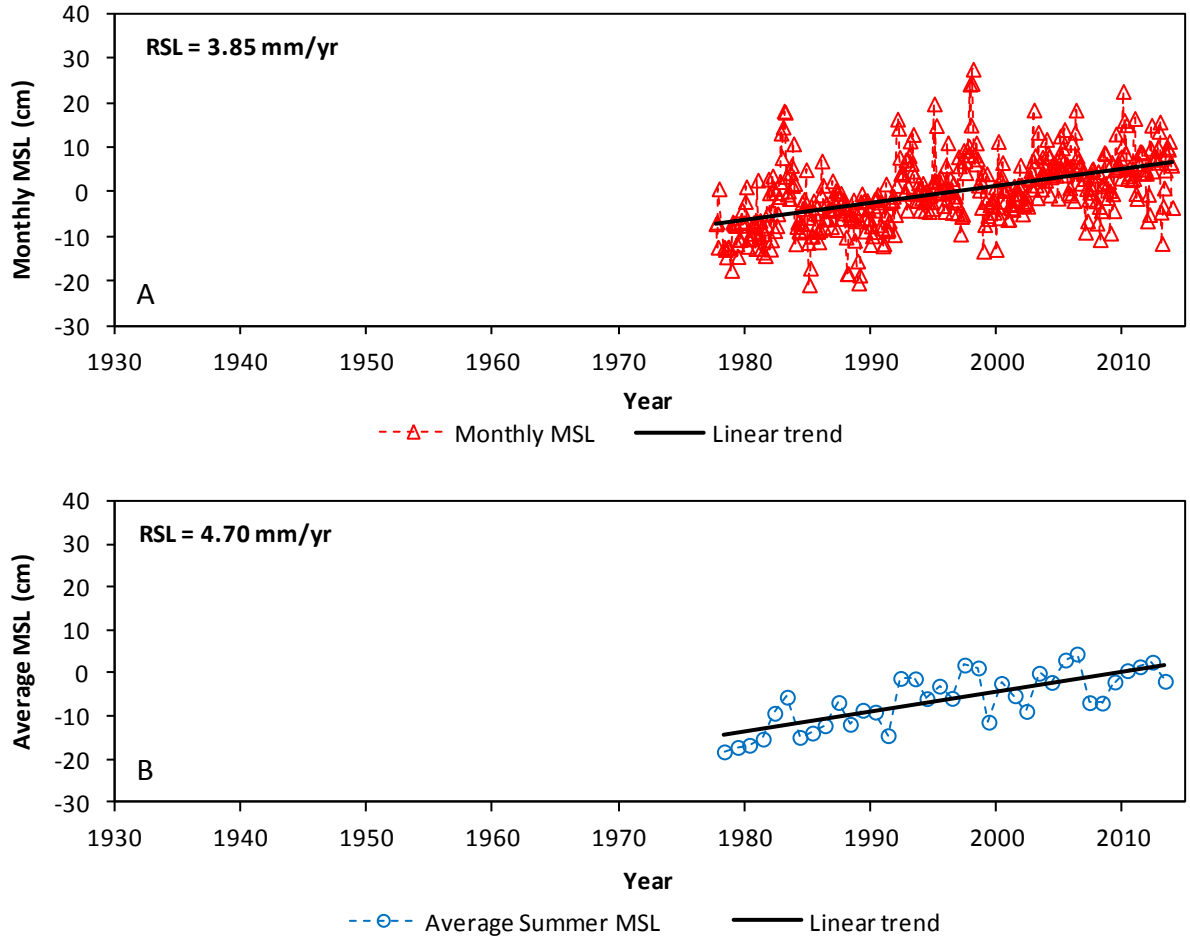

Figure 2-13 Relative sea level (RSL) trends for North Spit tide gauge using (A) monthly mean sea level (MSL) with the average seasonal cycle removed, and (B) average summer MSL. Figures reproduced from Patton et al. (2014).

The figures clearly show that the average summer MSL approach of Komar et al. (2011) significantly reduces scatter compared to the monthly MSL approach, by removing much of the data with extreme seasonal and natural climate variability. The RSL trends for Crescent City is -0.92 mm/yr for the monthly MSL approach, and -0.97 mm/yr for the average summer MSL approach (Figure 2-12). These similar RSL trends can be attributed to the 81-year observation record length for Crescent City. In contrast, the North Spit tide gauge record is relatively short (~37 years), and differences between the RSL trends (3.85 and 4.70 mm/yr) are much larger (Figure 2-13). However, the RSL trend of 4.70 mm/yr for the average summer MSL is close to the RSL value of 4.61 mm/yr (Table 2-3) determined by Patton et al. (2014), demonstrating that the summer MSL approach of Komar et al. (2011) may be best for estimating sea level change trends, even for tide gauges with shorter records.

To provide further insight into decadal trends in sea level rise for the Humboldt Bay region, the estimated VLM rates (Table 2-3) for the Crescent City and North Spit tide gauges were removed from the monthly MSL record, which essentially force both records to the ReMSL rate of 2.28 mm/yr. Figure 2-14 show the average summer MSL series developed from the VLM adjusted records for Crescent City and North Spit, respectively. The average summer MSL values follow the ReMSL trend over the observation record for both tide gauges, although natural climate variability and interannual to multidecadal trends exist in the data scatter. For example, the 1982-83 and 1990s El Niño events (Figure 2-7) generated summer MSL values that were consistently above the ReMSL trend. The average summer MSL values are similar between tide gauges for the period of record overlap (~1977 to 2014), with differences perhaps contributable to the different summer seasonal cycles for Crescent City and North Spit (Figure 2-9).

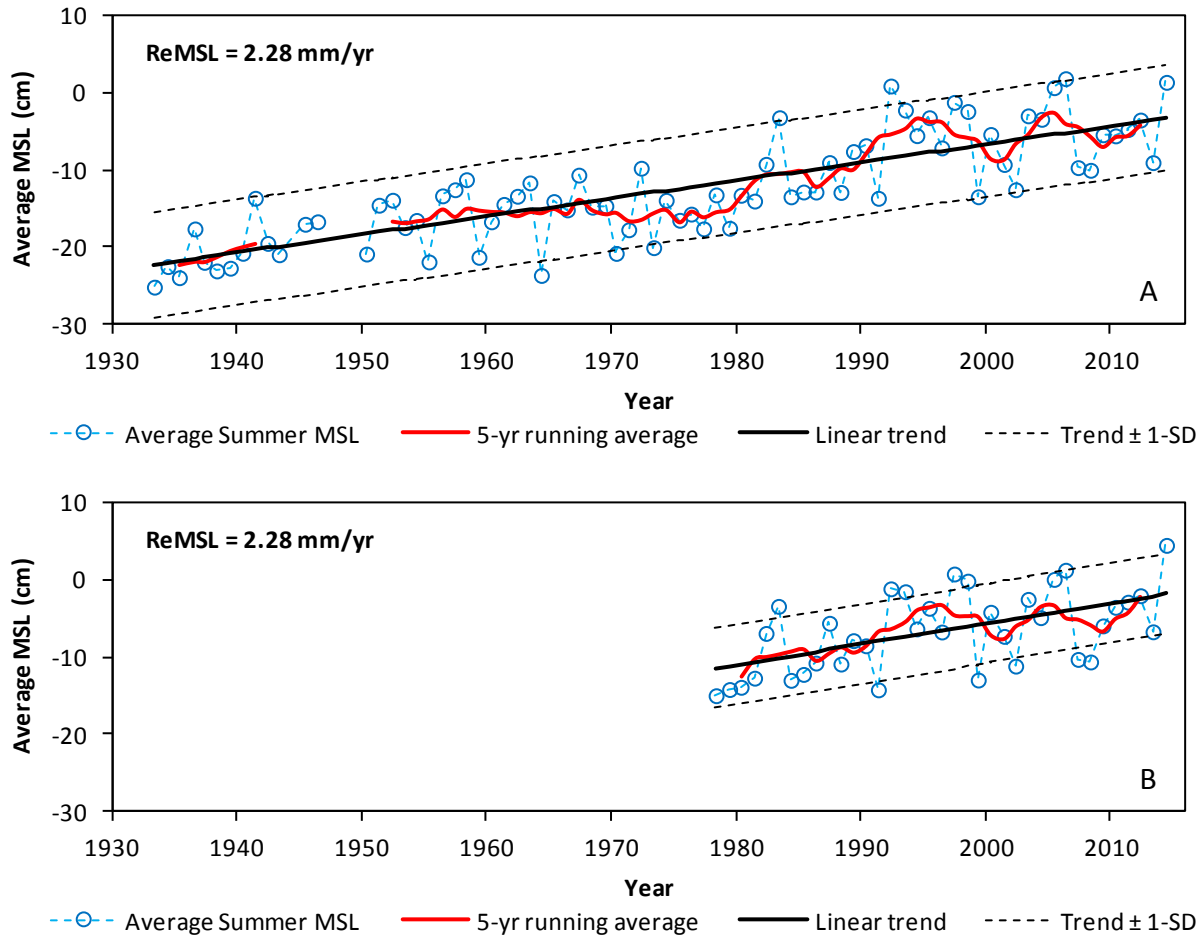

Figure 2-14 Average summer mean sea levels (MSL) for the monthly MSL with the vertical land motion (VLM) removed for (A) Crescent City tide gauge (VLM of 3.25 mm/yr), and (B) North Spit tide gauge (VLM of -2.33 mm/yr). Removal of the VLM forced the sea level trend (black line) to the regional MSL (ReMSL) of 2.28 mm/yr. The black dashed lines are the trend line ± one standard deviation (1-SD), and the red line is the 5-year running average.

The suppression of sea level rise along the U.S. west coast noted by Bromirski et al. (2011) is visible in the average summer MSL series for Crescent City and North Spit tide gauges (Figure 2-14) from about 1990 to the mid-2000s, as evidenced by the downward slope of the 5-yr running average (red line) during this period. Furthermore, the effects of the PDO regimes on the multidecadal sea level variation also described by Bromirski et al. (2011) are apparent in the average summer MSL. For example, the 1960s to 1980 period of consistently low summer MSL values coincides with the 1950 to late 1970s cold phase of the PDO (Figure 2-7). Likewise, the period of high summer MSL values during the late 1980s to 2000 is consistent with late 1970s to late 1990s PDO warm phase.

Although the average summer MSL series for the Crescent City and North Spit tide gauges show interannual to multidecadal variations due to seasonal atmospheric and ocean circulation processes (e.g. upwelling), and natural climate variability (e.g. ENSO and PDO), the extreme high and low values still follow the ReMSL trend over the observation record. This can be clearly seen as all the summer MSL extremes closely track the trend line envelopes (black dashed lines) shown in Figure 2-14, which consist of the ReMSL trend ± one standard deviation of the summer MSL values.

Sea Level Height Variability

Sea level heights vary due to astronomical tides, storm surge, wind stress effects, changes in barometric pressure, seasonal cycles, and ENSO phases, which results in water levels reaching higher levels over longer time scales (Cayan et al., 2008; Knowles, 2010). Figure 2-15 shows the hourly water levels for the Crescent City tide gauge for the 1982-83 El Niño years, along with the MSL and mean higher high water (MHHW) tidal datum, the mean monthly maximum water (MMMW), and the 10- and 100-yr extreme high water level events. As noted by Cayan et al. (2008), this sea level height variability is superimposed on MSL.

Most coastal damage to the U.S. west coast occurs when storm surge and high waves coincide with high astronomical tides and El Niño events (Cayan et al., 2008; NRC, 2012). Extreme sea level heights can occur when these forces coincide, which happened along the U.S. west coast during the large 1982-83 and 1997-98 El Niño events. For example, in late January 1983 a large El Niño driven storm coincided with higher than normal astronomical high tides, and produced the highest water level of record at the Crescent City tide gauge on 29 January 1983 which exceeded the 100-year extreme exceedance probability event (Figure 2-15 and Figure 2-16). The peak hourly water level on 29 January 1983 was 66.2 cm higher than the astronomical high tide, and on 26 January 1983, the peak hourly water level was 84.0 cm above the astronomical high tide.

As GMSL and ReMSL rise increases over time, the sea level height variability described above will also increase, and the incidence of extreme high water levels will become more common (NRC, 2012).

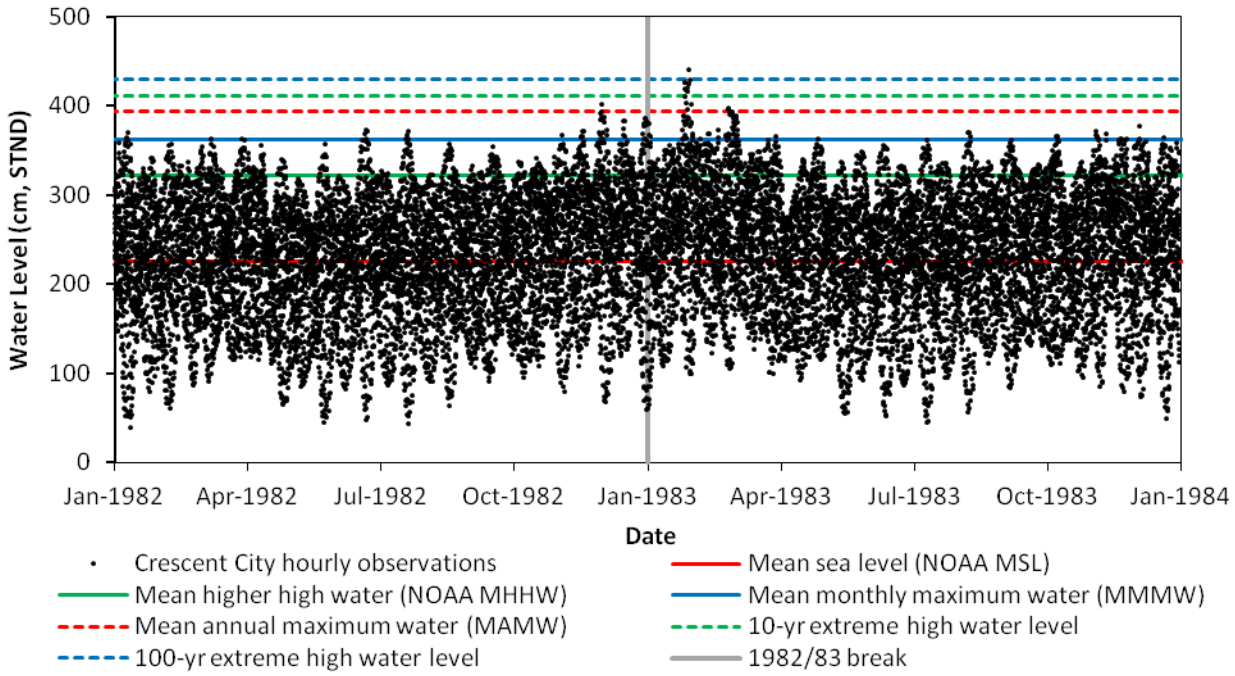

Figure 2-15 Crescent City tide gauge hourly water levels for 1982-83 El Niño years, with mean sea level (MSL), mean higher high water (MHHW), mean monthly maximum water (MMMW), mean annual maximum water (MAMW), and the 10- and 100-yr extreme high water level events.

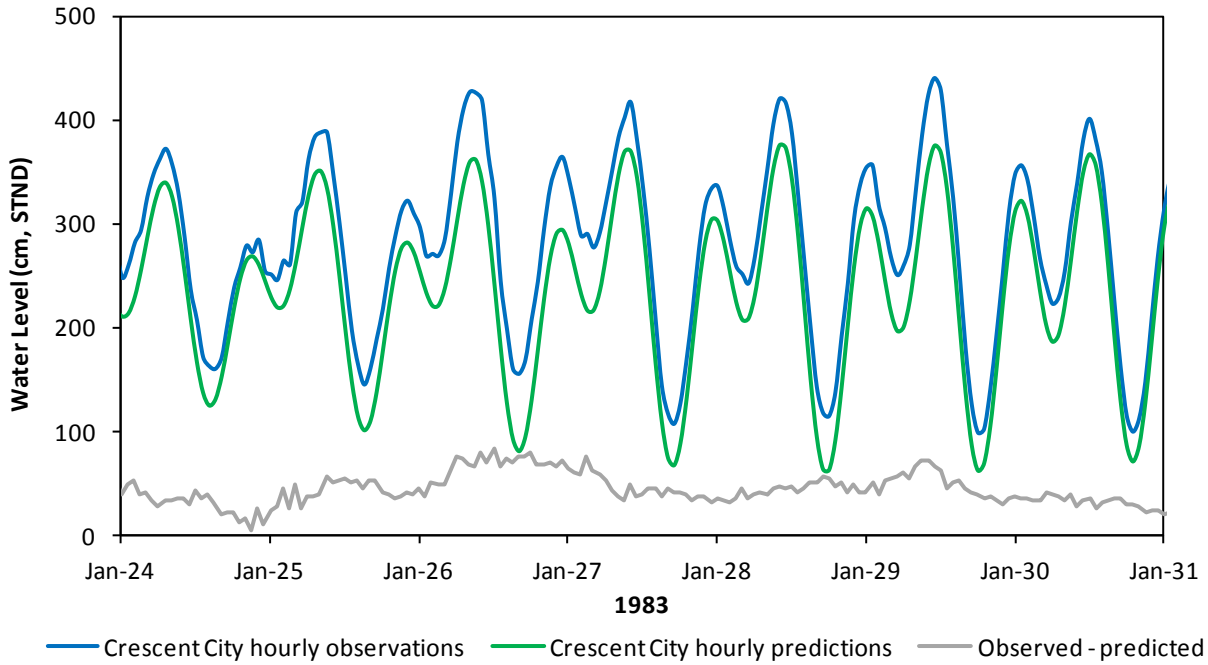

Figure 2-16 Crescent City tide gauge hourly water levels for January 1983 El Niño year. Blue line is observed water level, green line is astronomical tidal prediction, and grey line is observed minus predicted.

Projections of Sea Level Rise

As discussed previously, observations provide unequivocal evidence that the climate system is warming and that GMSL has risen over the 20th century (NRC, 2012; IPCC, 2013b). Projections of future sea level rise, both globally and regionally, are necessary to adequately assess and plan for the effects and impacts to coastal areas from sea level rise. Projections of future sea level rise generally depend on the understanding of contributions to sea level change, the response of key geophysical processes, and assumptions regarding future warming of the climate system (NRC, 2012). This section provides an overview and summarizes recent projections of GMSL rise, estimates of ReMSL rise for the Humboldt Bay region, and adjustments to this regional rate to provide projections of RSL rise for Humboldt Bay.

Methods for Projecting Future Sea Level Rise

Projections of 21st century sea level rise are typically made using process-based or physical models, such as Atmosphere–Ocean General Circulation Models (AOGCMs), extrapolating observations, semi-empirical models, or a combination of these approaches (NRC, 2012; Church et al., 2013). These projections rely on the different processes affecting sea level change described previously, such as ocean thermal expansion or VLM, depending if the projection is for global, regional or relative sea level rise.

Process-based or physical based projections of sea level rise attempt to describe the contributions from the individual physical components that contribute to sea level rise (Church et al., 2013). The AOGCMs predict the response of the climate system and ocean to future scenarios of greenhouse gas emissions. These models can provide reasonable estimates of future sea level rise from ocean volume density change (steric), primarily from thermosteric volume changes due to thermal expansion. However, these models underestimate the ocean volume mass change (barystatic) from melting land ice, as they do not fully account for rapid dynamical changes in the Greenland and Antarctic ice sheets (NRC, 2012; Church et al., 2013). The 2007 IPCC AR4 (Meehl et al., 2007) projections (Figure 2-17) used a combination of AOGCMs to estimate the global ocean steric volume change, and ice sheet surface mass balance and empirical models to determine ocean volume mass change from melting land ice for six different greenhouse gas emission scenarios. As noted in NRC (2012), at the time the AR4 projections were compiled, observations of rapid land ice transfers at a global scale were just beginning, and these projections did not include rapid dynamical ice sheet contributions or provide an upper bound for sea level rise. Consequently, the 2007 IPCC AR4 sea level rise projections were considered too low by the NRC (2012) and other researchers (e.g. Rahmstorf, 2007; Pfeffer et al., 2008; Vermeer and Rahmstorf; 2009; Jevrejeva et al., 2010; Grinsted et al., 2010).

Extrapolation of existing or past sea level rise rates can also be used to project future conditions, assuming constant observed rates or specified rules, and has been used by investigators to project the cryosphere (i.e. glaciers, ice caps, and ice sheets) contribution to projected future sea level rise (NRC, 2012).

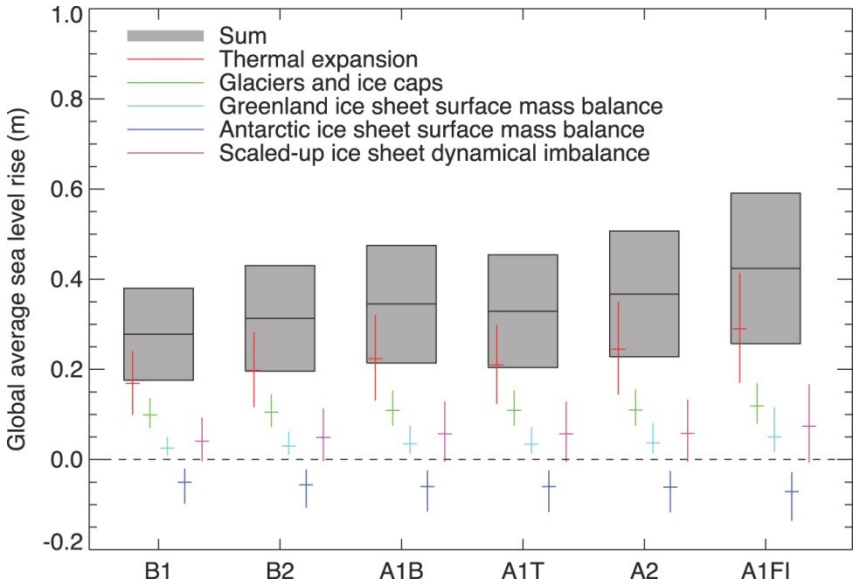

Figure 2-17 Projections and uncertainties (5 to 95% ranges) of global average sea level rise and its components in 2090 to 2099 (relative to 1980 to 1999) for the six emission scenarios. (Figure from Meehl et al. (2007), Figure 10.33)

The motivation for development of semi-empirical models (e.g. Rahmstorf, 2007; Vermeer and Rahmstorf; 2009; Jevrejeva et al., 2010; Grinsted et al., 2010) was primarily due to the limitations described above for the process-based sea level rise projections in the 2007 IPCC AR4 (Meehl et al., 2007; NRC, 2012; Church et al., 2013). The semi-empirical models do not explicitly account for the individual components of sea level rise, but are based on the physical concept that sea level rises as the Earth's climate system gets warmer (NRC, 2012; Church et al., 2013). Semi-empirical models are developed and calibrated to reproduce the observed past sea level record to the temperature record. Consequently, future sea level rise projections assume that the relationship between sea level and temperature change of the past holds in to the future. This relationship may not hold if the nonlinear physical processes, such as rapid dynamical ice sheet contributions, do not scale to the calibration period of the past (NRC, 2012; Church et al., 2013). Semi-empirical projections of sea level rise are generally two or more times greater than the process-based projections in the 2007 IPCC AR4 (NRC, 2012). As noted in the 2013 IPCC AR5, despite the success of semi-empirical models to reproduce the sea level rise observed in the 20th century, consensus in the scientific community does not exist regarding their reliability and confidence is low in their projections (Church et al., 2013).

Since completion of the 2007 IPCC AR4, a number of 21st century GMSL rise projections have been developed using modifications to the AR4 process-based estimates or semi-empirical models driven by the AR4 emission scenarios (Figure 2-18). This figure also includes the 2013 IPCC AR5 process-based projections (Church et al., 2013) for the new AR5 emission scenarios. Both the process-based estimates that include the extrapolated cryosphere rates and the semi-empirical models generate higher GMSL rise projections for the same AR4 emission scenarios

compared to the process-based models. The highest projected range of GMSL rise is derived from a combination of ocean thermal expansion from the 2007 IPCC AR4 and extrapolations of possible glacier and ice sheet loss by year 2100 (Pfeffer et al., 2008). They concluded that a total GMSL rise of 200 cm by 2100 is possible, but requires glacier variables to quickly accelerate to extremely high limits. However, the NRC (2012) concluded that this future scenario is highly unlikely and probably not plausible. Pfeffer et al. (2008) also concluded that a GMSL rise greater than 200 cm by 2100 is physically untenable.

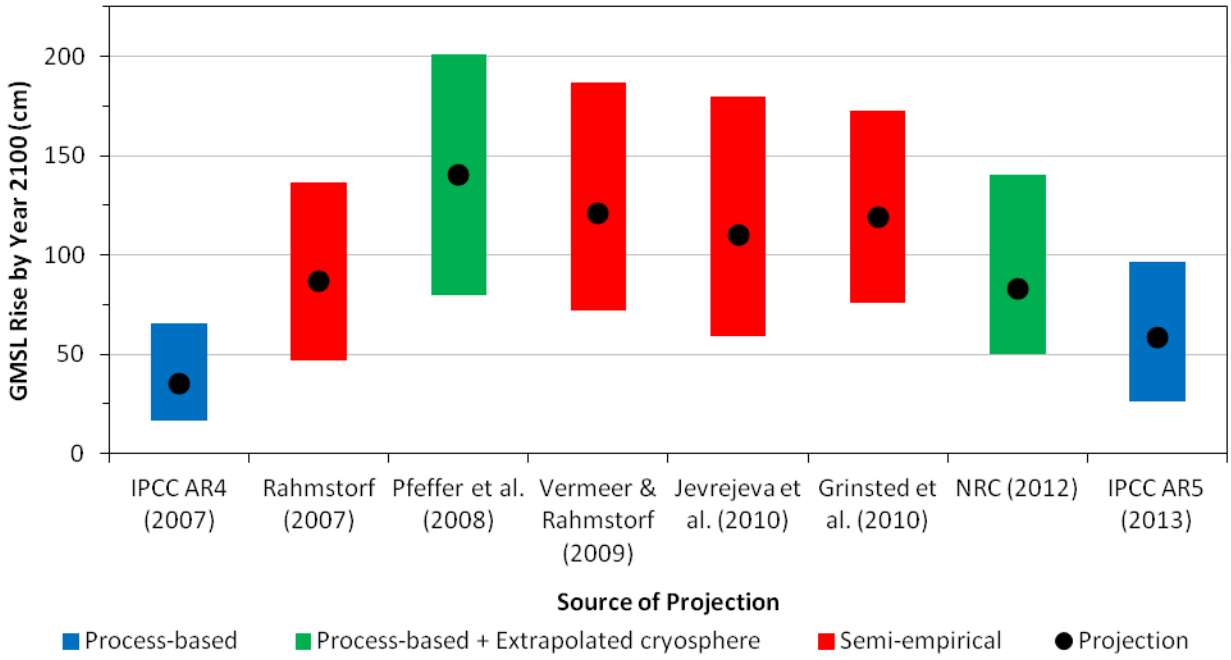

Figure 2-18 Global mean sea level (GMSL) rise projections for year 2100 from scientific literature since the 2007 IPCC AR4. Projections sequentially plotted by year of estimate. Range is the low and high uncertainties (generally 5 to 95% range), and the projection is the projected estimate for the A1B emission scenario from the 2007 IPCC AR4, or the median value of the range. Process-based projections are blue bars, process-based plus extrapolated cryosphere projections are green bars, and semi-empirical projections are red bars. Also provided are the process-based 2013 IPCC AR5 projections for the AR5 emission scenarios.

Global Mean Sea Level Rise Projections and Scenarios

This section provides a brief overview of the most recent 21st century projections and scenarios of GMSL rise published since 2012.

NOAA (2012) Global Mean Sea Level Rise Scenarios

In 2012, NOAA recommended a set of sea level rise scenarios for the United States National Climate Assessment (Parris et al., 2012). Unlike projections of sea level rise, the scenarios do

not attempt to predict future conditions, but describe potential future conditions that support sea level rise vulnerability assessments, planning and decision making under uncertainty. Four scenarios were developed based on a synthesis of future estimates of GMSL rise by 2100 from the scientific literature, consistent with Figure 2-18, that reflect different degrees of ocean warming and melting land ice (Table 2-4).

Table 2-4 NOAA (2012) global mean sea level (GMSL) rise scenarios by year 2100 (Parris et al., 2012).

Scenario	GMSL rise by year 2100 (cm)	
	Relative to year 1992[1]	Relative to year 2000[2]
Highest	200	197
Intermediate-High	120	117
Intermediate-Low	50	47
Lowest	20	17

[1]As reported by Parris et al. (2012). [2]Made relative to year 2000 by applying 1993-2010 satellite altimetry GMSL rate of 3.2 mm/yr (Table 2-1) for 8 years.

The Highest Scenario of GMSL rise was based on the Pfeffer et al. (2008) estimate of maximum possible glacier and ice sheet loss by 2100, and should be used when there is little tolerance for risk. The Intermediate-High Scenario was based on the average of the upper end of semi-empirical model projections, and the Intermediate-Low Scenario was based on the upper end of the 2007 IPCC AR4 projections. The Lowest Scenario was based on a linear extrapolation of the 20th century GMSL rate of ~1.7 mm/yr. Given the range of GMSL rise projections used in developing the scenarios, the authors concluded that they have very high confidence (>9 in 10 chance) that GMSL will rise at least 20 cm and no more than 200 cm by 2100 (Parris et al., 2012).

National Research Council (2012) Global Mean Sea Level Rise Projections

California Executive Order S-13-08, issued by Governor Schwarzenegger in 2008, directed State agencies to plan for sea level rise and coastal impacts, and it also requested the National Research Council (NRC) to assess sea level rise along the coasts of California, Oregon and Washington. The final NRC report, Sea-Level Rise for the Coasts of California, Oregon, and Washington, was released in June 2012, and provides the most comprehensive assessment of future sea level rise rates for the U.S. west coast conducted to date. Projections of sea level rise for California, Oregon and Washington were provided for the years 2030, 2050 and 2100. The Coastal and Ocean Working Group of the California Climate Action Team (CO-CAT) Sea Level Rise Guidance Document (March 2013), and the California Coastal Commission Draft Sea Level

Rise Policy Guidance (October 2013) have been updated with the scientific findings of the NRC (2012) report for California.

The NRC (2012) GMSL rise projections (Table 2-5) consisted of the ocean volume density change (steric) component predicted from the AOGCMs in the 2007 IPCC AR4 for the A1B emission scenario, and an extrapolated land ice (cryosphere) component using the best available information for glaciers, ice caps, and ice sheets. The NRC projections did not include reservoir storage and groundwater extraction as recent estimates suggested that these components summed to near zero. The NRC (2012) GMSL rise projection for 2100 (Figure 2-18) is generally lower than the semi-empirical estimates and higher than the process-based projections. Also provided in Table 2-5 for comparison is the 2013 IPCC AR5 (Church et al., 2013) GMSL rise projection for the A1B emission scenario from the 2007 AR4.

Table 2-5 Summary of global mean sea level (GMSL) rise projections (in cm) from NRC (2012) and 2013 IPCC AR5 (Church et al., 2013) relative to year 2000. The AR5 projection is for the A1B emission scenario from the 2007 IPCC AR4. Data from Table 5.2 of NRC (2012); and Table 13.5 of Church et al. (2013) and data downloaded from https://www.ipcc.ch/report/ar5.

	NRC (2012) projection		2013 IPCC AR5 projection for A1B emission scenario from 2007 AR4[1]	
Year	Projection	Range	Projection	Range
2030	13.5 ± 1.8	8.3 - 23.2	11.0	7.5 – 14.4
2050	28.0 ± 3.2	17.6 - 48.2	21.9	15.6 – 28.6
2100	82.7 ± 10.6	50.4 - 140.2	58.4	40.4 – 78.4

[1]Projections for years 2030 and 2050 calculated from downloaded data and based on 20-year centered average (Church et al., 2013). AR5 projections are relative to 1986-2005, projections made relative to year 2000 by applying 1993-2010 satellite altimetry GMSL rate of 3.2 mm/yr (Table 2-1) for 5 years.

IPCC Fifth Assessment Report (2013) Global Mean Sea Level Rise Projections

In 2013, the IPCC released its Fifth Assessment Report (AR5) on climate change. As part of the 2013 scientific work supporting the AR5, new GMSL rise projections were developed for four new greenhouse gas emission scenarios (Church et al., 2013). The new scenarios, the Representative Concentration Pathways (RCPs), represent future emissions and concentrations of greenhouse gases, aerosols, and other climate drivers. The RCPs represent a set of mitigation scenarios, which include implied policy actions, that have different targets in terms of greenhouse gas emissions and radiative forcing at year 2100 (IPCC, 2013b). RCP2.6 represents an emission mitigation scenario leading to very low radiative forcing (2.6 W/m^2), RCP4.5 and RCP6.0 represent two stabilization scenarios with intermediate radiative forcing (4.5 and 6.5 W/m^2, respectively), and RCP8.5 represents a very high greenhouse gas emission scenario with high radiative forcing (8.5 W/m^2).

Church et al. (2013) noted that confidence in projections of future GMSL rise has increased since the 2007 IPCC AR4, due to the improved understanding of the components driving sea level change, the ability to reproduce observed GMSL change since 1993 from the observed budget (Table 2-2 and Figure 2-5), the improved ability of process-based models to reproduce observations, and the inclusion of ice sheet dynamical changes. Summing the components of ocean thermal expansion predicted by the AOGCMs, glacier mass loss predicted by the global glacier models with AOGCM input, and land water storage accounts for about 65% of the observed GMSL rise for 1901 to 1990 (Church et al., 2013). For the 1993 to 2010 period, the sum of the modeled components accounts for approximately 90% of the observed satellite altimetry rate of 3.2 mm/yr, and is consistent with the 2.8 mm/yr rate for the tide gage reconstruction (Table 2-2). The difference between the observed and total modeled GMSL rise can be attributed to melting ice sheets, and inclusion of the observed Greenland and Antarctica ice sheet contribution (Table 2-2) further improves the agreement with the 3.2 mm/yr altimetry rate (Church et al., 2013). This improved agreement between observations and process-based models provides confidence in the AR5 projections of 21st century GMSL rise.

The 2013 IPCC AR5 (Church et al., 2013) projections for 21st century GMSL rise are presented in Table 2-6 and Figure 2-19. The AR5 projections were presented for the periods of 2046 to 2065, 2081 to 2100, and year 2100 relative to the 1986 to 2005 period. To allow comparison with the NRC (2012) projections, estimates for the years 2030 and 2050 were developed using available data downloaded from the IPCC AR5. Table 2-7 compares the estimated AR5 median projection and range to the NRC (2012) projections.

The 2013 IPCC AR5 projections of GMSL rise by 2100 (Figure 2-18) is lower than the semi-empirical estimates and the NRC (2012) estimates, but higher than the 2007 IPCC AR4 projection. The larger AR5 projections compared to AR4 are primarily due to improved modeling of the land ice contributions (Church et al., 2013).

Table 2-6 Summary of median values and likely ranges of global mean sea level (GMSL) rise projections (in cm) from 2013 IPCC AR5 for the four RCP emission scenarios (Church et al., 2013) relative to year 2000[1]. Data from Table 13.5 and data downloaded from https://www.ipcc.ch/report/ar5.

Year	RCP2.6	RCP4.5	RCP6.0	RCP8.5
2030	11.3 [7.7 to 14.9]	11.3 [7.9 to 14.7]	10.9 [7.4 to 14.3]	12.0 [8.5 to 15.5]
2050	20.4 [14.1 to 26.9]	21.5 [15.3 to 28.0]	20.4 [14.3 to 26.8]	24.3 [17.6 to 31.3]
2100	42.4 [26.4 to 59.4]	51.4 [34.4 to 69.4]	53.4 [36.4 to 71.4]	72.4 [50.4 to 96.4]

[1]Projections for years 2030 and 2050 calculated from downloaded data and based on 20-year centered average (Church et al., 2013). AR5 projections are relative to 1986-2005, projections made relative to year 2000 by applying 1993-2010 satellite altimetry GMSL rate of 3.2 mm/yr (Table 2-1) for 5 years.

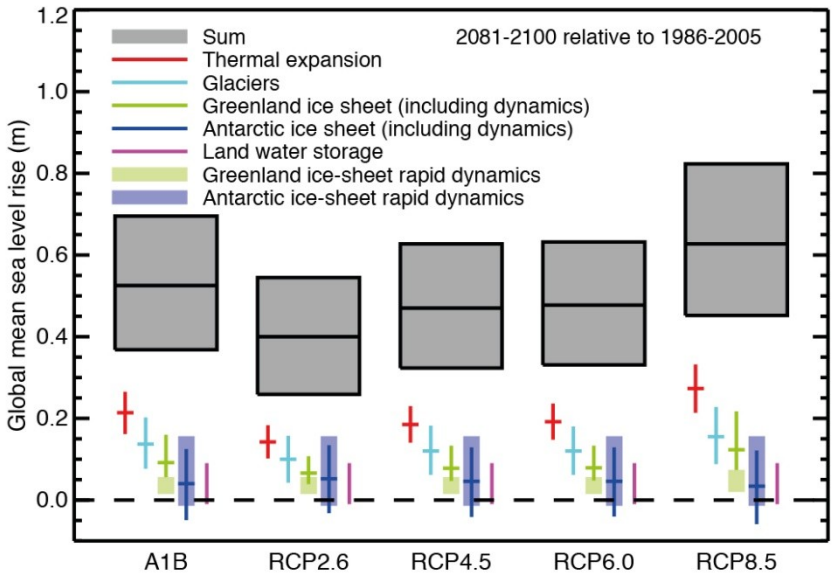

Figure 2-19 Projections from process-based models with likely ranges and median values for global mean sea level (GMSL) rise and its contributions in 2081–2100 relative to 1986–2005 for the four RCP scenarios and scenario SRES A1B used in the AR4. The contributions from ice sheets include the contributions from ice-sheet rapid dynamical change, which are also shown separately. (Figure from Church et al. (2013), Figure 13.10)

Table 2-7 Summary of global mean sea level (GMSL) rise projections (in cm) from NRC (2012) and 2013 IPCC AR5 (Church et al., 2013) relative to year 2000. Data compiled from Table 2-5 and Table 2-6.

	NRC (2012) projection		2013 IPCC AR5 projection[1]	
Year	Projection	Range	Median Projection	Range
2030	13.5 ± 1.8	8.3 - 23.2	11.3	7.4 – 15.5
2050	28.0 ± 3.2	17.6 - 48.2	21.0	14.1 – 31.3
2100	82.7 ± 10.6	50.4 - 140.2	52.4	26.4 – 96.4

[1]Projection is median value of the RCP median projections, and range is the lowest and highest range value for each year from Table 2-6.

Given the higher confidence in the AR5 projections, the authors concluded that for each RCP emission scenario the 21st century GMSL rise is likely (66 to 100% probability) to be within the range given by the process-based models (Church et al., 2013). The authors further concluded that the only process that could substantially increase GMSL rise above the likely range during the 21st century is the collapse of the marine-based sectors of the Antarctic ice sheet. Although

the contribution to GMSL rise from a collapse of the Antarctic ice sheet cannot currently be quantified, due to a lack of consensus in the scientific literature, there is medium confidence that if a collapse were initiated it would not exceed several tenths of a meter during the 21st century (Church et al., 2013).

It is worth noting that a 30 cm (0.3 m) increase in GMSL rise from the collapse of the Antarctic ice sheet would essentially make the 2013 IPCC AR5 projections consistent with the NRC (2012) projections by 2100 (Table 2-7). For example, the AR5 projected median value would increase from 52.4 to 82.4 cm, which is essentially the same as the NRC projection value of 82.7 cm. Likewise, the AR5 high range projection would increase 96.4 to 126.4 cm, close to the 140.2 cm NRC high range value.

Regional Sea Level Rise Projections for the Humboldt Bay Region

The NRC (2012) report provided sea level rise projections for California, Oregon and Washington that varied from the GMSL rise projections due to ocean dynamical processes, steric density variations, sea level fingerprint effects of the mass redistribution of melting land ice, and VLM. The NRC determined sea level rise projections for four regions of the U.S. west coast (Seattle, Newport, San Francisco, and Los Angeles) based on the influence of these regional processes, and represent the most comprehensive regional projections to date.

To provide estimates of ReMSL rise projections for the Humboldt Bay region, which is defined in this report to not include VLM effects, the NRC (2012) regional projections were modified to remove their VLM component. For example, north of Cape Mendocino, the NRC assumed that all areas had an upward VLM of 1 mm/yr, which is inconsistent with the observed downward VLM in Humboldt Bay (Table 2-3). Modifications consisted of removing the NRC estimates of VLM for Newport (1 mm/yr, upward VLM) and San Francisco (-1.5 mm/yr, downward VLM), and then averaging the resulting values to provide a ReMSL rise projection for the Humboldt Bay region (Table 2-8).

Table 2-8 Regional mean sea level (ReMSL) rise projections (in cm) for the Humboldt Bay region, and for comparison the NRC (2012) global mean sea level (GMSL) rise projection.

Year	ReMSL rise projection for the Humboldt Bay region[1]		NRC (2012) GMSL rise projection	Projection percent difference[2]
	Projection	Range		
2030	9.9	3.9 – 21.3	13.5	-27.0
2050	21.4	10.9 – 46.2	28.0	-23.8
2100	75.1	38.6 – 137.9	82.7	-9.2

[1]ReMSL projection is the averaged NRC (2012) projections for Newport and San Francisco with the vertical land motion removed. [2]Percent differences are relative to the GMSL rise projection.

The modified ReMSL rise projection for the Humboldt Bay region differ from the NRC (2012) GMSL rise projection due to the effects of regional dynamical ocean and steric volume change, and the mass volume redistribution of the melting land ice due to the sea level fingerprints. These combined processes lower the ReMSL rise projection for the Humboldt Bay region compared to the GMSL projection (Table 2-8), primarily due to the sea level fingerprint effects (NRC, 2012). The percent differences are greatest for the 2030 (~27%) and 2050 (~24%) projections, with the ReMSL projection being approximately 9% less by 2100.

The 2013 IPCC AR5 (Church et al., 2013) also provided regional projections of sea level rise for the RCP scenarios for the 2081 to 2100 period that included the effects of regional dynamical ocean and steric volume changes, ice sheet mass redistribution, and atmospheric loading. Although not as detailed and at a coarser resolution than the NRC (2012) regional projections, the AR5 projections also indicate that sea level rise for the Humboldt Bay region will be lower than the GMSL rise projection. The percent differences ranged from 0 to ~11% less than the GMSL rise projection for the 2081 to 2100 period relative to 1986 to 2005, with higher differences for the higher RCP scenarios.

Relative Sea Level Rise Projections for the Humboldt Bay Region

The relative sea level (RSL) rise is what coastal areas experience and is the most important quantity for assessing and planning for the coastal impacts from sea level change (NRC, 2012; Church et al., 2013). The modified ReMSL rise projections for the Humboldt Bay region (Table 2-8) can be made to RSL rise projections for Humboldt Bay by simply adding the VLM estimates for the bay (Table 2-3) to the ReMSL values. Table 2-9 lists the RSL rise projections adjusted for the North Spit (-2.33 mm/yr), Mad River Slough (-1.11 mm/yr), and Hookton Slough (-3.56 mm/yr) downward VLMs. Figure 2-20 shows a temporal plot of how the North Spit VLM rate of -2.33 mm/yr combines with the ReMSL rise projection (fit to a second order equation) to provide the RSL rise projection for North Spit.

Table 2-9 Relative sea level (RSL) rise projections (in cm) in Humboldt Bay adjusted for North Spit, Mad River Slough, and Hookton Slough downward vertical land motions (VLM).

	North Spit (VLM = -2.33 mm/yr)		Mad River Slough (VLM = -1.11 mm/yr)		Hookton Slough (VLM = -3.56 mm/yr)	
Year	Projection	Range	Projection	Range	Projection	Range
2030	16.9	12.5 – 27.4	13.3	8.9 – 23.8	20.6	16.2 – 31.1
2050	33.0	21.6 – 58.3	26.9	15.5 – 52.2	39.1	27.7 – 64.4
2100	98.4	61.5 – 161.2	86.2	49.3 – 149.0	110.7	73.8 – 173.5

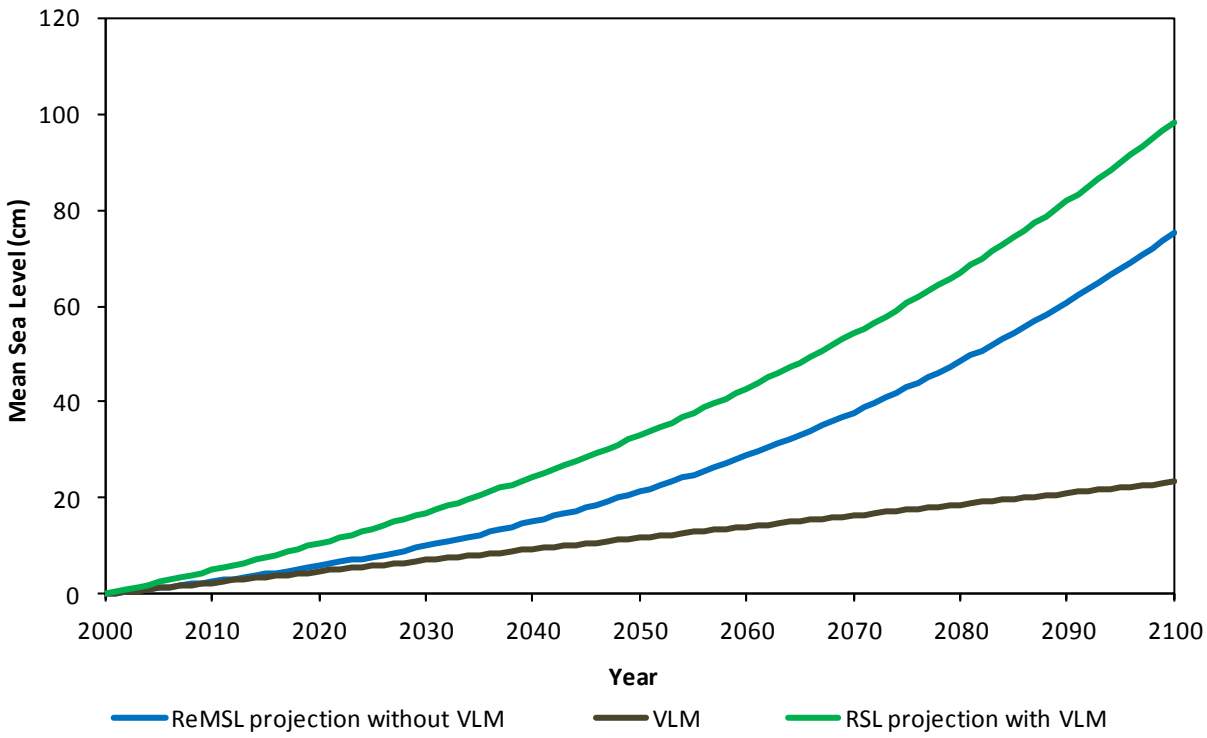

Figure 2-20 Humboldt Bay regional mean sea level (ReMSL) rise projection (based on modified NRC (2012) projections) with vertical land motion (VLM) removed, VLM for North Spit (-2.33 mm/yr, downward motion), and relative sea level (RSL) rise projection for North Spit.

The observed north to south downward VLM gradient in Humboldt Bay (Table 2-3) produces a gradient in the RSL rise projections (Table 2-9), with the south end of the bay having higher RSL projections than the north end. The VLM rates in Humboldt Bay not only create the highest observed RSL rise rates in California, but over the long-term also generate higher RSL rise projections that will affect Humboldt Bay faster than other parts of the U.S. west coast. For example, the large downward VLM for Hookton Slough creates a high RSL rise projection of approximately 174 cm by 2100, which is only 26 cm less than the highest projected GMSL rise of 200 cm due to the maximum possible glacier and ice sheet loss postulated by Pfeffer et al. (2008).

3 Hydrodynamic Model Methods and Configuration

The hydrodynamic model used for the Humboldt Bay SLR modeling is the Environmental Fluid Dynamics Code (EFDC) model originally developed at the Virginia Institute of Marine Science by Dr. John Hamrick (Hamrick, 1992). Tetra Tech, Inc. continued development of EFDC with support from the U.S. Environmental Protection Agency (EPA). In 2007, the EPA released a public domain version of EFDC, EFDC-EPA Version 1.01 (EFDC_EPA), which is part of a suite of models recommended by the EPA for total maximum daily load (TMDL) development. EFDC_EPA is a multifunctional surface water modeling system for simulating three-dimensional (3D) or two-dimensional (2D) flow, transport and biogeochemical processes in surface waters including rivers, lakes, wetlands, estuaries and coastal regions. The EFDC model dynamically couples hydrodynamics and salinity and temperature transport, and can internally link to cohesive and non-cohesive sediment transport, water and sediment toxic contaminant transport and fate, dye transport, and water quality and eutrophication sub-models. Various enhancements to the EFDC hydrodynamic code include hydraulic structure representation, vegetation resistance (Moustafa and Hamrick, 2000), and wetting and drying (Ji et al., 2001). Full documentation of the EFDC model can be found in Hamrick (1992) and Tetra Tech (2007a, 2007b and 2007c).

Dynamic Solutions-International, LLC (DSI) has made a number of enhancements to the EFDC_EPA code, and has its own open source version of EFDC (EFDC_DSI). The primary enhancements of EFDC_DSI include (1) dynamic memory allocation, (2) enhanced heat exchange modeling options, (3) Lagrangian particle tracking sub-model, (4) internal wind wave generation sub-model, and (5) the development of a multi-threaded version of EFDC (EFDC_DSI_OMP) that significantly decreases computational time. DSI has also developed a windows-based GUI (EFDC_Explorer7.1) for pre- and post-processing of the various EFDC models (Craig, 2013). Both EFDC_Explorer7.1 and EFDC_DSI_OMP were used in this study.

Model Formulation

The governing hydrodynamic equations in EFDC are the three-dimensional turbulence- or Reynolds-averaged equations of motion for an incompressible, variable density fluid (Hamrick, 1992). EFDC assumes (Jin, 2000; Ji, 2008): (1) the Boussinesq approximation is appropriate, (2) the hydrostatic pressure assumption describes the vertical pressure distribution, and (3) eddy viscosity concept adequately describes turbulent mixing. To account for realistic boundaries, the hydrodynamic equations are formulated in curvilinear-orthogonal horizontal coordinates and a sigma or stretched vertical coordinate. The transformed hydrodynamic equations for continuity and momentum, and the salinity and temperature transport equations are (Hamrick, 1992; Ji, 2008):

$$\frac{\partial(m\varsigma)}{\partial t}+\frac{\partial(m_y Hu)}{\partial x}+\frac{\partial(m_x Hv)}{\partial y}+\frac{\partial(mw)}{\partial z}=Q_H \qquad (1)$$

$$\frac{\partial(mHu)}{\partial t}+\frac{\partial(m_yHuu)}{\partial x}+\frac{\partial(m_xHvu)}{\partial y}+\frac{\partial(mwu)}{\partial z}-\left(mf+v\frac{\partial m_y}{\partial x}-u\frac{\partial m_x}{\partial y}\right)Hv \tag{2}$$

$$=-m_yH\frac{\partial(p+g\varsigma)}{\partial x}-m_y\left(\frac{\partial h}{\partial x}-z\frac{\partial H}{\partial x}\right)\frac{\partial p}{\partial z}+\frac{\partial}{\partial z}\left(m\frac{A_v}{H}\frac{\partial u}{\partial z}\right)+Q_u$$

$$\frac{\partial(mHv)}{\partial t}+\frac{\partial(m_yHuv)}{\partial x}+\frac{\partial(m_xHvv)}{\partial y}+\frac{\partial(mwv)}{\partial z}+\left(mf+v\frac{\partial m_y}{\partial x}-u\frac{\partial m_x}{\partial y}\right)Hu \tag{3}$$

$$=-m_xH\frac{\partial(p+g\varsigma)}{\partial y}-m_x\left(\frac{\partial h}{\partial y}-z\frac{\partial H}{\partial y}\right)\frac{\partial p}{\partial z}+\frac{\partial}{\partial z}\left(m\frac{A_v}{H}\frac{\partial v}{\partial z}\right)+Q_v$$

$$\frac{\partial p}{\partial z}=-gH\frac{(\rho-\rho_0)}{\rho_0}=-gHb \tag{4}$$

$$\rho=\rho(S,T) \tag{5}$$

$$(\tau_{xz},\tau_{yz})=\frac{A_v}{H}\frac{\partial}{\partial z}(u,v) \tag{6}$$

And for salinity and temperature transport

$$\frac{\partial(mHS)}{\partial t}+\frac{\partial(m_yHuS)}{\partial x}+\frac{\partial(m_xHvS)}{\partial y}+\frac{\partial(mwS)}{\partial z}=\frac{\partial}{\partial z}\left(\frac{mA_b}{H}\frac{\partial S}{\partial z}\right)+Q_S \tag{7}$$

$$\frac{\partial(mHT)}{\partial t}+\frac{\partial(m_yHuT)}{\partial x}+\frac{\partial(m_xHvT)}{\partial y}+\frac{\partial(mwT)}{\partial z}=\frac{\partial}{\partial z}\left(\frac{mA_b}{H}\frac{\partial T}{\partial z}\right)+HR_T+Q_T \tag{8}$$

where t is time, u and v are horizontal velocities in curvilinear-orthogonal horizontal coordinates (x, y), m_x and m_y are the curvilinear-orthogonal coordinate system metric coefficients and are the square roots of the diagonal components of the metric tensor, and $m = m_xm_y$ is the Jacobian or square root of the metric tensor determinate. The sigma coordinate (z) uses a time variable mapping or stretching transformation to provide uniform resolution in the vertical given by:

$$z=\frac{(z^*+h)}{(\zeta+h)} \tag{9}$$

where z^* is the original physical vertical coordinate, and $-h$ and ζ are the physical vertical coordinates of the bottom topography and free surface, respectively. Total depth ($H = h + \zeta$) is the sum of the depth below and the free surface displacement relative to the undisturbed, physical vertical coordinate, $z^* = 0$. The vertical velocity (w) in the sigma coordinate is related to the physical vertical velocity w^* by:

$$w = w^* - z\left(\frac{\partial \varsigma}{\partial t} + \frac{u}{m_x}\frac{\partial \varsigma}{\partial x} + \frac{v}{m_y}\frac{\partial \varsigma}{\partial y}\right) + (1-z)\left(\frac{u}{m_x}\frac{\partial h}{\partial x} + \frac{v}{m_y}\frac{\partial h}{\partial y}\right) \tag{10}$$

In the continuity equation (1), Q_h represents water gains or losses, such as rainfall, evaporation, groundwater interaction and water withdrawals. In the momentum equations (Eq. 2 and 3), g is gravitational acceleration, f is the Coriolis parameter, A_v is vertical turbulent momentum mixing coefficient or eddy viscosity, and Q_u and Q_v are additional forces or momentum sources/sinks such as subgrid scale horizontal diffusion and vegetation resistance. The physical pressure (p) in excess of the reference density hydrostatic pressure is given by:

$$p = \frac{\rho_0 g H(1-z)}{\rho_0} = gH(1-z) \tag{11}$$

where ρ_0 is the reference density. Buoyancy (b) in equation (4) is the normalized deviation of density from the reference value, water density (ρ) is a function of temperature (T) and salinity (S) in equation (5), and τ_{xz} and τ_{yz} are vertical shear stresses in the horizontal (x,y) direction in equation (6). In the transport equation for salinity (7) and temperature (8), A_b is the vertical turbulent mass diffusivity, Q_S and Q_T include subgrid scale horizontal diffusion and constituent sources and sinks, and R_T in the temperature equation represents heating from solar radiation.

Solution of the momentum equations (2 and 3) and transport equations (7 and 8) requires specification of the vertical turbulent viscosity (A_v) and mass diffusivity (A_b). The second moment turbulence closure model developed by Mellor and Yamada (1982) and modified by Galperin et al. (1988) and Blumberg et al. (1992) is used in EFDC to provide the A_v and A_b coefficients. The model relates A_v and A_b to vertical turbulence intensity and turbulence length scale via transport equations (Hamrick, 1992; Ji, 2008).

In EFDC, additional horizontal viscosity or diffusivity, respectively, in the momentum equations (2 and 3) and transport equations (7 and 8) can be calculated using the Smogorinsky subgrid scale formula (Smogorinsky, 1963), which relates horizontal mixing to the model grid size and current shear (Ji, 2008).

Vertical Boundary Conditions

Vertical boundary conditions for the momentum equations are based on specifying the kinematic shear stresses in equation (6) at the bed ($z = 0$) and water surface ($z = 1$) as (Hamrick, 1992; Hamrick and Mills, 2000; Ji, 2008):

$$(\tau_{xz}, \tau_{yz}) = (\tau_{bx}, \tau_{by}) = C_b \sqrt{u_{bl}^2 + v_{bl}^2}\,(u_{bl}, v_{bl}) \tag{12}$$

$$(\tau_{xz}, \tau_{yz}) = (\tau_{sx}, \tau_{sy}) = C_s \sqrt{U_w^2 + V_w^2}\,(U_w, V_w) \tag{13}$$

where τ_{bx} and τ_{by} are bottom shear stresses; τ_{sx} and τ_{sy} are surface shear stresses; u_{bl} and v_{bl} are velocities at the midpoint of the bottom layer; U_w and V_w are wind velocity components at 10 m above the water surface. The bottom drag coefficient (C_b) is given by:

$$C_b = \frac{k^2}{\ln\left(\frac{\Delta_{bl}}{2z_0^*}\right)^2} \tag{14}$$

where k is the von Karman constant (0.4), Δ_{bl} is the dimensionless bottom layer thickness, $z_0^* = z_0/H$ is the dimensionless roughness height, and z_0 is the bottom roughness height. The wind stress coefficient (C_s) is given by:

$$C_s = 0.001\frac{\rho_a}{\rho}\left(0.8 + 0.65\sqrt{U_w^2 + V_w^2}\right) \tag{15}$$

where ρ_a is air density.

For temperature transport modeling, the NOAA Geophysical Fluid Dynamics Laboratory atmospheric heat exchange model (Rosati and Miyakoda, 1988) or the CE-QUAL-W2 equilibrium temperature method (Craig, 2013; Cole and Wells, 2013) can be implemented for the water surface boundary condition.

Numerical Solution

The numerical scheme of the hydrodynamic equations uses second-order accurate spatial finite differencing on a staggered or C grid. Time integration uses a second-order accurate, three-time level or two-time level finite-difference scheme with an external-internal mode splitting procedure which separates the external free surface gravity wave (barotrophic mode) from the internal shear (baroclinic mode). The semi-implicit, external mode solution uses a preconditioned conjugate gradient procedure to compute the 2D water surface elevations, allowing relatively large time steps constrained only by the stability criteria of the high-order upwind advection scheme (Smolarkiewicz and Margolin, 1993) or the explicit central difference approach used for nonlinear accelerations (Jin et al., 2000). The internal mode equations are solved at the external mode time step, and are implicit with respect to vertical diffusion.

The transport equations for salinity, temperature, turbulence intensity and length scale, and other constituents are solved using a high order upwind scheme (Smolarkiewicz and Clark, 1986; Smolarkiewicz and Grabowski, 1990) known as the multidimensional positive definite advective transport algorithm (MPDATA), which is first-order accurate in space and second-order accurate in time (Hamrick, 1992). To minimize numerical diffusion, MPDATA within EFDC employs an optional anti-diffusive correction and flux limiter calculation (Smolarkiewicz and Grabowski, 1990).

Further details of the EFDC model formulation, finite difference numerical schemes, underlying assumptions and parameter representations may be found in Hamrick (1992) and Tetra Tech (2007a, 2007b and 2007c).

Model Grid

The model domain encompasses Humboldt Bay within the existing shoreline (Laird, 2013), the larger slough and lower tributary systems (e.g. Mad River Slough, Freshwater Creek, Elk River), and a portion of the open ocean immediately outside of the entrance channel (Figure 3-1). The model grid is based on a previously developed 3D hydrodynamic and transport model for Humboldt Bay (Anderson, 2010), but was configured as a 2D model for the 100-yr long SLR simulations to increase computational efficiency. The curvilinear-orthogonal grid consists of 1,560 horizontal cells and one vertical layer, with an average orthogonal deviation of 2.3 degrees. Grid cells had an average size of 205.6 by 219.7 m, ranging in size from 12.7 to 678.8 m in the x-direction and 25.8 to 514.7 m in the y-direction.

Figure 3-1 Humboldt Bay hydrodynamic model grid domain.

Elevations were assigned to the grid cells using the Humboldt Bay project DEM developed by PWA (2014) as part of the overall SLR vulnerability work (Figure 3-2).

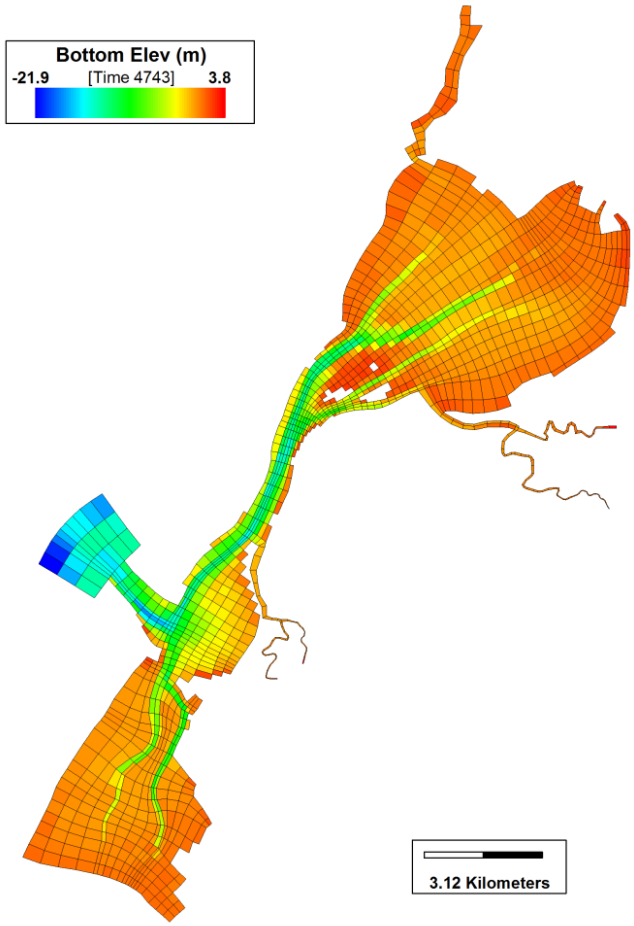

Figure 3-2 Humboldt Bay hydrodynamic model grid and bottom elevations (m) referenced to NAVD88.

The grid configuration required a 2 second time step to satisfy the Courant-Friedrich-Lewy (CFL) criteria and reduce oscillations in the solution field. The 100-yr simulations required approximately 155 CPU hours on a Pentium 3.2 GHz 6-Core Pentium Processor (overclocked to 4.8 GHz) using the DSI multi-threaded version of EFDC (EFDC_DSI_OMP). Model results were output at 15 minute intervals.

Model parameters and Initial conditions

Model parameters (Table 3-1) were based on values from a previously developed and semi-calibrated three-dimensional EFDC hydrodynamic and transport model of Humboldt Bay (Anderson, 2010).

The adjusted parameter representing bottom drag (or friction) is the total effective roughness height (Z_0), which represents the total roughness due to skin friction and form drag. A constant Z_0 of 0.005 m was used for the entire model domain. Horizontal eddy viscosity was set to zero for the SLR simulations. It was assumed that the numerical diffusion associated with the EFDC model (Hamrick, 1992) is likely similar in magnitude as realistic eddy viscosity values.

Table 3-1 Key EFDC model parameters.

Parameter	Value	Source/Description
Effective roughness height (Z_0)	0.005 m	Based on Anderson (2010), and calibrated within range of literature values (Ji 2008, Tetra Tech 2007b)
Horizontal eddy viscosity	0	Assumed zero
Wet/dry depth	0.01 m	Adjusted for model stability, within range of bathymetric data accuracy
Model time step	2 sec	Adjusted for model stability

For each EFDC model run, the model was spun-up for 7 days prior to the effective start date of each SLR simulation. The water surface elevation was set to the value taken from the ocean boundary condition at the start of the 7-day spin-up period. The initial velocities were set as zero. The 7-day model spin-up period was of adequate length to remove the initial condition effects from the water surface elevation solution field.

4 Hydrodynamic Model Ocean Boundary Condition

The developed Humboldt Bay 2D model was driven only by a 100-yr long hourly sea level height series (1913 to 2012) at the ocean boundary. Freshwater inflows tributary to Humboldt Bay were not included. The effects of internally generated wind waves on predicted water levels in Humboldt Bay for the 100-yr simulations were not directly assessed. Inclusion of these effects where beyond the scope and funding available for this study.

Tidal Observations

The ocean boundary of the model domain is located approximately 1.8 km west of the Humboldt Bay entrance (Figure 3-1). The National Oceanic and Atmospheric Administration (NOAA) Center for Operational Oceanographic Products and Services (CO-OPS) currently operates two tide gauges in the Humboldt Bay region (or near the model domain) with water level observations (Figure 1-1 and Table 4-1): North Spit (NOAA tide gauge 9418767) located interior to Humboldt Bay and 3.7 km from the entrance, and Crescent City (NOAA tide gauge 9419750) located 109 km north of the entrance.

The Crescent City tide gauge has a much longer record of hourly water level observations than the North Spit gauge. The monthly highest water level observations are derived from the hourly and six-minute tidal observations (NOAA, 2013). Verified six-minute water level observations are available for the North Spit and Crescent City gauges, but cover a much shorter observation period beginning in January 1996. Due to the longer period of tidal observations, the Crescent City hourly water level data was used to develop the ocean boundary condition (Table 4-1). This approach allowed the North Spit tidal observations to serve as a calibration/validation data set interior to Humboldt Bay.

Table 4-1 NOAA tide gauges and data summary in the Humboldt Bay region through year 2012.

	Verified Hourly Water Level Observations		Verified Monthly Highest Water Level Observations	
NOAA Tide Gauge	**Period**	**Number**	**Period**	**Number**
Crescent City (9419750)	1933-04-11 to 1943-10-11; 1945-01-20 to 1947-06-01; 1950-04-01 to 1964-03-28; 1964-07-31 to 1979-01-26; 1979-08-01 to 2000-08-31; 2001-01-01 to 2012-12-31	639,011	1933-01-01 to 1947-12-31; 1950-01-01 to 2012-12-31	867
North Spit (9418767)	1993-01-01 to 2012-12-31	174,509	1977-09-01 to 1977-12-31; 1978-05-01 to 2012-12-31	409

Water levels recorded at the NOAA gauges include the combined effects of astronomical tides and nontidal sea levels. Nontidal sea levels occur from local weather events such as storm surge, wind stress effects, and changes in barometric pressure; from larger interannual to decadal climate patterns such as the El Niño-Southern Oscillation (ENSO); and from decadal or longer climate variability such as the Pacific Decadal Oscillation (Cayan et al., 2008; Bromirski et al., 2011; NRC, 2012), all of which can increase or decrease the astronomical tide levels. The recorded water levels do not include wave effects, but may contain a limited amount of wave setup depending on the gauge's exposure to ocean waves (NOAA, 2013). Since the North Spit tide gauge is located inside Humboldt Bay and generally protected from ocean swell, the water level observations probably do not include significant wave effects. However, the Crescent City tide gauge location within the Crescent City Harbor, and the harbor's orientation to the open ocean may allow some wave setup effect in the tidal observations. NOAA (2013) notes that the water levels recorded at a NOAA gauge approximately correspond to what FEMA defines as still water elevation, and are not the 1% annual chance BFE which include wave effects.

100-year Long Detrended Hourly Sea Level Height Series

For predicting water levels in Humboldt Bay, the 2D model was forced by a 100-yr long (1913 – 2012) detrended hourly sea level height series (100-yr HSLH series) developed on data from the NOAA Crescent City tide gauge. The 100-yr HSLH series consists of 639,011 hourly water level observations (Table 4-1) and 246,373 hourly water level predictions with the long-term SLR and VLM signal removed (detrended) from the entire series. The 100-yr HSLH series includes the sea level height variability inherent in the historical Crescent City observed tidal record, and is of adequate length to make reliable estimates of extreme high water levels (e.g. 100-yr extreme high water level). The entire 100-yr HSLH series spanned 101-years (1912 to 2012) with the 1912 tide levels used for model spinup.

Hourly water level predictions were based on NOAA hindcast astronomical tide predictions for Crescent City, and a developed nontidal sea level model following the general approach of Cayan et al. (2008). This approach uses multi-linear regression to relate nontidal sea level residuals to weather (wind and sea level pressure) and ENSO variability. The general procedure to develop the hourly water level predictions for Crescent City follows.

1. Hourly observations and hindcasted tide predictions for Crescent City were downloaded from the NOAA CO-OPS website (http://tidesandcurrents.noaa.gov/), referenced to the tide gauges station datum (STND). The hourly observations were detrended using least-squares linear regression to remove the SLR and VLM signal from the data. The regression was on the hourly water level residuals generated by subtracting the NOAA Crescent City mean sea level (MSL) tidal datum value of 225.4 cm (1983-2001 NTDE) from the hourly observations. Detrending the hourly data effectively references the data to the middle of the current 1983-2001 NTDE (Flick et al., 2013), which for this work references midnight on 2 July 1992. The NOAA hindcasted tidal predictions generally

reproduce NOAA published tidal datum for the current 1983-2001 NTDE. Consequently, it was assumed for this work that the NOAA tide predictions represent detrended astronomical hindcasted tide predictions over the 1913-2012 period referenced to the 1983-2001 NTDE.

2. Hourly detrended nontidal sea level residuals were determined by subtracting the NOAA hindcasted astronomical tide predictions from the detrended water level observations from step 1 above.
3. Nontidal sea level model independent variables collected for analysis include wind velocity, sea level pressure (inverse barometer effect), and ENSO variability extracted from various reanalysis datasets for two time periods: 1912-1949 and 1950-2012. For the 1912-1949 period:
    - 6-hour wind velocity (u- and v-direction) and sea level pressure: 20th Century Reanalysis V2 data (Compo et al., 2011) provided by the NOAA Office of Oceanic & Atmospheric Research, Earth System Research Laboratory, Physical Sciences Division (NOAA/OAR/ESRL/PSD). All NOAA/OAR/ESRL/PSD data were downloaded from http://www.esrl.noaa.gov/psd.
    - Monthly ENSO variability over NINO 3.4 Region: monthly sea surface temperature anomalies averaged over the NINO 3.4 extracted region (120°W to 170°W longitude, 5°S to 5°N latitude) from Kaplan SST V2 data (Kaplan et al., 1998) provided by NOAA/OAR/ESRL/PSD.

    For the 1950-2012 period:
    - 6-hour wind velocity (u- and v-direction) and sea level pressure: NCEP/NCAR Reanalysis 1 data (Kalnay et al., 1996) provided by NOAA/OAR/ESRL/PSD.
    - Monthly ENSO variability for NINO 3.4 region: monthly 3-month averaged sea surface temperature anomalies for the NINO 3.4 region from ERSST.V3B dataset (1981-2010 base period) provided by the NOAA National Weather Surface Climate Prediction Center (downloaded from http://www.cpc.ncep.noaa.gov).
4. Seasonal multi-linear regression models were developed for two time periods (1933-1949, and 1950-2012), relating the observed hourly nontidal sea level residuals from step 2 (dependent variable) to the 6-hour wind velocity (u- and v-direction), 6-hour sea level pressure, and monthly ENSO values from step 3 (independent variables). Hourly estimates of the independent variables were determined from the 6-hour and monthly values using linear interpolation. The seasonal periods were September-November (fall), December-February (winter), March-May (spring), and June-August (summer). Seasonal regression models provided better correlations between predicted and observed nontidal residuals than an annual model.
5. The final hourly detrended water level predictions for Crescent City consisted of combining the NOAA hindcasted tide predictions (step 1) with the hourly detrended nontidal sea level predictions (step 4).

To create the 100-yr HSLH series (1913-2012) the 639,011 detrended hourly water level observations were combined with the 246,373 hourly water level predictions.

Adequacy of 100-yr Hourly Sea Level Height Series

Since the Humboldt Bay 2D model is driven solely by the 100-yr HSLH series, the created 100-yr series was assessed against water level observations at the Crescent City tide gauge. This section describes the accuracy of the 100-yr HSLH series, comparing predictions to observations with a focus on:

- Hourly nontidal sea level and water level prediction equations and statistics.
- Assumption of stationarity at middle of the 1983 to 2001 NTDE (midnight on 2 July 1992).
- Annual extreme high water estimates using generalized extreme value analysis.

The seasonal nontidal sea level model multi-linear regression equations and general correlation and fit statistics related to observations for the two model periods are summarized in Table 4-2.

Table 4-2 Multi-linear regression relations for the NOAA Crescent City tide gauge (9419750) nontidal sea level residuals (independent variable, cm) based on reanalysis datasets for ENSO variability, sea level pressure and u- and v-wind velocity (independent variables).

Model Period	Multi-linear Regression Coefficients[1]					Regression Statistics[2]		
	NIN0 3.4	SLP	u_Vw	v_Vw	INT	R	SE of Regression (cm)	Number of Obs
1933-1949								
Sep-Nov	3.07	-1.14	-0.16	0.68	1162.71	0.76	6.53	4,463
Dec-Feb	3.43	-1.31	-0.32	0.81	1329.29	0.85	8.40	4,427
Mar-May	3.25	-1.38	-0.29	0.61	1404.50	0.75	8.31	4,988
Jun-Aug	0.95	-0.87	-0.84	0.73	889.52	0.53	5.55	4,739
1950-2012								
Sep-Nov	2.52	-1.28	-0.12	0.19	1303.60	0.74	7.10	21,774
Dec-Feb	3.00	-1.50	-0.08	0.40	1523.62	0.85	8.90	21,860
Mar-May	2.81	-1.44	-0.20	0.28	1466.01	0.76	8.39	22,201
Jun-Aug	1.71	-1.10	-0.43	0.05	1121.04	0.53	5.96	22,048

[1]SLP is sea level pressure, u_Vw and v_Vw are u- and v-direction wind velocity components, respectively, and INT is intercept. [2]R is correlation coefficient, SE is standard error, and Obs is observations.

Correlation plots are shown in Figure 4-1 for the nontidal sea level predictions. Observations, and statistics are summarized in Table 4-3. Correlation coefficients (R) for the seasonal regression relations range from 53% to 85% with higher values for the winter, fall, and spring seasonal periods (Table 4-2), respectively, when storms and El Niño conditions more significantly affect sea levels. The standard error of the regressions (SE) range from 5.6 to 8.4 cm for the 1933 to 1949 period, and 6.0 to 9.0 cm for the 1950 to 2012 period, with the highest SE occurring in the winter season.

The standard deviations of the nontidal sea level predictions are similar to, but smaller than observations, with a correlation coefficient of approximately 79% for both model periods (Table 4-3). These results are consistent with the nontidal sea level model developed by Cayan et al. (2008) for Crescent City, which had an R value of 82% between observed and predicted nontidal sea levels. The correlation plots (Figure 4-1) show that predicted nontidal sea levels slightly underestimate and overestimate the higher and lower observations, respectively. One likely explanation for this is the 6-hour wind velocity and sea level pressure Reanalysis data, which are 6-hour averages that would tend to reduce peak values and raise low values that occur over shorter time scales (e.g. hourly).

Overall, the developed nontidal sea level models generally appear to reproduce observed nontidal sea level variability using the three independent variables of wind, sea level pressure and ENSO variability (Figure 4-2).

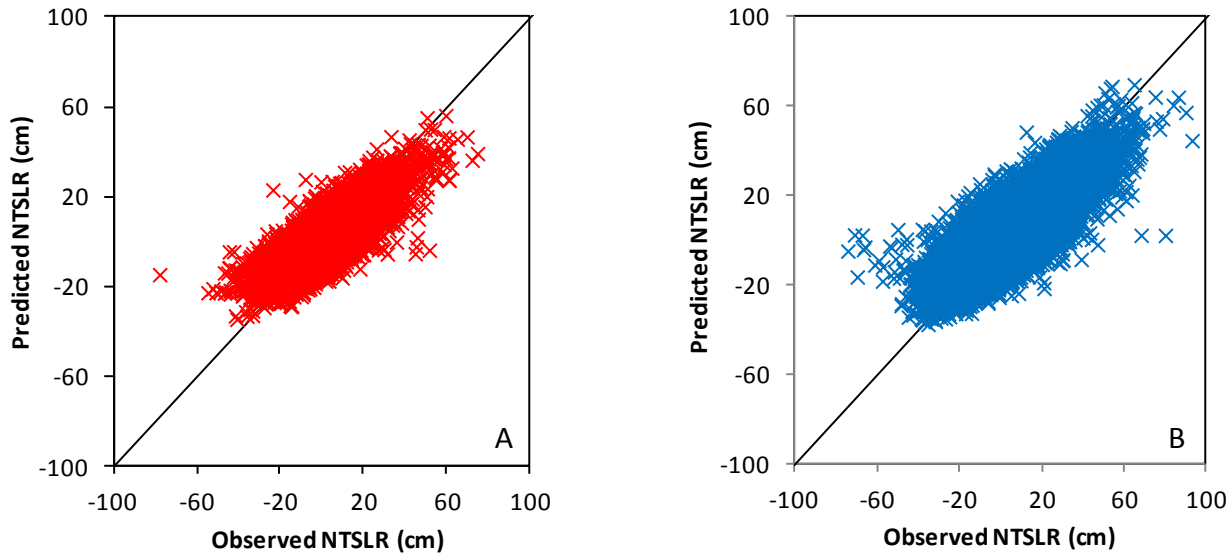

Figure 4-1 Predicted and observed nontidal sea level residual (NTSLR) correlations for the NOAA Crescent City tide gauge (9419750) for the two multi-linear regression model periods. Plot A shows the NTSLR correlation from the regression model developed for the 1933-1949 period, and plot B shows the NTSLR correlation for the 1950-2012 period regression model.

Table 4-3 Summary statistics for nontidal sea level residuals from the multi-linear regression models and water level predictions for the NOAA Crescent City tide gauge (9419750)[1].

Model Period	Statistics for Hourly Nontidal Sea Level Predictions			Statistics for Water Level Predictions (astronomical tide plus nontidal sea level)		
	R	SD of Obs (cm)	SD of Pred (cm)	R	SD of Obs (cm)	SD of Pred (cm)
1933-1949	0.785	11.78	9.25	0.994	65.43	65.46
1950-2012	0.788	12.45	9.81	0.993	66.06	65.83

[1]R is correlation coefficient, SD is standard deviation, Obs is observation, and Pred is prediction.

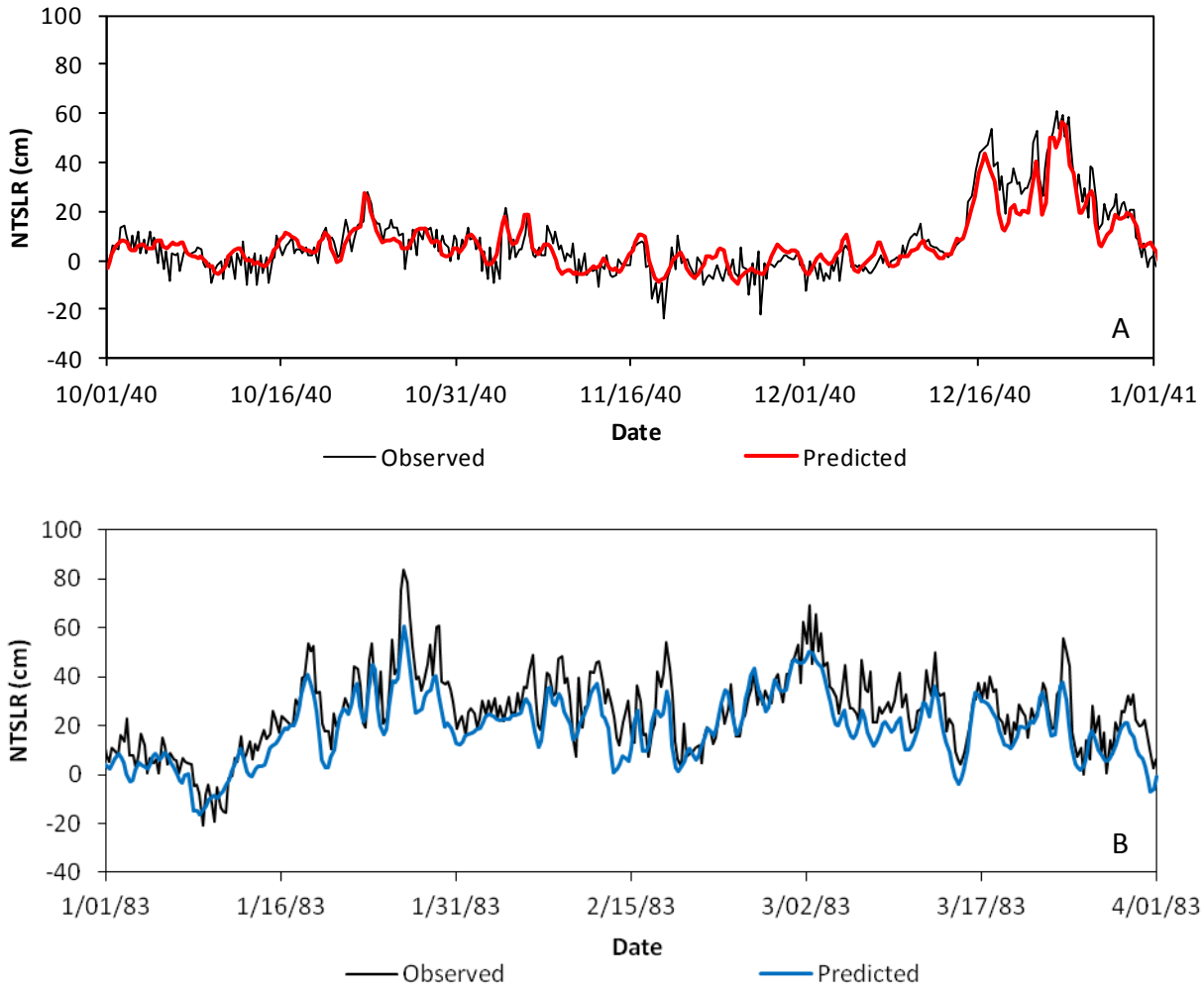

Figure 4-2 Time series of predicted and observed nontidal sea level residuals (NTSLR) for the NOAA Crescent City tide gauge (9419750) for two El Niño periods; October-December 1940 (A), and January-March 1983 (B).

The predicted hourly water levels (astronomical tide plus nontidal sea level) were used to fill data gaps in the 100-yr HSLH series. Statistics for the hourly water level predictions with observations are summarized in Table 4-3. Figure 4-3 shows correlation plots of predicted and observed water levels for the two model periods. The high correlation coefficient of 99% for both model periods indicate that predicted hourly water level variability is essentially the same as observed, with the largest difference in standard deviations between predictions and observations of only 0.23 cm (Table 4-3).

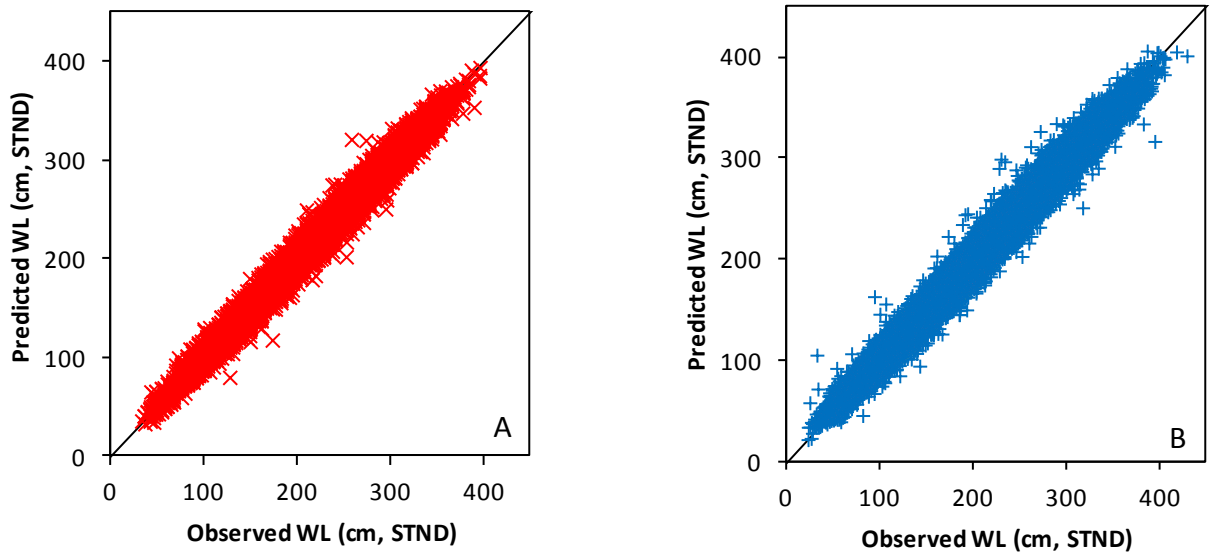

Figure 4-3 Predicted and observed hourly water level (WL) correlations for the NOAA Crescent City tide gauge (9419750) for the two multi-linear regression model periods. Plot A shows the water level correlation for the regression model developed for the 1933-1949 period, and plot B shows the water level correlation for the 1950-2012 period regression model.

Figure 4-4 shows monthly MSL estimated from the hourly observations, both reported and detrended, and from the final 100-yr HSLH series. The observed water levels (A in Figure 4-4), prior to detrending, exhibit an overall downward trend in the monthly MSL showing the combined effects of SLR and VLM, and indicates the RSL rise trend for the Crescent City tide gauge. Detrending the hourly observations (B in Figure 4-4) removes the RSL rise trend and creates stationary monthly MSL about the reported NOAA MSL for the 1983-2001 NTDE. The monthly MSL from the 100-yr HSLH series (C in Figure 4-4) also indicate a stationary series from the combined detrended observed and predicted sea levels.

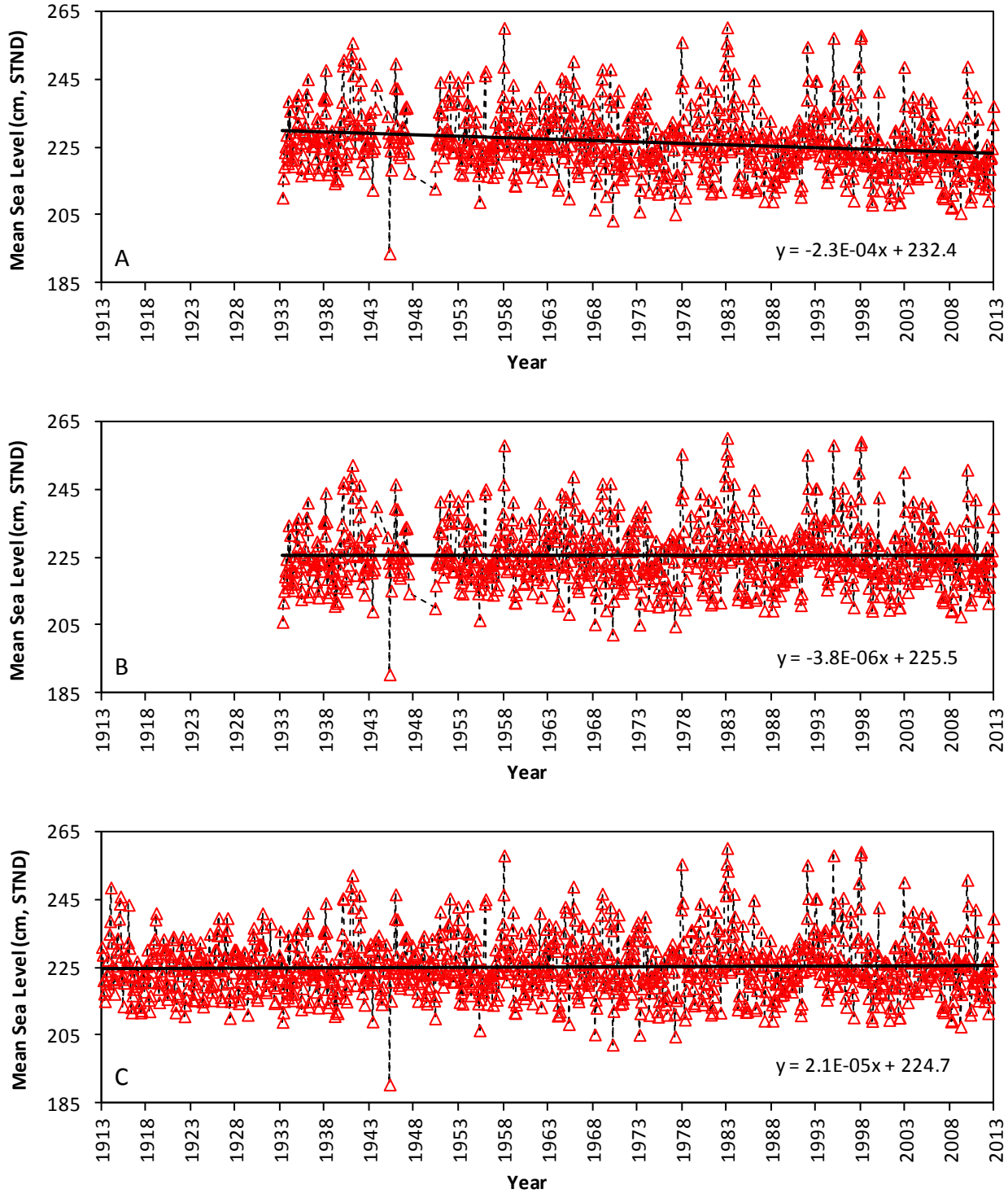

Figure 4-4 Crescent City NOAA tide gauge (9419750) monthly mean sea level (MSL) estimated from hourly water level records referenced to STND. Observed monthly MSL for period of record showing combined effects of SLR and VLM resulting in overall downward trend (A). Detrended observed monthly MSL (B). Observed and predicted monthly MSL from the 100-yr HSLH series (C).

To further assess data stationarity and assumptions, comparisons were made between reported NOAA tidal datum and estimates from the 100-yr HSLH series. The Crescent City tide gauge reported MSL, mean higher high water (MHHW) and mean lower low water (MLLW) tidal datum for the 1983-2001 NTDE are listed in Table 4-4. These datum were also estimated from the NOAA astronomical tide predictions, detrended hourly observations, and the detrended 100-yr HSLH series (Table 4-4). Overall, the 100-yr HSLH series appears relatively stationary around the 1983-2001 NTDE, with a difference of -3 mm between the reported MSL and MHHW and the estimated values from the 100-yr HSLH series. It is worth noting the 2 cm difference between the reported MLLW tidal datum (112.4 cm) and the estimated values from the NOAA tide predictions (114.4 cm), the detrended hourly observations (114.4 cm), and the 100-yr HSLH series (114.0 cm). It is not clear why this discrepancy exists with the MLLW values.

Table 4-4 Crescent City NOAA tide gauge (9419750) tidal datum comparison summary for mean higher high water (MHHW), mean sea level (MSL) and mean lower low water (MLLW) from various tide data sources.

Tide Data Source	Tidal Datum (cm, STND)		
	MHHW	MSL	MLLW
NOAA reported values (1983-2001 NTDE)	321.9	225.4	112.4
NOAA hindcasted hourly tide predictions (1913-2012)	322.0	225.4	114.4
NOAA detrended hourly observations (1933-2012)	321.7	225.4	114.4
100-yr HSLH series (1913-2012)	321.6	225.1	114.0

A final assessment of the accuracy of the developed 100-yr HSLH series was performed by comparing probabilities of exceedance for annual extreme high water level estimates (e.g. 100-yr event) from the 100-yr HSLH series to reported NOAA highest monthly observations. To develop the NOAA annual maximum water level series, the reported NOAA highest monthly water level observations (Table 4-1) were first detrended to the middle of the 1983-2001 NTDE using the same linear equation used to detrend the hourly observations. A 77-yr annual maximum series was generated from the detrended NOAA highest monthly observations, and the detrended 100-yr HSLH series provided a 100-yr annual maximum series. Exceedance probabilities and return intervals of extreme high water level events were determined for both annual maximum series using a generalized extreme value (GEV) analysis. Results of the GEV analysis for both annual maximum series are summarized in Table 4-5 and the exceedance

probability curves are provided in Figure 4-5. The 100-yr annual maximum water level series, estimated from the 100-yr HSLH series, reasonably reproduces the annual extreme high water level estimates generated from the 77-yr NOAA annual maximum series, with differences ranging between -2.2 cm and 2.7 cm.

Table 4-5 Comparison of annual extreme high water level probability estimates for Crescent City NOAA tide gauge (9419750) from the 77-yr observation record and the 100-yr long hourly sea level height (HSLH) series.

Probabilities of Exceedance (%)	Return Interval (years)	1933-2012 NOAA Highest Monthly Observations (cm, STND)	1913-2012 100-yr HSLH Series (cm, STND)	Difference (cm)
99.0	1.01	365.8	367.9	-2.2
90.9	1.1	375.6	376.0	-0.4
66.7	1.5	386.3	385.2	1.1
50.0	2	392.0	390.3	1.7
20.0	5	404.5	401.9	2.6
10.0	10	411.6	409.0	2.7
4.0	25	419.5	417.2	2.3
2.0	50	424.7	422.9	1.8
1.0	100	429.2	428.1	1.1
0.2	500	437.9	438.8	-0.9

Summary

Based on results of the above assessment, the developed 100-yr HSLH series, generated from 639,011 hourly water level observations and 246,373 hourly water level predictions, appears to reproduce water level observations for the Crescent City tide gauge with reasonable accuracy. The detrended 100-yr HSLH series is stationary about the 1983-2001 NTDE, and reproduces reported NOAA tidal datum (Figure 4-4 and Table 4-4). Furthermore, the 100-yr HSLH series reasonably reproduces extreme high water level events compared to extreme events generated from NOAA high water observations (Table 4-5 and Figure 4-5).

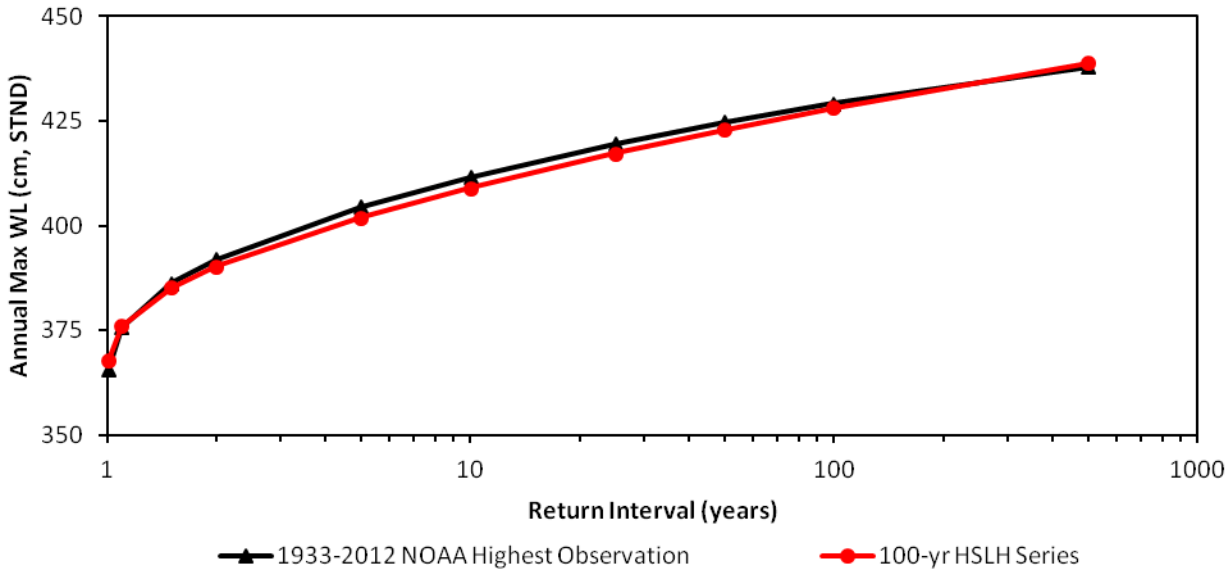

Figure 4-5 Annual extreme high water level (WL) probability curves for Crescent City NOAA tide gauge (9419750) from the 77-yr observation record and the 100-yr long hourly sea level height (HSLH) series.

Sea Level Rise Modeling Scenarios

For modeling purposes the detrended 100-yr HSLH series was converted from STND to NAVD88 using the published NOAA and National Geodetic Survey (NGS) datum conversion (STND – 1.240 m = NAVD88) for the Crescent City tide gauge (downloaded from http://tidesandcurrents.noaa.gov/gauges.html?type=Datums#California).

Five SLR scenarios were assessed for Humboldt Bay (Table 4-6 and Figure 4-6): year 2012 existing sea levels, and half-meter SLR increments of 0.5, 1.0, 1.5 and 2.0 m. For each SLR scenario a constant step SLR was added to the detrended 100-yr HSLH series, referenced to year 2000 so that the SLR scenarios could be related to the modified NRC (2012) SLR projections. To adjust the 100-yr HSLH series to year 2000, which was referenced to the middle of the 1983-2001 NTDE (midnight on 2 July 1992), the ReMSL rise rate of 2.28 mm/yr (Burgette et al., 2009) was applied for 8 years (0.018 m adjustment). The 2.28 mm/yr ReMSL rate applied to an additional 12 years (0.027 m adjustment) was used to estimate the step SLR for the year 2012 existing sea levels simulation.

To assist with 2D model calibration and demonstrate the ability of the model to reproduce observed water levels in Humboldt Bay, a 100-yr HSLH series was developed that included the ReMSL rise rate (100-yr HSLH calibration series). The 100-yr HSLH calibration series was created by adjusting the detrended 100-yr HSLH series for the ReMSL rate of 2.28 mm/yr relative to the middle of the 1983-2001 NTDE (midnight 2 July 1992).

Table 4-6 Humboldt Bay 100-yr long sea level rise (SLR) scenarios and assumptions[1].

Conditions and SLR Scenarios	Effective Date	Step SLR (m)	100-yr Model Simulation
Detrended 100-yr HSLH series referenced to middle of 1983-2001 NTDE	1992-07-02, 00:00		No
Year 2000 (base condition), step ReMSL rise rate of 2.28 mm/yr over 8 years from 2 July 1992	2000-07-02, 00:00	0.018	No
Year 2012 existing sea level, step ReMSL rise rate of 2.28 mm/yr over 12 years from 2 July 2000	2012-07-02, 00:00	0.027	Yes
Year 2000 + 0.5 m	Not defined	0.500	Yes
Year 2000 + 1.0 m	Not defined	1.000	Yes
Year 2000 + 1.5 m	Not defined	1.500	Yes
Year 2000 + 2.0 m	Not defined	2.000	Yes

[1]Regional mean sea level (ReMSL) rise rate of 2.28 mm/yr from Burgette et al. (2009).

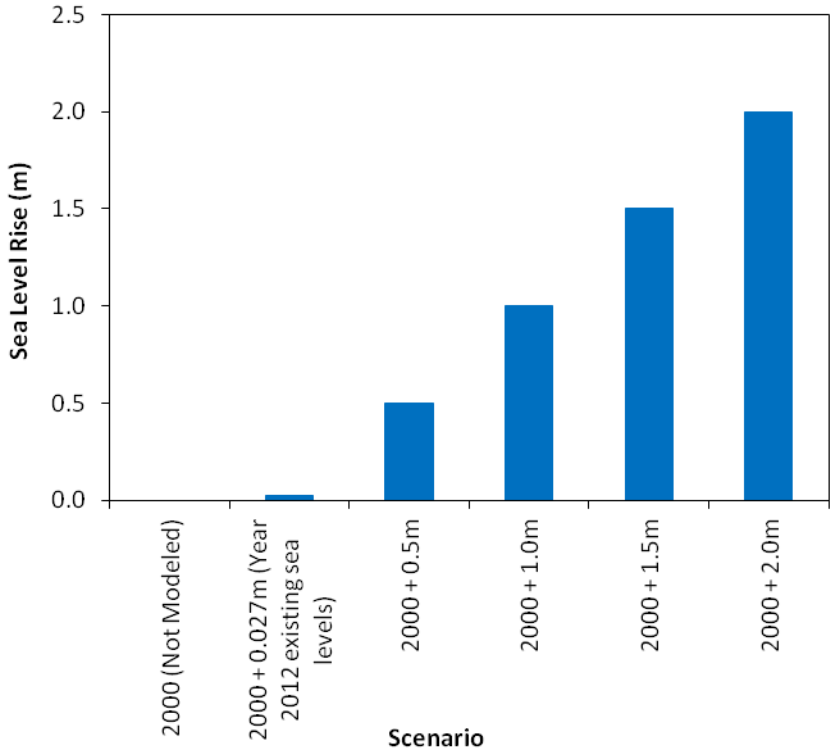

Figure 4-6 Humboldt Bay 100-yr long sea level rise (SLR) scenarios.

5 Hydrodynamic Model Results

This section summarizes the ability of the 2D hydrodynamic model, driven only by the 100-yr HSLH series boundary condition developed for the Crescent City tide gauge, to reproduce observed water levels in Humboldt Bay. Time-series graphs, correlation plots and statistics between water level predictions and observations are provided at five NOAA tide gauges in Humboldt Bay (Table 5-1 and Figure 2-11). These five tide gauges also coincide with the gauges used in Cascadia GeoSciences (CG) ongoing study to estimate tectonic land-level changes, or VLM, in Humboldt Bay (Patton et al., 2014). Recently, Patton et al. (2014) updated the VLM estimates at the five Humboldt Bay tide gauges (Table 2-3). For the North Spit gauge, comparisons could be made between observations and predictions for the Year 2012 existing sea levels scenario (Table 5-1). For the other historic tide gauges, comparisons between observations and predictions could only be made for the calibration simulation with the 100-yr HSLH series adjusted for the Burgette et al. (2009) ReMSL rise rate of 2.28 mm/yr. Distinctions between the simulations will be further discussed.

Available Hourly Tidal Observations in Humboldt Bay

The North Spit tide gauge is the only active tide gauge in Humboldt Bay (Table 5-1), with the other gauges considered historic. Three of the gauges, North Spit, Samoa and Fields Landing, have records of hourly water level observations collected by NOAA, with different periods of record (tidal data downloaded from http://tidesandcurrents.noaa.gov). The other two gauges, Mad River Slough and Hookton Slough, do not have hourly observations available from NOAA, but do have water level observations collected by others. NHE collected water levels at the approximate historic Mad River Slough tide gauge location from about March to June 2008 (NHE, 2009). As part of the CG study, CG and NHE collected water levels at the location of the historic Hookton Slough tide gauge from approximately August to December 2012 (Patton et al., 2014).

Tide levels were either downloaded from the NOAA CO-OPS website or calculated for each tide gauge referenced to STND, and converted to NAVD88 using the published NOAA and NGS datum and/or benchmark data for each gauge from http://tidesandcurrents.noaa.gov.

Table 5-1 Summary of Humboldt Bay NOAA tide gauge data used for comparison with model results.

NOAA Tide Gauge, Status	Data Source, Number of Hourly Observations	Period of Record	Hydrodynamic Model Simulation
Fields Landing (9418723), historic	NOAA; 2,461 observations	2010-11-30 14:00 to 2011-03-13 02:00	100-yr HSLH calibration series
Hookton Slough (9418686), historic	CG and NHE; 3,008 observations	2012-08-02 09:00 to 2012-12-05 16:00	100-yr HSLH calibration series
Mad River Slough (9418865), historic	NHE; 2,347 observations	2008-03-18 18:00 to 2008-03-18 12:00	100-yr HSLH calibration series
North Spit (9418767), active	NOAA; 174,509 observations	1993-01-01 00:00 to 2012-12-31 00:00	Year 2012 existing sea levels
Samoa (9418817), historic	NOAA; 2,398 observations	2010-11-30 12:00 to 2011-03-10 09:00	100-yr HSLH calibration series

Water Level Comparisons

This section summarizes the methods used to compare water level observations with 2D model predictions and corresponding results at the five tide gauge locations in Humboldt Bay. The resolution of the 2D model grid used in this study does not capture the smaller channels located in the shallow areas of North and South Bays. Two of the tide gauges, Mad River Slough and Hookton Slough, are located in these smaller channels. The 2D model could not predict the full tidal range observed at these gauges due to the shallow elevation of the grid cells; however, the 2D model did adequately predict the upper half of the tidal range at the Mad River Slough and Hookton Slough tide gauges.

North Spit Tide Gauge

Comparisons between North Spit observations and predictions were provided for the entire hourly water level record, the daily maximum water level, and the annual extreme high water level. Due to the relatively long period of recorded tidal observations at the North Spit tide gauge (Table 4-1 and Table 5-1), the available data was detrended using least-squares linear regression to remove the SLR and VLM signal, and compared to results from the Year 2012 existing sea levels simulation. The North Spit hourly water level linear regression was applied to the hourly MSL residuals, while the highest monthly observations were detrended relative to the monthly MSL residuals. It was necessary to adjust the detrended North Spit observations (referenced to midnight 2 July 1992) to year 2012, the effective date of the 100-yr long Year 2012 existing sea levels simulation, by applying the 2.28 mm/yr ReMSL rise rate (Burgette et al., 2009) over 20 years, for a total of 4.56 cm.

A time-series of hourly observed and predicted North Spit water levels during February 1998, including a correlation plot between observed and predicted hourly water levels are provided in Figure 5-1. Since the inundation mapping developed for this study relied on the daily maximum water levels generated from the 2D model, a correlation plot between observed and predicted daily maximum water levels is also provided in Figure 5-1.

Predicted and observed water level means, standard deviations, and correlation coefficients for the hourly water levels and daily maximum water levels are summarized in Table 5-2 and Table 5-3, respectively. Predicted mean water level was similar to the observed value with a difference of 0.9 cm. The predicted and observed standard deviations were similar with a difference of 1.6 cm, indicating that the 2D model reproduces observed water level variability well. Figure 5-1 illustrates the high correlation coefficients (0.996 and 0.975) for both water level analyses, verifying the good prediction of water levels for the North Spit gauge. The data points that significantly deviate from the 1:1 line in the correlation plots (Figure 5-1), are associated with tsunami events that have been recorded in the North Spit and Crescent City tidal observations.

Table 5-4 summarizes the reported NOAA tidal datum (MSL, MLLW and MHHW) at the North Spit gauge, and estimates from the 100-yr predicted water levels. To compare observed and predicted tidal datum, the NOAA values were adjusted by 4.56 cm to account for a ReMSL rise rate of 2.28 mm/yr over 20 years. The 100-yr predictions reasonably reproduce reported MHHW, MSL and MLLW North Spit tidal datum, with differences of 0.2, 1.0 and 1.6 cm, respectively.

Thirty-five years of annual maximum water levels are available for the North Spit gauge from 1978 to 2012. The relatively long period of highest monthly observations at the North Spit gauge (Table 4-1) allowed for a comparison of predicted and observed extreme high water levels. The 1981 annual maximum water level value is approximately 1.4 meters higher than the next highest North Spit water level in 1983. In Crescent City, the highest observed water level for the 77-yr record was in 1983. Consequently, the 1981 North Spit annual maximum water level was considered an outlier and removed from the analysis, resulting in a 34-yr detrended annual maximum observed water level series for the North Spit gauge. The 2D model predictions for North Spit generated a 100-yr long detrended annual maximum water level series. A generalized extreme value (GEV) analysis provided probabilities of exceedance for extreme events for both of the annual maximum series. Results of the GEV analyses are summarized in Table 5-5 and the exceedance probability curves are provided in Figure 5-2. The 100-yr predicted annual maximum series reasonably reproduces, although somewhat over-predicts, the annual extreme high water level estimates from the 34-yr observed annual maximum series. Differences ranged from 3.2 to 7.0 cm. One possible explanation for the over-prediction of extreme events is the longer period of record between predictions (100-yr) and observations (34-yr).

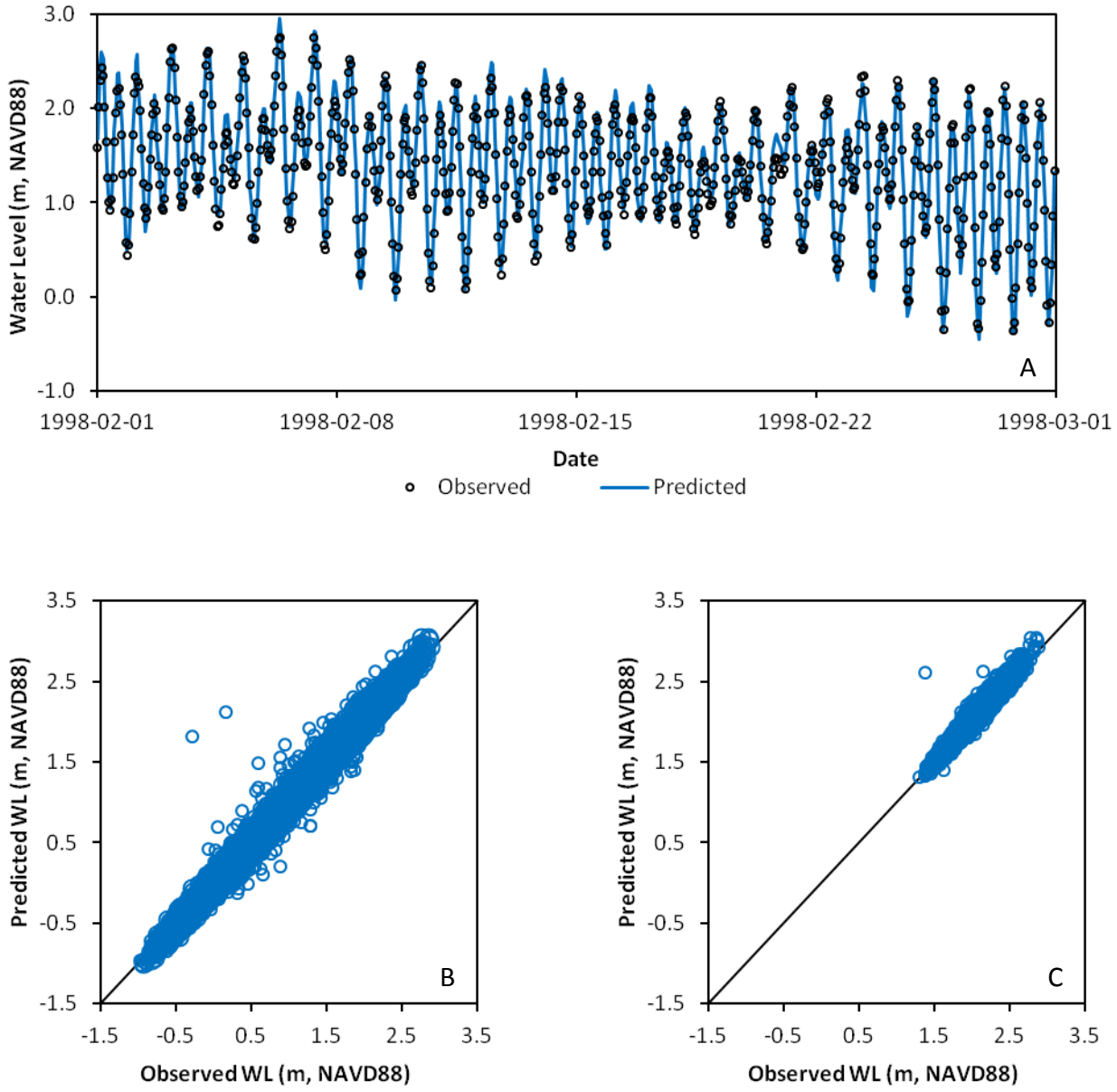

Figure 5-1 Time series and correlation plots of observed and predicted water levels (WL) for North Spit NOAA tide gauge (9418767). Tidal observations were from NOAA and were detrended prior to comparison. Plot A is a time series for February 1998, plot B is the correlation between predicted and observed hourly water levels, and plot C is the correlation between predicted and observed daily maximum water level. The data points that significantly deviate from the 1:1 line in the correlation plots were associated with tsunami events in the North Spit and Crescent City tide records.

Table 5-2 Statistics for hourly water level observations and predictions for Humboldt Bay tide gauges[1].

NOAA Tide Gauge	Average (cm)		Standard Deviation (cm)		Fit Statistics	
	Observed	Predicted	Observed	Predicted	R	No of Obs.
Fields Landing (9418723)	107.6	110.0	65.2	66.5	0.995	2,461
North Spit (9418767)	107.1	106.2	62.9	64.5	0.996	174,509
Samoa (9418817)	111.3	110.3	67.6	68.3	0.993	2,398

[1]Hourly water level statistics were not provided for Hookton Slough and Mad River Slough tide gauges.

Table 5-3 Statistics for daily maximum water level observations and predictions for Humboldt Bay tide gauges.

NOAA Tide Gauge	Average (cm)		Standard Deviation (cm)		Fit Statistics	
	Observed	Predicted	Observed	Predicted	R	No of Obs.
Fields Landing (9418723)	207.9	211.1	24.3	24.3	0.977	102
Hookton Slough (9418686)	205.5	204.4	18.9	20.5	0.972	124
Mad River Slough (9418865)	199.5	197.7	24.4	23.9	0.987	97
North Spit (9418767)	203.1	203.4	22.7	23.4	0.975	7,272
Samoa (9418817)	217.9	217.0	25.2	25.5	0.981	99

Table 5-4 Comparison of observed and predicted North Spit tidal datum for mean higher high water (MHHW), mean sea level (MSL) and mean lower low water (MLLW).

Tide Data Source	Tidal Datum (cm, NAVD88)		
	MHHW	MSL	MLLW
NOAA published values for 1983-2001 NTDE	198.7	102.5	-10.3
NOAA published values for 1983-2011 NTDE + 4.56 cm (2.28 mm/yr ReMSL rise rate for 20-years)	203.3	107.1	-5.7
Predicted 100-yr hourly water levels for 1913-2012 period	203.1	106.1	-7.3

Table 5-5 Comparison of observed (34-yr record) and predicted (100-yr record) annual extreme high water level probability estimates for North Spit NOAA tide gauge (9418767).

Probabilities of Exceedance (%)	Return Interval (years)	1978-2012 NOAA Highest Monthly Observations (cm, NAVD88)[1]	1913-2012 100-yr EFDC Predicted Series (cm, NAVD88)	Difference (cm)
99.0	1.01	242.8	249.5	-6.7
90.9	1.1	250.8	257.8	-6.9
66.7	1.5	260.0	267.0	-7.0
50.0	2	265.2	272.2	-7.0
20.0	5	277.4	284.1	-6.7
10.0	10	284.9	291.3	-6.4
4.0	25	293.9	299.7	-5.8
2.0	50	300.1	305.4	-5.3
1.0	100	305.9	310.6	-4.7
0.2	500	318.2	321.4	-3.2

[1]Assumed 1981 maximum annual water level was an outlier and removed from analysis.

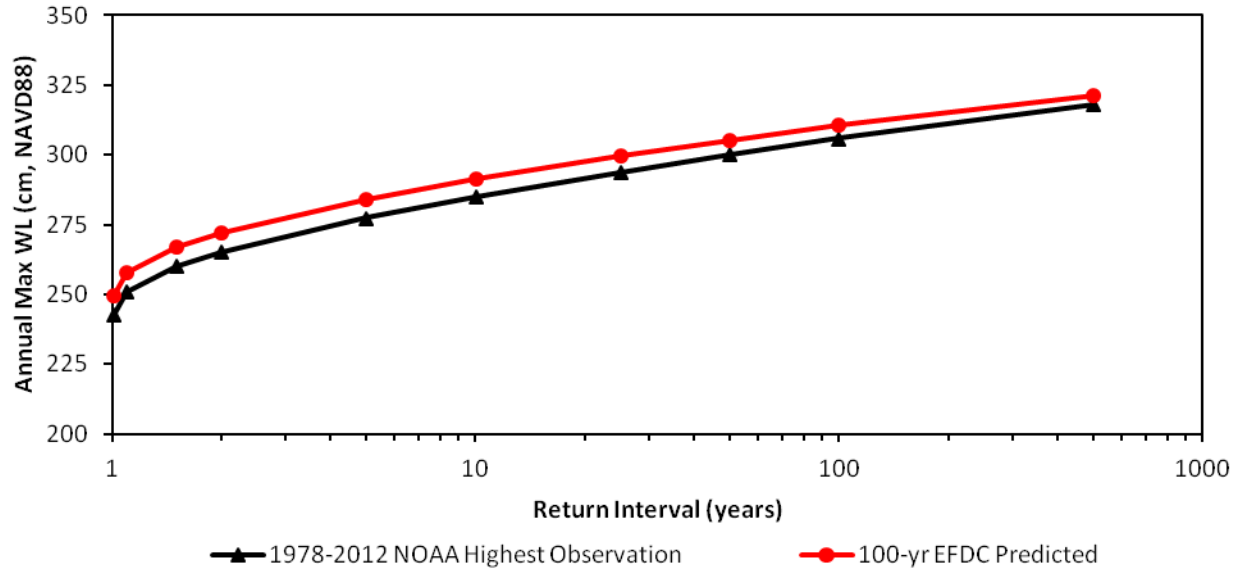

Figure 5-2 Annual extreme high water level (WL) probability curves for North Spit NOAA tide gauge (9418767) from the 34-yr observation record and the 100-yr predicted WL.

Other Humboldt Bay Tide Gauges

Comparisons between observations and predictions are provided for the hourly water level and/or the daily maximum water level observation records for the other four tide gauges in Table 5-1 (Fields Landing, Hookton Slough, Mad River Slough and Samoa). As noted earlier, the 2D model grid resolution at the Mad River Slough and Hookton Slough tide gauge locations does not capture the full-observed tidal range, and only the daily maximum water levels were assessed at these two gauges.

For the Fields Landing, Hookton Slough, Mad River Slough and Samoa tidal gauges, the period of tidal observations is not long enough to detrend the data and remove the SLR and VLM trend. Instead, these tidal observations were compared to predictions from the simulation that used the 100-yr HSLH calibration series boundary condition that was adjusted for the ReMSL rise rate of 2.28 mm/yr. The tidal observations at these four tide gauges include the effects of both SLR and VLM. Although the 100-yr HSLH calibration series accounts for the ReMSL rise rate of 2.28 mm/yr, it does not account for VLM, which increases or decreases the RSL rise at each tide gauge. To compensate for this difference, the appropriate VLM rate estimate (Table 2-3) was added to each of the four tide gauges (Fields Landing, Hookton Slough, Mad River Slough and Samoa) tidal observations by the time before or after midnight on 16 June 1991. The NGS benchmark data sheets (http://www.ngs.noaa.gov) for each tide gauge indicate that June 1991 is the date of the most recent orthometric height adjustment, which for this work was assumed to be midnight on 16 June 1991. The correlation plots of daily maximum water levels for Hookton Slough (Figure 5-3) show the effect of adjusting the observations by the VLM. The bottom left correlation plot (B in Figure 5-3) show the results prior to adjusting for VLM, and the bottom right correlation plot (C in Figure 5-3) shows the data fit following VLM adjustment. The VLM adjustment to the tidal observations clearly improves the daily maximum water level correlation for Hookton Slough. The effect of the VLM adjustment is only demonstrated in Figure 5-3 for Hookton Slough. The remaining figures and statistics for the Fields Landing, Hookton Slough, Mad River Slough and Samoa tide gauges compare the VLM adjusted observations with predictions.

Water level observations are compared to predictions in Figure 5-3 to Figure 5-6 for Hookton Slough, Fields Landing, Mad River Slough and Samoa tide gauges, respectively. Water level means, standard deviations, and correlation coefficients between observations and predictions for hourly and daily maximum water levels are summarized in Table 5-2 and Table 5-3, respectively. For Fields Landing and Samoa the model grid allows the full tidal range to be simulated at these gauges. The Fields Landing (Figure 5-4) and Samoa (Figure 5-6) plots, low differences between the means and standard deviations. and the high correlation coefficients for the hourly data (Table 5-2) and the daily maximum water level (Table 5-3), respectively, indicate similar comparison between observations and predictions at these gauges as for North Spit. The effects of the March 2011 tsunami are visible in the correlation plots for Fields Landing (Figure 5-4).

For Hookton Slough (Figure 5-3) and Mad River Slough (Figure 5-5), the model grid resolution does not allow the full tidal range to be simulated, but the higher hourly water level predictions compare well with observations. The relatively low differences between the means and standard deviations, and the high correlation coefficients (Table 5-3) indicate good comparison between observations and predictions for daily maximum water levels at the Mad River Slough and Hookton Slough gauges.

Summary

Results indicate that the 2D hydrodynamic model driven only by the 100-yr HSLH series developed for the Crescent City tide gauge reproduces Humboldt Bay observed water levels reasonably well. At the Humboldt Bay tide gauges where the model grid resolution allows simulation of the full tidal range (North Spit, Fields Landing and Samoa), results show a very good comparison between predicted and observed means and standard deviations. The high correlation coefficients between these data series indicate a good overall correlation between observed and predicted hourly water levels. For the North Spit tide gauge, a generalized extreme value (GEV) analysis shows that the 100-yr predicted annual maximum series reasonably reproduces, although slightly over-predicts, annual extreme high water levels calculated from the 34-yr observation record. Results for all tide gauges (Fields Landing, Hookton Slough, Mad River Slough, North Spit and Samoa) show that predicted daily maximum water levels compare well with observations for inundation vulnerability mapping and other analysis in this study that rely on the daily maximum water levels.

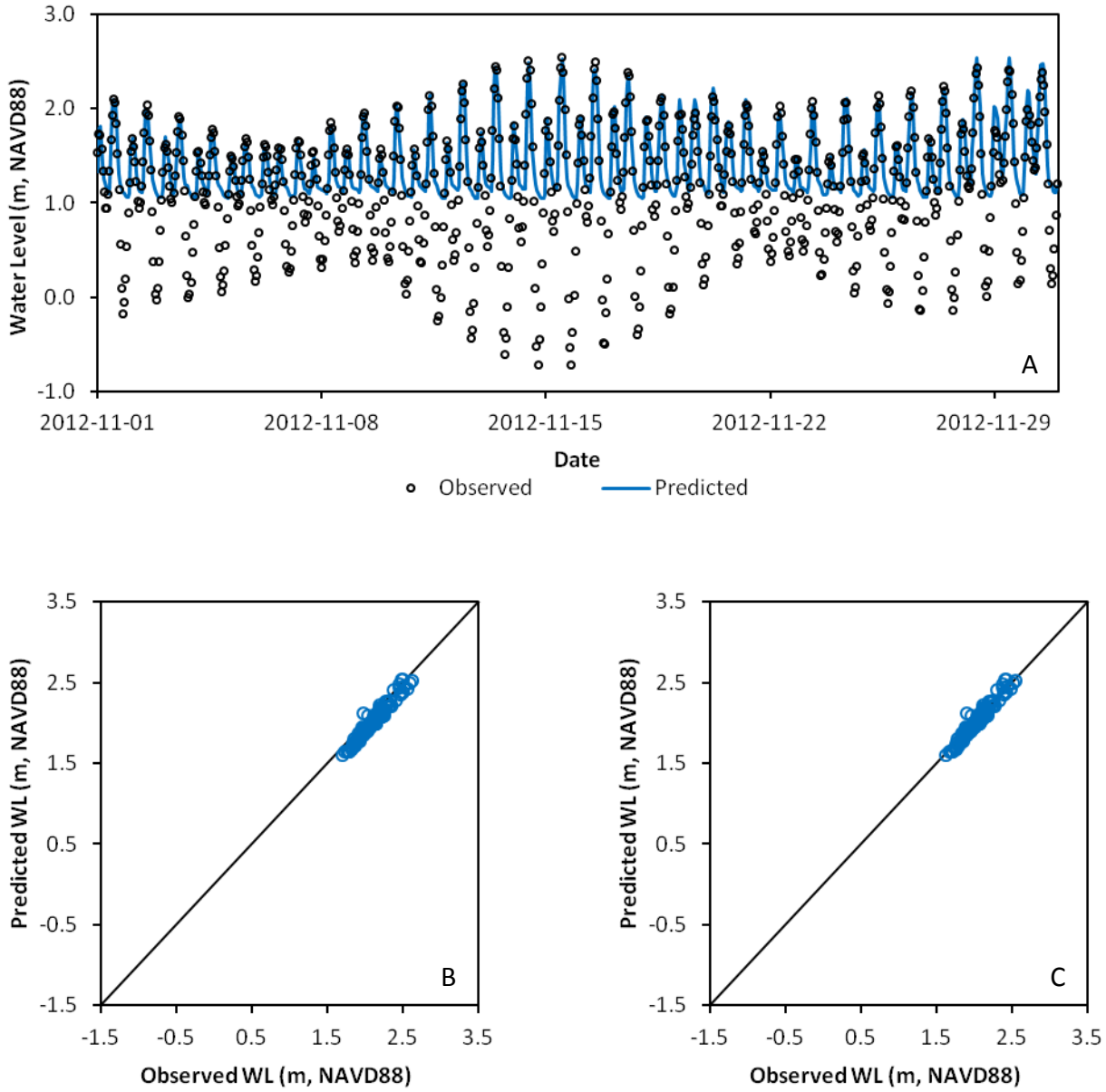

Figure 5-3 Time series and correlation plots of observed and predicted water levels (WL) for Hookton Slough NOAA tide gauge (9418686). Tidal observations were from NHE and CG (2013) and were adjusted for vertical land motion (VLM) estimates (Table 5-1). Plot A is a time series for November 2012, plot B is the correlation between predicted and observed daily maximum water levels prior to adjusting for VLM, and plot C is the correlation between predicted and observed daily maximum water levels after adjusting for VLM. The 2D model grid resolution did not allow full simulation of the tidal range, and an hourly water level correlation was not provided for this gauge.